



Three models of magnetic ordering in typical magnetic materials

G.D. Tang^{a,b,*}, Z.Z. Li^a, L. Ma^a, W.H. Qi^a, L.Q. Wu^a, X.S. Ge^a, G.H. Wu^b, F.X. Hu^b

^a Hebei Advanced Thin Film Laboratory, Department of Physics, Hebei Normal University, Shijiazhuang City, 050024, People's Republic of China

^b State Key Laboratory of Magnetism, Institute of Physics, Chinese Academy of Sciences, Beijing 100190, People's Republic of China



ARTICLE INFO

Article history:

Accepted 28 June 2018
Available online 11 July 2018
Editor: F. Parmigiani

Keywords:

Models of magnetic ordering
Spin arrangements in magnetically ordered materials
Magnetic oxides
Metals and alloys

ABSTRACT

In this work, we review three models of magnetic ordering in typical magnetic materials that have been proposed based on atomic physics. The first model we discuss is the O 2p itinerant electron model for magnetic oxides, which is called the IEO model. Using this model, the magnetic structures of spinel ferrites $M\text{Fe}_2\text{O}_4$, where $M = \text{Ti}, \text{Cr}, \text{Mn}, \text{Fe}, \text{Co}, \text{Ni}$, or Cu , and perovskite manganites $\text{La}_{1-x}\text{Sr}_x\text{MnO}_3$, where $0.0 \leq x \leq 0.4$, can be explained. The second model considered is a new itinerant electron model for magnetic metals, called the IEM model. The IEM model can be employed to explain the relation between the average magnetic moment per atom and resistivity for Fe, Ni, and Co metals. According to this model, free electrons in magnetic metals should be distinguished from itinerant electrons. Then, when the free electrons are excluded, the itinerant electrons transitioning between adjacent metal ions in magnetic metals have similar characteristics to those transitioning between adjacent cations and O anions in magnetic oxides. The third model we address is the Weiss electron pair (WEP) model, which is based on the IEO and IEM models. The WEP model is used to explain the origin of the magnetic ordering energy in magnetic metals and oxides and provides a reason for the different Curie temperatures observed in typical magnetic metals and oxides.

© 2018 The Authors. Published by Elsevier B.V. This is an open access article under the CC BY license (<http://creativecommons.org/licenses/by/4.0/>).

Contents

1. Introduction.....	2
1.1. Historical perspective: Molecular field.....	2
1.2. Difficulties related to conventional magnetic ordering theory.....	3
1.2.1. Disputes over the distributions of Mn and Cr cations in (A)B ₂ O ₄ spinel ferrites.....	3
1.2.2. Difficulties in describing the observed magnetic moments of R _{1-x} T _x MnO ₃ perovskite manganites.....	5
1.2.3. What is the relation between the electrical resistivity and average atomic magnetic moment in Fe, Co, and Ni metals?.....	5
1.2.4. Is there a phenomenological model capable of explaining the origin of magnetic ordering in both metals and oxides?.....	6
2. Oxide ionicity and its dependence on the cation ionization energies.....	6
2.1. Conventional ionicity investigations.....	7
2.2. New definition of ionicity and its measurement using X-ray photoelectron spectra.....	8
2.3. Ionicities of spinel ferrites.....	9

* Corresponding author at: Hebei Advanced Thin Film Laboratory, Department of Physics, Hebei Normal University, Shijiazhuang City, 050024, People's Republic of China.

E-mail address: tanggd@hebtu.edu.cn (G.D. Tang).

2.3.1.	Quantum-mechanical potential barrier model used to estimate cation distributions.....	10
2.3.2.	Ionicity of the cubic spinel ferrite Fe_3O_4	10
2.3.3.	Estimation of the ionicities of MFe_2O_4 spinel ferrites.....	11
3.	O 2p itinerant electron model for magnetic oxides (IEO model).....	12
3.1.	O 2p hole model: A simple introduction	12
3.2.	IEO model.....	13
4.	Applications of the IEO model to spinel ferrites	14
4.1.	Cation distributions and magnetic moment directions in Cr- and Co-substituted spinel ferrites $\text{Ni}_{0.7}\text{Fe}_{2.3}\text{O}_4$	14
4.2.	Discussion of the magnetic structures and cation distributions in $\text{M}_x\text{N}_{1-x}\text{Fe}_2\text{O}_4$ ferrites.....	18
4.3.	Important experimental evidence for the IEO model from Ti-doped spinel ferrites	21
4.4.	Experimental evidence for the IEO model from the infrared spectra of MFe_2O_4 samples	25
4.5.	Canted magnetic structures and cation distributions in the spinel ferrites $\text{MN}_x\text{Fe}_{2-x}\text{O}_4$	26
4.6.	Canted magnetic structures and cation distributions in $\text{M}_x\text{Mn}_{1-x}\text{Fe}_2\text{O}_4$ (M = Zn, Mg, or Al).....	29
5.	Applications of the IEO model to ABO_3 perovskite manganites.....	30
5.1.	Magnetic structures of the perovskite manganites $\text{La}_{1-x}\text{Sr}_x\text{MnO}_3$ ($0 \leq x \leq 0.4$).....	30
5.2.	Influence of thermal treatment on the ionic valences and magnetic structures of the perovskite manganites $\text{La}_{0.95}\text{Sr}_{0.05}\text{MnO}_3$	39
5.3.	Magnetic structures in several series of perovskite manganites with Fe and Cr doping	40
5.4.	Magnetic structures of the perovskite manganites $\text{Pr}_{0.6}\text{Sr}_{0.4}\text{M}_x\text{Mn}_{1-x}\text{O}_3$	41
5.4.1.	Magnetic structure of $\text{Pr}_{0.6}\text{Sr}_{0.4}\text{MnO}_3$	42
5.4.2.	Magnetic structure of $\text{Pr}_{0.6}\text{Sr}_{0.4}\text{Mn}_{1-x}\text{M}_x\text{O}_3$ (M = Cr, Fe, Co, or Ni).....	43
6.	Comparison of the IEO model to the super-exchange (SE) and double-exchange (DE) models of magnetic ordering in oxides.....	45
7.	New itinerant electron model for magnetic metals (IEM model).....	46
8.	Weiss electron pair (WEP) model and magnetic ordering energy	47
8.1.	WEP model.....	47
8.2.	Estimation of the energies of the Weiss molecular fields for several materials.....	48
8.3.	Thermal expansivity near the Curie temperature	49
8.4.	Discussion of the relation between the WEP and Weiss molecular field energies	49
8.5.	Why do typical magnetic metals and oxides have different Curie temperatures?	51
9.	Summary and prospects for future work	52
	Acknowledgments	53
	References	53

1. Introduction

As is well known, there are magnetic domains in ferromagnetic, ferrimagnetic, and antiferromagnetic materials below the Curie or Néel temperature. In a magnetic domain, adjacent ionic magnetic moments are ordered [1–3].

1.1. Historical perspective: Molecular field

To explain the magnetic ordering phenomena [4,5] in ferromagnetic, ferrimagnetic, and antiferromagnetic materials, Pierre Weiss proposed in 1907 that a powerful molecular field existed that acted to align the ionic magnetic moments in a domain and was sufficiently strong to counter powerful internal magnetic repulsive forces between ionic magnetic moments. The magnitude of this molecular field could be estimated from the Curie temperature T_C by using the following relation [6]:

$$k_B T_C = H_m g S \mu_B, \quad (1.1)$$

where Boltzmann's constant k_B is $1.38 \times 10^{-23} \text{ J K}^{-1}$, the Bohr magneton μ_B is $1.165 \times 10^{-29} \text{ J m A}^{-1}$, H_m is the molecular field intensity, g is the Landé g -factor, and $gS\mu_B$ is assumed to be the average atomic moment. For Fe, a ferromagnetic metal with $T_C = 1043 \text{ K}$ and $gS\mu_B = 2.22 \mu_B$, the molecular field intensity H_m thus has an estimated value of

$$H_m = \frac{k_B T_C}{gS\mu_B} = \frac{1043 \times 1.38 \times 10^{-23}}{2.22 \times 1.165 \times 10^{-29}} = 5.565 \times 10^8 \text{ A m}^{-1} = 6.994 \times 10^6 \text{ Oe}. \quad (1.2)$$

While the model proposed by Weiss provided some insight into the nature of magnetic ordering, it failed to explain the origin of such large molecular fields in magnetic metals and alloys. An explanation of how such powerful fields arise was only provided after Heisenberg and Dirac obtained their results some years later. They explained the origin of the molecular field by detailing the theory of the exchange interaction between electrons in neighboring atoms. This exchange interaction was investigated using quantum mechanical theory, based on the local electron model, or quasi-free electron model, for different magnetic systems. Later, to explain antiferromagnetic and ferromagnetic coupling in magnetic oxides, the molecular field concept was extended using the super-exchange (SE) and double-exchange (DE) interaction models, respectively. Regretfully, we do not have sufficient space to provide thorough accounts of these models, although reviews are widely available in the literature [1–3,6].

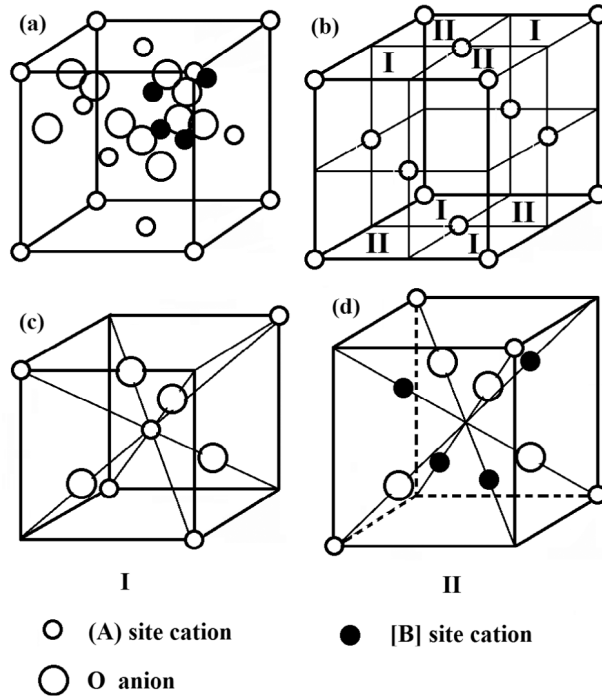


Fig. 1. Illustration of a crystal cell (a) and (b), and its (A) and [B] sites, (c) and (d), in $(A)[B]_2O_4$ spinel ferrites (from Fang and Lu [7]).

1.2. Difficulties related to conventional magnetic ordering theory

Although magnetic ordering theory has been developing for more than 100 years since Weiss first proposed his molecular field assumption, and despite the many successes of traditional models, explaining experimental magnetic ordering data still presents numerous difficulties for theorists. Some notable examples are the conflicting accounts regarding the distributions of Mn and Cr cations in $(A)[B]_2O_4$ spinel ferrites; the failure to describe the magnetic moments observed in $R_{1-x}T_xMnO_3$ perovskite manganites; the failure to explain the relation between the electrical resistivity and average atomic magnetic moment of Fe, Co, and Ni metals; and the absence of a consistent model explaining the magnetic ordering in both metals and oxides. In the rest of this introduction, we shall briefly discuss each of these challenges related to conventional magnetic ordering theory and the experimental data highlighting these difficulties.

1.2.1. Disputes over the distributions of Mn and Cr cations in $(A)[B]_2O_4$ spinel ferrites

The $(A)[B]_2O_4$ spinel ferrites are typical ferrimagnetic materials and have attracted significant attention due to their excellent physical properties and potential applications. In spinel ferrites, the O ions are arranged in close-packed, face-centered-cubic (FCC) lattice structures. As shown in Fig. 1, there are two types of interstitial sites that are occupied by the metal atoms: tetrahedral (a) or (A) sites and octahedral (16d) or [B] sites [1–3,7]. The crystal lattice constant a ; the distances from the O anions to the cations at the (A) and [B] sites, d_{AO} and d_{BO} , respectively; and the distance from the cations at the (A) sites to those at the [B] sites d_{AB} can all be obtained using X-ray diffraction (XRD) data. The ideal values of d_{AO} , d_{BO} , and d_{AB} for the cubic spinel structure are known to be $\sqrt{3}a/8$, $a/4$, and $\sqrt{11}a/8$, respectively. From these values, it can be inferred that the volume of space surrounding a tetrahedral (A) site is smaller than that surrounding a [B] site. In general, the experimentally observed average value of d_{AO} is larger than the ideal value of $\sqrt{3}a/8$, while d_{BO} is often smaller than $a/4$. However, the observed value of d_{AB} is almost always equal to its ideal value.

Traditionally, if MFe_2O_4 ferrites have eight divalent cations occupying the (A) sites and 16 trivalent ferric cations occupying the [B] sites, they are described as having normal spinel structures, which tend to optimize the charge density balance. However, if the eight divalent cations occupy the [B] sites and the 16 trivalent ferric ions are evenly divided between the (A) and [B] sites, the system is classified as having an inverse spinel structure, which tends to lower the Pauli repulsion energy in the (A) sites. In the spinel ferrites MFe_2O_4 , where $M = Fe, Co, Ni, \text{ or } Cu$, all of the cation magnetic moments of the (A) or [B] sites are parallel at low temperatures, but the cation magnetic moments of the (A) sites are antiparallel to those of the [B] sites.

According to the conventional theory, the magnetic structures of spinel ferrites have been explained using the magnetic SE interaction model [2,3]. Based on this traditional view, McQueeney et al. [8] and Moyer et al. [9] proposed that Fe_3O_4 has a completely inverse spinel crystal structure, with the Fe^{3+} cations at the octahedral and tetrahedral sites coupled

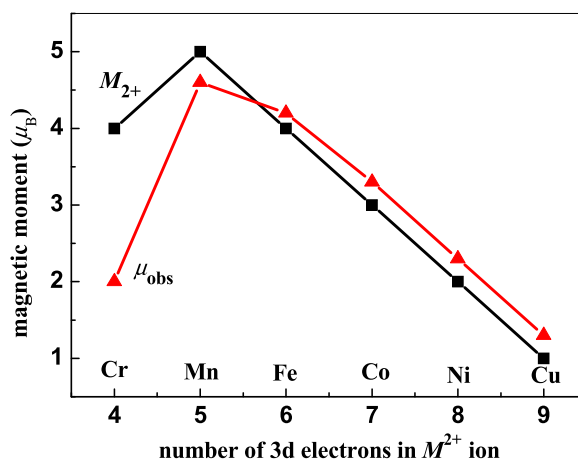


Fig. 2. Observed molecular magnetic moment, μ_{obs} (\blacktriangle), and divalent M -ion magnetic moment, M_{2+} (\blacksquare), of (A)[B] $_2$ O $_4$ spinel ferrites MFe_2O_4 ($M = Cr, Mn, Fe, Co, Ni$ and Cu), as a function of the number of 3d electrons in the divalent M -ion.

Table 1

Ratio between the average numbers of Mn cations occupying (A) and [B] sites per formula of spinel ferrites, as reported by different authors.

Material	Mn content ratio occupying the (A)/[B] sites	Reference
$Ni_{0.7}Mn_{0.3}Nd_{0.1}Fe_{1.9}O_4$	0.3/0.0	[10] Zhao et al. (2008)
$Fe_{3-x}Mn_xO_4$ ($x = 0, 0.25, 0.5, 0.75$ and 1.0)	0.0/ x	[11] Li et al. (2012)
$CoMn_xFe_{2-x}O_4$ ($0.0 \leq x \leq 1.0$)	0.0/ x	[12] Fayek et al. (1992)
$Co_{1-x}Mn_xFe_2O_4$ ($x = 0.2, 0.4$)	0.0/ x	[14] Lee et al. (1998)
$Ni_{1-x}Cu_xFe_{2-y}Mn_yO_4$ ($x = 0.2, 0.5, 0.8$; $y = 0.25, 0.50, 0.75$)	0.00/ y	[13] Roumaih (2001)
$Co_{1-x}Mn_xFe_2O_4$ ($x = 0.6$)	0.40/0.19	[14] Lee et al. (1998)
$Ni_{1-x}Cu_xFe_{2-y}Mn_yO_4$ ($x = 0.5, 0.8$; $y = 1.0$)	0.25/0.75	[13] Roumaih (2001)
$Co_{1-x}Mn_xFe_2O_4$ ($x = 0.8$)	0.22/0.54	[14] Lee et al. (1998)
$Mn_{0.80}Zn_{0.18}Fe_{2.02}O_4$	0.71/0.09	[15] Sakurai et al. (2008)
$Mn_{0.972}Fe_{1.992}O_4$	0.787/0.185	[16] Harrison et al. (1957)

antiferromagnetically via the magnetic SE interaction, while the Fe^{2+} and Fe^{3+} cations at the octahedral sites are coupled ferromagnetically through the magnetic DE interaction. Thus, the $2p$ electrons of the O anions mediate the hopping of E_g electrons between the Fe^{2+} and Fe^{3+} cations.

If the MFe_2O_4 lattice is considered to have an inverse spinel structure, where the Fe^{3+} cations at the (A) and [B] sites are coupled antiferromagnetically, the sum of the magnetic moments of the Fe^{3+} cations must be zero, and the calculated average magnetic moments per formula must be equal to the magnetic moments of the M^{2+} cations occupying the [B] sites, M_{2+} . The experimentally observed average molecular magnetic moments of MFe_2O_4 with $M = Fe, Co, Ni,$ and Cu are $\mu_{obs} = 4.2, 3.3, 2.3,$ and $1.3 \mu_B$, respectively [1–3], which are all slightly greater than those of M_{2+} (4, 3, 2, and $1 \mu_B$). Thus, the inverse spinel structure is a better approximation for these materials. However, for $MnFe_2O_4$, μ_{obs} is $4.6 \mu_B$, which is slightly less than that of the Mn^{2+} cation ($5 \mu_B$). Furthermore, for $CrFe_2O_4$, μ_{obs} is $2.0 \mu_B$, which is only half that of Cr^{2+} ($4 \mu_B$). The dependences of μ_{obs} and M_{2+} on the number of 3d electrons in M^{2+} cations, n_d , are shown in Fig. 2. As the observed moments of the materials with $M = Mn$ and Cr do not follow the same trend as those of the materials with $M = Fe, Co, Ni,$ and Cu , the analysis of the cation distributions in Mn- or Cr-doped spinel ferrites is complicated and has resulted in many conflicting claims.

Table 1 presents a summary of some of the studies that have been performed using Mn-doped spinel ferrites, for a number of different fabrication processes. Zhao et al. [10] prepared nanocrystalline $Ni_{0.7}Mn_{0.3}Nd_{0.1}Fe_{1.9}O_4$ ferrite using an emulsion method and concluded from the Mössbauer spectra that the Mn^{2+} cations occupied the tetrahedral (A) sites, estimating the cation distributions of the sample to be $(Mn_{0.3}^{2+}Fe_{0.41}^{3+}Ni_{0.29}^{2+})[Ni_{0.41}^{2+}Nd_{0.1}^{3+}Fe_{1.49}^{3+}]O_4$. Li et al. [11] prepared monodispersed $Fe_{3-x}Mn_xO_4$ (for $x = 0, 0.25, 0.5, 0.75,$ and 1.0) and concluded based on their Mössbauer spectra analysis that the Mn ions occupied the [B] sites. Using a ceramic sintering technique, Fayek et al. [12] fabricated six powder samples of $CoMn_xFe_{2-x}O_4$ ($0.0 \leq x \leq 1.0$) and deduced from Mössbauer spectra and neutron diffraction measurements that all of the Mn ions (in this case Mn^{3+} ions) occupied the [B] sites. Roumaih [13] prepared ferrite samples with compositions $Ni_{1-x}Cu_xFe_{2-y}Mn_yO_4$ (with $x = 0.2, 0.5,$ and 0.8 and y varying from 0.0 to 1.0) via solid-state reactions. Based on magnetic measurements and the condition of electroneutrality, they concluded that all of the Mn cations occupied the [B] sites when $y \leq 0.75$ and that 12% (for $x = 0.2$) and 25% (for $x = 0.5$ and 0.8) of the Mn cations occupied the (A) sites when $y = 1.0$. Lee et al. [14] synthesized $Co_{1-x}Mn_xFe_2O_4$ ($0.2 \leq x \leq 0.8$) spinel ferrites via the usual ceramic method. They determined that the Mn^{2+} ions replaced

Table 2

Ratio between the average numbers of Cr cations occupying (A) and [B] sites per formula of spinel ferrites, as reported by different authors.

Material	Cr content ratio occupying the (A)/[B] sites	Reference
$\text{CoAl}_x\text{Cr}_x\text{Fe}_{2-2x}\text{O}_4 (0.0 \leq x \leq 0.5)$	0.0/x	[17] Mane et al. (2000)
$\text{Ni}_{0.5}\text{Mg}_{0.5}\text{Fe}_{2-x}\text{Cr}_x\text{O}_4 (x = 0.2, 0.4, 0.6)$	0.0/x	[19] Hashim et al. (2012)
$\text{Ni}_{0.5}\text{Mg}_{0.5}\text{Fe}_{2-x}\text{Cr}_x\text{O}_4 (x = 0.8)$	0.05/0.75	[19] Hashim et al. (2012)
$\text{Ni}_{0.5}\text{Mg}_{0.5}\text{Fe}_{2-x}\text{Cr}_x\text{O}_4 (x = 1.0)$	0.05/0.95	[19] Hashim et al. (2012)
$\text{Co}_{0.5}\text{Ni}_{0.5}\text{Cr}_x\text{Fe}_{2-x}\text{O}_4 (x = 0.25, 0.5, 0.75, 1.0)$	1/4	[20] Kadam et al. (2013)
$\text{NiCr}_x\text{Fe}_{2-x}\text{O}_4 (x = 0.2)$	0.1/0.1	[21] Ghatage et al. (1996)
$\text{NiCr}_x\text{Fe}_{2-x}\text{O}_4 (x = 0.4)$	0.15/0.25	[21] Ghatage et al. (1996)
$\text{NiCr}_x\text{Fe}_{2-x}\text{O}_4 (x = 0.8)$	0.25/0.55	[21] Ghatage et al. (1996)
$\text{NiCr}_x\text{Fe}_{2-x}\text{O}_4 (x = 1.0)$	0.3/0.7	[21] Ghatage et al. (1996)

the Co^{2+} ions at the [B] sites when x was low, while some of the Mn^{2+} ions replaced the Fe^{3+} ions at the (A) sites when $x \geq 0.6$. Sakurai et al. [15] grew a single crystal $\text{Mn}_{0.80}\text{Zn}_{0.18}\text{Fe}_{2.02}\text{O}_4$ sample and suggested based on their analysis of X-ray absorption near-edge structure spectra and X-ray magnetic circular dichroism spectra that only Mn^{2+} , Zn^{2+} , and Fe^{3+} ions existed in this ferrite. Moreover, they suggested that the Mn^{2+} ions were distributed at both the (A) and [B] sites, and the final chemical formula was given as $(\text{Mn}_{0.71}^{2+}\text{Zn}_{0.10}^{2+}\text{Fe}_{0.19}^{3+})[\text{Mn}_{0.09}^{2+}\text{Zn}_{0.08}^{2+}\text{Fe}_{1.83}^{3+}]\text{O}_4$. Harrison et al. [16] grew single-crystal manganese ferrite via the flame fusion method, from which they determined that 78.7% of the Mn cations occupied the (A) sites. The ratios of the Mn cations occupying the (A) and [B] sites in these reports are summarized in Table 1, demonstrating the wide variety of the results.

A similar variety of results was found in studies on Cr-doped spinel ferrites. Mane et al. [17] fabricated $\text{CoAl}_x\text{Cr}_x\text{Fe}_{2-2x}\text{O}_4$ ($0.0 \leq x \leq 0.5$) ferrite samples via the usual ceramic method. They thought that all of the Cr ions, in the form of Cr^{3+} , occupied the octahedral [B] sites, while the Co ions were distributed across both the (A) and [B] sites. Magalhães et al. [18] synthesized a series of ferrite samples with compositions $\text{Fe}_{3-x}\text{Cr}_x\text{O}_4$ ($x = 0.00, 0.07, 0.26, 0.42, \text{ and } 0.51$) via the conventional co-precipitation method and determined that the Cr^{3+} ions replaced the Fe^{3+} ions at the [B] sites with low x , but with increasing x , the Cr ions replaced both the Fe^{2+} ions at the [B] sites and the Fe^{3+} ions at the (A) sites. Hashim et al. [19] prepared ferrite samples with compositions $\text{Ni}_{0.5}\text{Mg}_{0.5}\text{Fe}_{2-x}\text{Cr}_x\text{O}_4$ ($0.0 \leq x \leq 1.0$) via the citrate-gel auto-combustion method and concluded based on Mössbauer spectroscopy and powder XRD measurements that all of the Cr cations entered the [B] sites when $x \leq 0.6$, with Cr cations entering the (A) sites only when $x \geq 0.8$. Kadam et al. [20] prepared $\text{Co}_{0.5}\text{Ni}_{0.5}\text{Cr}_x\text{Fe}_{2-x}\text{O}_4$ samples using the sol-gel auto-combustion method and obtained the cation distributions by analyzing XRD patterns. They concluded that the ratio between the numbers of Cr cations occupying the (A) and [B] sites was 1/4. Ghatage et al. [21] prepared $\text{NiCr}_x\text{Fe}_{2-x}\text{O}_4$ ($0.2 \leq x \leq 1.0$, with x increasing in increments of 0.2) via the usual ceramic method. Using neutron diffraction, they concluded that the number of Cr ions per formula at the (A) sites increased from 0.10 to 0.30 as x increased from 0.2 to 1.0. The ratios between the numbers of Cr cations occupying the (A) and [B] sites in these reports are summarized in Table 2.

The variety of the results presented in Tables 1 and 2 clearly demonstrate the marked differences regarding the distributions of Mn or Cr cations among these reports, which raises concerns regarding the underlying models.

1.2.2. Difficulties in describing the observed magnetic moments of $R_{1-x}T_x\text{MnO}_3$ perovskite manganites

The manganites $R_{1-x}T_x\text{MnO}_3$ have ABO_3 perovskite structures, where R and T are rare earth and alkaline earth ions, respectively. These materials have been extensively studied due to their rich physics, such as their colossal magnetoresistance, and for their potential applications in magnetic devices [22–25]. Fig. 3 shows an ideal cubic cell with an ABO_3 perovskite crystal structure [7,22]. In an $R_{1-x}T_x\text{MnO}_3$ crystal cell, both the R and T cations occupy the A sites and form the A sublattice, while the Mn cations occupy the B sites and form the B sublattice. The ion distributions of rhombohedral and orthogonal perovskite manganites are very close to those of materials with cubic structures [26]. In earlier work, all of the O ions were assumed to be O^{2-} ions, and the R and Mn ions in RMnO_3 were assumed to be trivalent cations. Furthermore, the concentration of the Mn^{4+} cations in $R_{1-x}T_x\text{MnO}_3$ samples was assumed to be the same as that of the T^{2+} cations. It was also assumed that the spin structure and electronic transport properties of $R_{1-x}T_x\text{MnO}_3$ were correlated via the DE mechanism [27–31], whereby the hopping of e_g electrons between the Mn^{3+} and Mn^{4+} cations is mediated by O^{2-} anions, whereas the antiferromagnetic spin structure of RMnO_3 was thought to be correlated via the magnetic SE interaction between Mn^{3+} cations (also being mediated by O^{2-} anions). Millis et al. [32] proposed that the Jahn–Teller effect should be considered, in addition to the DE interaction, to explain the magnetic and electrical transport properties of perovskite manganites. However, no method capable of being used to estimate the magnetic moments of $R_{1-x}T_x\text{MnO}_3$ materials using the DE and SE models has been reported. For example, both Urushibara et al. [33] and Jonker and Van Santen [28] reported that the experimental magnetic moment per formula of $\text{La}_{1-x}\text{Sr}_x\text{MnO}_3$ increased from 0.0 ($x = 0.00$) to $4.2 \mu_B$ ($x = 0.15$). However, the dependence of the magnetic moment on x could not be determined in either case.

1.2.3. What is the relation between the electrical resistivity and average atomic magnetic moment in Fe, Co, and Ni metals?

The observed average atomic magnetic moments for Fe, Ni, and Co can be found easily in the literature [6,34,35], where they are listed as 2.22, 0.62, and $1.72 \mu_B$, respectively. Similarly, the observed electrical resistivities are given in the literature [34] as 8.6, 6.14, and $5.57 \mu\Omega \text{ cm}$, respectively, for Fe, Ni, and Co. One would expect these magnetic moments and resistivities to be related in valence electron states; however, to date, no such relation has been reported.

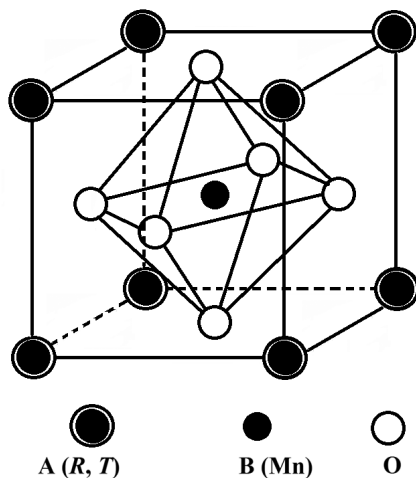


Fig. 3. Illustration of the cubic ABO_3 perovskite manganite crystal cell (from Fang and Lu [7], Salamon et al. [22]).

Table 3

Crystal structure, observed average molecular magnetic moments, μ_{obs} , and Curie temperature, T_C , of several metals and oxides.

Material	Crystal structure	μ_{obs} (μ_B)	T_C (K)	Reference
Fe	BCC	2.22	1043	[35] Stöhr et al., 2006
Co	HCP	1.72	1404	[35] Stöhr et al., 2006
Ni	FCC	0.62	631	[35] Stöhr et al., 2006
$MnFe_2O_4$	Spinel	4.6	570	[3] Chikazumi, 1997
$FeFe_2O_4$	Spinel	4.2	860	[2] Chen, 1977
$CoFe_2O_4$	Spinel	3.3	793	[2] Chen, 1977
$NiFe_2O_4$	Spinel	2.3	863	[2] Chen, 1977
$CuFe_2O_4$	Spinel	1.3	766	[2] Chen, 1977
$La_{0.8}Ca_{0.2}MnO_3$	perovskite	3.76	198	[36] Hibble et al., 1999
$La_{0.75}Ca_{0.25}MnO_3$	perovskite	3.13	240	[37] Radaelli et al., 1995
$La_{0.85}Sr_{0.15}MnO_3$	perovskite	4.2	238	[33] Urushibara et al., 1995
$La_{0.7}Sr_{0.3}MnO_3$	perovskite	3.5	369	[33] Urushibara et al., 1995

1.2.4. Is there a phenomenological model capable of explaining the origin of magnetic ordering in both metals and oxides?

Table 3 shows the crystal structure, μ_{obs} , and T_C for several typical magnetic metals and oxides [2,3,33,35–37]. It is easy to see that the T_C values of the spinel ferrites are close to that of Ni, while those of the perovskite manganites are much lower than those of the spinel ferrites. These results indicate that there is an intrinsic relation between the magnetic properties of magnetic metals and oxides; however, this intrinsic relation has never been satisfactorily explained.

To explain these phenomena, Tang et al. proposed a series of magnetic ordering models based on atomic physics: (i) the O 2p itinerant electron model for magnetic oxides, or IEO model; (ii) the new itinerant electron model for magnetic metals, or IEM model; and (iii) the Weiss electron pair (WEP) model for the magnetic ordering energy.

By applying these models, Tang et al. were able to explain many controversial experimental results, including the four puzzles outlined above.

The remaining sections of this work are organized as follows. Since the IEO model is based on the assumption that there are both O^{1-} and O^{2-} ions present in oxides, Section 2 introduces the topic of oxide ionicity and discusses its dependence on the ionization energies of the cations. In Sections 3–5, we describe the IEO model in greater detail and discuss its applications to both (A)[B]₂O₄ spinel ferrites and ABO_3 perovskite manganites. Section 6 addresses the relations and differences between the IEO model and the conventional SE and DE models. In Section 7, we introduce the IEM model and discuss its application to explaining the relation between the resistivity and average atomic magnetic moment of Fe, Co, and Ni. The WEP model is introduced in Section 8, and we describe its application to explaining the thermal expansivity near T_C for several perovskite manganite materials and how it elucidates why typical magnetic metals and oxides have different T_C . The final section, Section 9, is devoted to a brief recapitulation of the primary findings and a discussion of the potential topics of future work.

2. Oxide ionicity and its dependence on the cation ionization energies

One elementary reason for the difficulties involved in adequately explaining the magnetic oxide puzzles outlined above using the conventional models is that the ionicity of the oxides is neglected in these models. In both the conventional SE and DE models, the valence of all of the O anions is assumed to be -2.0 . It will be seen in what follows that the absolute value of

Table 4

First, second, third, and fourth ionization energies (eV) of free 3d transition metal atoms (from Liao [38]).

No.	Sc	Ti	V	Cr	Mn	Fe	Co	Ni	Cu	Zn
1	6.56	6.82	6.75	6.77	7.43	7.90	7.88	7.64	7.73	9.39
2	12.80	13.58	14.66	16.49	15.64	16.19	17.08	18.17	20.29	17.96
3	24.76	27.49	29.31	30.96	33.67	30.65	33.50	35.19	36.84	39.72
4	73.49	43.27	46.71	49.16	51.2	54.8	51.3	54.9	57.38	59.4

the average valence of the O ions in an oxide is less than 2.0. This feature implies that oxides contain O^{1-} ions, in addition to the expected O^{2-} ions. While the O^{2-} ions have full outer electron shells with the electronic configuration $2s^2 2p^6$, the outer orbit of an O^{1-} ion (with the electronic configuration $2s^2 2p^5$) contains a $2p$ hole that affects the magnetic ordering and electrical transport properties of the oxide.

2.1. Conventional ionicity investigations

It is well known that O has a second electron affinity energy of 8.08 eV, while the second and third ionization energies of the free 3d transition metal atoms (from Sc to Zn) range from 12.80 eV to 39.72 eV [38], as shown in Table 4. It is reasonable to assume that the ionization energies of the free atoms affect how ions gain and lose electrons in oxides. To describe this property, many attempts have been made to formulate the concept of ionicity [39].

One common approach is based on molecular orbital theory, which is concerned with the combination of atomic orbitals to form new molecular orbitals. In molecular orbital theory, new orbitals arise from linear combinations of the initial atomic orbitals and can form bonding and antibonding orbitals, where the bonding orbitals have lower energies than the antibonding orbitals. Consequently, there is an energy gap E_g between the bonding and antibonding states. Based on dispersion theory and molecular orbital theory, Phillips [39] defined the ionicity as

$$f_i = C^2 / (E_h^2 + C^2), \quad (2.1)$$

where $E_g^2 = E_h^2 + C^2$, with E_h and C arising from the real and imaginary components, respectively, of the pseudopotential of the model. In the case of a purely covalent Group IV crystal such as diamond, Si, or Ge, $E_h = E_g$ (i.e., $C = 0$), while in the case of an ideal ionic crystal, $C = E_g$ (i.e., $E_h = 0$). However, in actual experiments, there is no truly ideal ionic crystal. Phillips [39] reviewed both the spectroscopic methods used to determine E_h and C and studies of the ionicities of simple compounds and summarized the resulting ionicity data, as shown in Table 5. Here, f_{IP} is the Phillips ionicity, f_i and f_{i1} are the Pauling ionicities [39], and the remaining parameters will be introduced in Section 2.3.3.

Numerous further ionicity studies followed the work conducted by Phillips, which we briefly summarize here. Thomas and Pollini [40] reported the ionicities of the dihalides MX_2 ($M = Mn, Fe, Co, \text{ or } Ni$), which were obtained using the dielectric theory of the chemical bond, with their results ranging from $f_i \approx 0.72$ (for NiI_2) to $f_i \approx 0.80$ (for $MnCl_2$). Chelikowsky and Burdett [41] examined the relationship between the spectroscopic crystal ionicity and spatial structures of several II–VI and III–V compounds based on dielectric theory. García and Cohen [42] provided a first-principles mapping to the ionicity scale proposed by Pauling for $A^N B^{8-N}$ solids using a measure of the asymmetry of the valence charge distribution in $A^N B^{8-N}$ compounds. Peng et al. [43] determined that the ionicity of NiO was 0.3 using reflection high-energy electron diffraction and reflection electron microscopy. Chambers and Droubay [44] found that there were higher degrees of covalent bonding in $\alpha\text{-Cr}_2\text{O}_3$ and $\alpha\text{-Fe}_2\text{O}_3$ than in MgO by measuring the photoemission spectra of ultrathin epitaxial films of $\alpha\text{-Cr}_2\text{O}_3$ and $\alpha\text{-Fe}_2\text{O}_3$ on Pt(111). Balamurugan et al. [45] examined the relationship between the ionicity of Cu_2O samples and their particle size using X-ray photoelectron spectroscopy (XPS). Guittet et al. [46] concluded that the degree of ionic/covalent character in oxides significantly influenced the electronic structure of a material and its properties. Ito et al. [47] found, using first-principles calculations, that the Li ionicity in LiMn_2O_4 remained high and that the Mn–O covalent bonding was stronger following substitution of M ($M = Zn \text{ or } Ni$) for Mn than it was in the parent LiMn_2O_4 . Abu-Farsakh and Qteish [48] calculated the ionicities of 32 $A^N B^{8-N}$ compounds, ranging from elemental Group IV solids to I–VII compounds, using maximally localized Wannier functions. Yu et al. [49] investigated plasma-assisted molecular beam epitaxial anatase $\text{TiO}_{2-x}\text{N}_x$ ($x < 0.3$) films and, in combination with experimental results obtained from XRD and atomic force microscopy, found that the average ionicity of the Ti–O (or N) bonds decreased slightly following N substitution for the lattice O ions. Lizárraga et al. [50] examined the structural characterization of amorphous alumina and its polymorphs using X-ray photoemission spectra and nuclear magnetic resonance (NMR) from first-principle calculations and determined that the local environments of the strongly ionic Al–O bonds could be well resolved by calculating the NMR chemical shifts. Christensen et al. [51] reported their theoretical investigations of the bonding properties of 34 elemental and compound semiconductors and obtained the associated valence charge densities from self-consistent band-structure calculations (within the local-density approximation), where they too were able to establish a relation to the Phillips ionicity scale. Arif et al. [52] reported the results of their study of the ionicity factors of semiconductors with hexagonal structures based on the energy gap, and using density functional theory (DFT) with a full-potential linear augmented plane wave theory.

From this plethora of results, it should be clear how complex and critical ionicity is in models of atomic bonding, as well as in describing how ions gain and lose electrons.

Table 5

Ionicities of II–VI compounds. Here, f_{IP} and f_i (f_{i1}) are the Phillips and Pauling ionicities (from Phillips [39]). f_{IT} is the ionicity as calculated by Ji et al. [63], where R is the probability ratio, between the question and Sr compounds, of the second electron in the cation jumping to the anions through the potential barrier with height V_{2i} and width r , where V_{2i} is the second ionization energy of the question cation and r is the effective radius of the anions with coordination number N .

Material	f_{IP}	f_i Pauling (1932)	f_{i1} Pauling (1939)	f_{IT}	N	V_{2i} (eV)	r (nm)	R
BeO	0.602	0.63	0.81	0.568	4	18.21	0.138	0.159
ZnO	0.616	0.59	0.80	0.572	4	17.96	0.138	0.168
CdO	0.785	0.55	0.85	0.589	6	16.91	0.14	0.210
MgO	0.841	0.73	0.88	0.641	6	15.04	0.14	0.330
CaO	0.913	0.79	0.97	0.831	6	11.87	0.14	0.778
SrO	0.926	0.79	0.93	0.926	6	11.03	0.14	1.000
BeS	0.312	0.22	0.61	0.543	4	18.21	0.181	0.105
ZnS	0.623	0.18	0.59	0.546	4	17.96	0.181	0.112
CdS	0.685	0.18	0.59	0.562	4	16.91	0.181	0.151
MgS	0.786	0.34	0.67,	0.606	6	15.04	0.184	0.257
CaS	0.902	0.43	0.81	0.804	6	11.87	0.184	0.735
SrS	0.914	0.43	0.91	0.914	6	11.03	0.184	1.000
BeSe	0.299	0.18	0.59	0.538	4	18.21	0.195	0.092
ZnSe	0.676	0.15	0.57	0.541	4	17.96	0.195	0.099
CdSe	0.699	0.15	0.58	0.556	4	16.91	0.195	0.134
MgSe	0.790	0.29	0.65,	0.599	6	15.04	0.198	0.237
CaSe	0.900	0.39	0.90	0.801	6	11.87	0.198	0.723
SrSe	0.917	0.39	0.80	0.917	6	11.03	0.198	1.000
BeTe	0.169	0.09	0.55	0.530	4	18.21	0.218	0.073
ZnTe	0.546	0.06	0.53	0.532	4	17.96	0.218	0.079
CdTe	0.675	0.04	0.52	0.545	4	16.91	0.218	0.112
MgTe	0.554	0.18	0.59	0.584	6	15.04	0.221	0.208
CaTe	0.894	0.26	0.88	0.783	6	11.87	0.221	0.702
SrTe	0.903	0.26	0.75	0.903	6	11.03	0.221	1.000

2.2. New definition of ionicity and its measurement using X-ray photoelectron spectra

A very interesting result is revealed if we consider the Phillips ionicity, f_{IP} , as a function of the second ionization energy V_{2i} . Taking the data from Table 5, curves of f_{IP} versus V_{2i} of the cation are shown in Fig. 4(a) for several compounds. Notably, f_{IP} decreases with increasing V_{2i} . Similarly, Guo et al. [53] and Raddy et al. [54] reported the ionicities, f_i , of several dioxides, where the dependence of f_i on the fourth ionization energy V_{4i} of the cations is shown in Fig. 4(b). It can be seen that f_i is less than 0.75 when $V_{4i} > 44$ eV, which suggests that there is no quadrivalent cation when $V_{4i} > 44$ eV. These variations of the ionicity with the ionization energy of the cations can be understood simply as follows: since it is difficult for an electron with a high ionization energy to be lost by its cation, the absolute value of the valence of each compound is less than its ideal value. For example, the absolute value of the average valence for O anions $|V_{alO}|$ in an oxide is less than 2.0, which has been proven both theoretically and experimentally.

Using first-principles calculations, Cohen and Krakauer [55,56] calculated the effective charges of the O, Ti, and Ba atoms in BaTiO₃. Their results indicated that the average valence of Ba is +2, which is the same as the traditionally accepted value, but the average valences of Ti and O are +2.89 and −1.63, respectively, which are different from the conventional results of +4 and −2, respectively. Dupin et al. [57] proposed that a portion of the O ions in oxides are O^{1−} ions based on the XPS analysis, and provided the average net charge q_o of the O ions in the considered oxides; specifically, q_o of the O ions was found to be −1.15, −1.18, −1.05, −1.78, and −1.85 for TiO₂, ZrO₂, CoO, CaO, and SrO, respectively. These results could be understood by considering the presence of O^{1−} anions, in addition to the expected O^{2−} anions. Thus, q_o of the O ions can be understood equivalently as the average valence V_{alO} .

Based on these investigations, Wu et al. [58] proposed a new definition of the ionicity as the ratio of the average valence to the ideal valence of the anions in a compound. For example, in an oxide, the f_i would be $|V_{alO}|/2$. Using the data reported by Dupin et al. [57] and given the above, the ionicities of CaO and SrO (with $f_i = |V_{alO}|/2 = |q_o|/2$) were determined to be 0.890 and 0.925, respectively, which agree well with those found by Phillips (0.913 and 0.926, see Table 5) [39].

Following the method employed by Dupin, Wu et al. [58] investigated the ionicities for BaTiO₃ and several other monoxide powder samples using O 1s photoelectron spectra. In particular, they found that V_{alO} for BaTiO₃ was −1.55, which is close to the value of −1.63 calculated from first principles by Cohen [56]. In addition, they obtained a very interesting result in that $f_i (=|V_{alO}|/2)$ decreased approximately linearly with increasing V_{2i} of the cation M^{2+} , which is very close to the results reported by Phillips [39], as shown in Fig. 5 [58]. In related work, Wu et al. [59] also found the average valences of Ti and O ions in a polycrystalline bulk sample of SrTiO₃ to be +2.98 and −1.62 using XPS with Ar ion etching, which again are close to the values for BaTiO₃ calculated by Cohen [56] (+2.89 and −1.63).

These results indicate that this new definition of the ionicity and the method used to measure ionicity via XPS analysis are reasonable. Moreover, this new definition and measurement method enable the investigation of ionicity in a simple and straightforward manner.

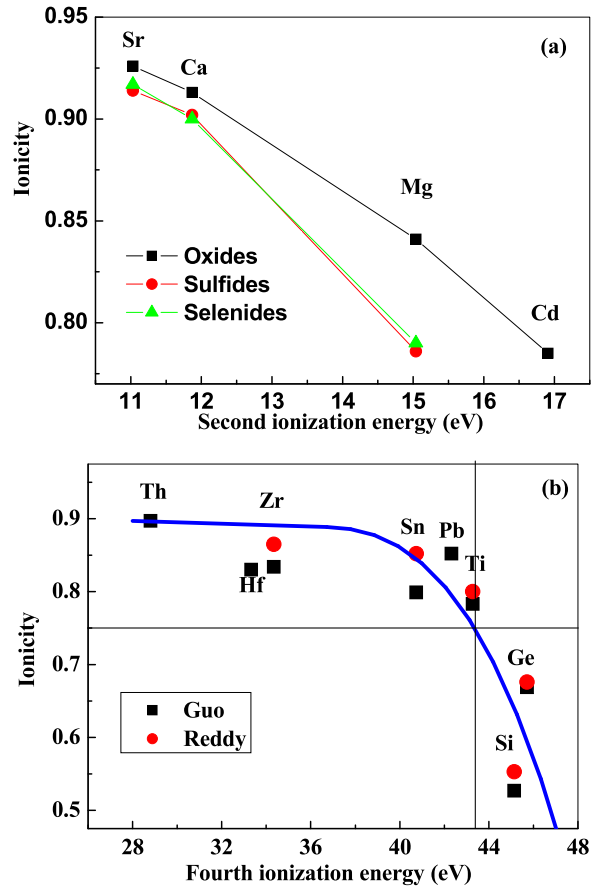


Fig. 4. (a) Phillips' ionicity [39], f_{IP} , of monoxide, monosulfide, and monoselenide compounds as a function of the second cation ionization energy, V_{2i} ; (b) The ionicity of the dioxides reported by Guo et al. [53] (■) and Raddy et al. [54] (●) as a function of the fourth cation ionization energy, V_{4i} .

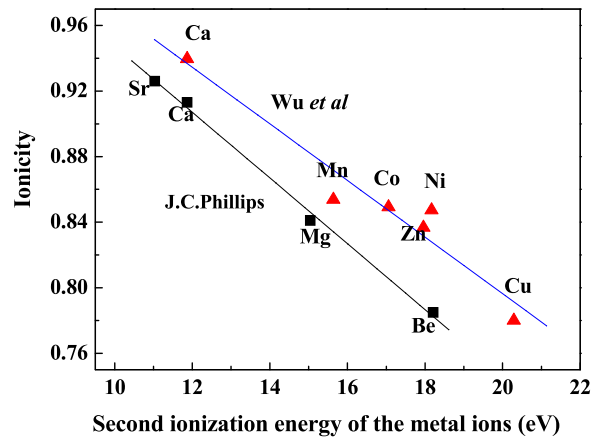


Fig. 5. The ionicities, f_i , of monoxide measured using XPS by Wu et al. [58], as a function of the second ionization energy V_{2i} of the cations. The values reported by Phillips [39] are shown for comparison.

2.3. Ionicities of spinel ferrites

In this section, we consider how the concept of ionicity may be incorporated into the models used to estimate cation distributions and consider the cases of spinel ferrites in detail.

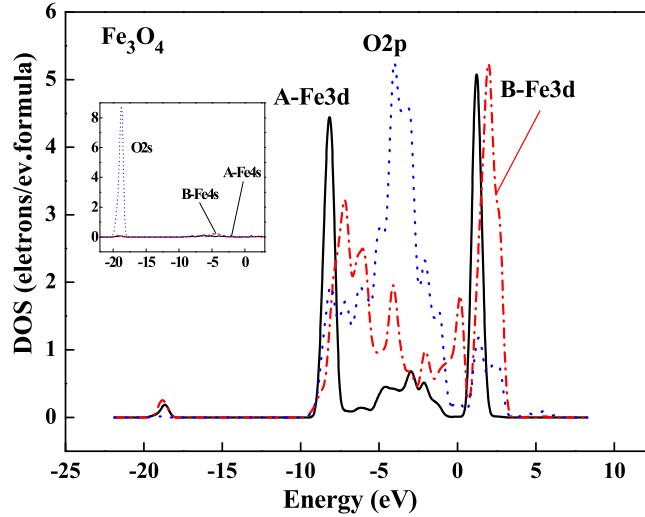


Fig. 6. DOSs of Fe 3d and O 2p electrons in Fe_3O_4 with (A)[B] $_2\text{O}_4$ spinel structure (from Ji et al. [63]).

2.3.1. Quantum-mechanical potential barrier model used to estimate cation distributions

To explain the different cation valences observed in the perovskite manganites $\text{La}_{1-x}\text{Ca}_x\text{MnO}_3$ and spinel ferrites, Tang et al. [60,61] proposed a simple quantum-mechanical potential barrier model for estimating the cation distributions in various compounds. They supposed that a potential barrier exists between each cation–anion pair, whose height is proportional to the ionization energy of the cation, and whose width is related to the distance between the neighboring cations and anions. The ratio between the contents of the different valence cations is therefore related to the probabilities of their last ionized electrons passing through the potential barrier. Using the transmission coefficient of electrons through a square potential barrier [62], Tang et al. [60] derived the following approximate expression for the content ratio R of the different cations:

$$R = \frac{P_C}{P_D} = \frac{V_D}{V_C} \exp \left[10.24 \left(r_D V_D^{1/2} - c_v r_C V_C^{1/2} \right) \right], \quad (2.2)$$

where the lengths and energies are measured in nanometers and electronvolts, respectively. Here, P_C (P_D) represents the probability of the last ionized electron of the C (D) cations jumping to the anions through a potential barrier with height V_C (V_D) and width r_C (r_D). V_C and V_D are the ionization energies of the last ionized electrons of the C and D cations, respectively, and r_C and r_D are the distances from the C and D cations to the anions, respectively. c_v is a correction parameter for the barrier shape that quantifies the extents to which the shapes of the two potential barriers deviate from squares, and $c_v = 1$ when $V_C = V_D$ and $r_C = r_D$.

It should be noted that the ratio of the ionization energies of the free atoms (rather than the ionization energy itself) was used in Eq. (2.2), which can be employed to describe the fact that the cation ionization energies of the free atoms affect how ions gain and lose electrons in oxides. Since the ionization energies of all free atoms are known [38], it is convenient and effective to investigate the ionicity and cation distributions in compounds using Eq. (2.2), as shall be described in the following sections.

2.3.2. Ionicity of the cubic spinel ferrite Fe_3O_4

To investigate the ionicities of spinel ferrites, Ji et al. [63] calculated the density of states (DOS) for the valence electrons in the cubic spinel ferrite Fe_3O_4 using plane-wave pseudopotential DFT. The DOSs of the Fe 3d and O 2p valence electrons are shown in Fig. 6. The inset depicts the DOSs of the Fe 4s and O 2s electrons. Below the Fermi energy level (the energy zero point), the ratio of Fe 4s to Fe 3d electrons was calculated to be $\sim 5\%$, so the Fe 4s electrons could be neglected. Similarly, about 96% of the O 2s electrons were found to be distributed below -17 eV, preventing them from participating in orbital hybridization with the metal cations. Consequently, near the Fermi energy, only the DOSs of the Fe 3d and O 2p electrons need to be considered. Therefore, hybridization between the Fe cations and O anions occurs between the Fe 3d and O 2p orbitals.

The average numbers of 3d electrons calculated to lie below the Fermi energy levels shown in Fig. 6 in Fe_A ions at the (A) sites and Fe_B ions at the [B] sites in Fe_3O_4 are 5.975 and 6.089, respectively. Similarly, the average number of 2p electrons below the Fermi energy at the O ion sites is 4.894. Clearly, the average number of O 2p electrons is less than the value of 6 usually assumed for the O^{2-} anion in the traditional view. Meanwhile, the average number, n_d , in Fe is 6.051 [= (5.975 + 6.089 \times 2)/3], resulting from one Fe_A and two Fe_B ions], which is greater than the value of 5.33 [= (6 + 5 \times 2)/3], for

one Fe^{2+} and two Fe^{3+} ions] assumed in the traditional view, where the valence of the O anion is taken to be -2.0 . Thus, the valence absolute values of both the cations and anions as determined from the DOS are distinctly less than the values expected based on the traditional view, because the second electronic affinity energy of O (8.08 eV) is far lower than the third ionization energy of Fe (30.65 eV), with the result being that Fe^{3+} ions are not easily formed.

According to the traditional view of Fe_3O_4 with an (A)[B] $_2\text{O}_4$ structure, all of the cation magnetic moments at the (A) and [B] sites are parallel at low temperatures, with the (A) and [B] sites considered separately, while the magnetic moments of the ions at the (A) sites are antiparallel to those of the ions at the [B] sites. Using the calculated n_d values mentioned above for Fe, one can calculate that the magnetic moment per formula of Fe_3O_4 is $3.8 \mu_B$, which is smaller than those obtained experimentally ($3.93 \mu_B$ upon Verwey transition (116 K) reported by Tang et al. [64], and $4.2 \mu_B$ in Refs. [2,3]). Therefore, the calculated numbers of Fe 3d valence electrons mentioned above require correction to match the experimentally measured magnetic moments more closely.

For more accurate analysis, Ji et al. [63] defined the average magnetic moment of one Fe cation at an (A) site to be m_A (in units of μ_B), which is antiparallel to that at a [B] site, m_B (also in units of μ_B). To reproduce the correct experimental moment per formula of $4.2 \mu_B$ [2,3], the required condition is

$$2m_B - m_A = 4.2. \quad (2.3)$$

Letting the average ratio between the numbers of 3d electrons in the Fe cations at (A) and [B] sites n_A/n_B be obtained from the calculated DOSs yields

$$n_A/n_B = 5.975/6.089. \quad (2.4)$$

Then, since only 10 electrons with opposite spin directions can occupy the five 3d energy levels of transition metals, we have from Hund's rules and traditional ferrite theory [2,3] that

$$m_A = 10 - n_A \text{ and } m_B = 10 - n_B. \quad (2.5)$$

Using Eqs. (2.3)–(2.5), one can then obtain the following values:

$$n_A = 5.584, n_B = 5.692, m_A = 4.416, \text{ and } m_B = 4.308. \quad (2.6)$$

These values indicate that n_A and n_B , 5.584 and 5.692, respectively, are less than the values calculated using the DOSs, 5.975 and 6.089, and are obviously greater than the values of 5 (one Fe^{3+} at an (A) site per formula) and 5.5 (one Fe^{3+} and one Fe^{2+} at [B] sites), respectively, that would be expected based on the traditional viewpoint. The n_A and n_B values in Eq. (2.6) are very close to those calculated by Jeng et al. [65].

If other 3d electrons and all of the 4s electrons of the Fe cations were accepted by the O anions, then the average valences of the Fe cations at the (A) and [B] sites would be $+2.416$ ($=8-n_A$, since the total number of 3d and 4s electrons in one Fe atom is 8) and $+2.308$ ($=8-n_B$), respectively, where the values of n_A and n_B are those presented in Eq. (2.6). It is thus easy to obtain the ratios of Fe_A^{3+} to Fe_A^{2+} cations and Fe_B^{3+} to Fe_B^{2+} cations, $0.416/0.584$ and $0.308/0.692$, respectively. In other words, the number of Fe^{3+} cations for every Fe_3O_4 formula is only 1.032 ($=0.416+0.308 \times 2$), rather than 2 as in the traditional view. It is also easy to find the average valence of the O anions, which is -1.758 [$=-(2.416 + 2 \times 2.308)/4$], and therefore to determine that the ionicity of Fe_3O_4 is 0.879 ($=1.758/2$).

2.3.3. Estimation of the ionicities of $M\text{Fe}_2\text{O}_4$ spinel ferrites

According to the Phillips [39], Sr compounds exhibit the largest ionicities of the II–VI compounds. As in the following, by fitting to the ionicities of Sr compounds using the quantum-mechanical potential barrier model of Eq. (2.2), Ji et al. [63] reported a method of estimating the ionicities of $M\text{Fe}_2\text{O}_4$ spinel ferrites.

In such II–VI compounds, if only the first electron of a cation is ionized, f_i is simply 0.5. Accounting for the probability of ionizing the second electron, the ionicity can be estimated as

$$f_{IT} = 0.5 + 0.5 \times c_f \times R, \quad (2.7)$$

where R is calculated using Eq. (2.2), where P_C (P_D) represents the probability of the second electron of the cation jumping to the anions through the potential barrier of height V_C (V_D) and width r_C (r_D); V_C and V_D are the second ionization energies of the cations in the compound in question and the Sr compound, r_C and r_D are the effective radii of the anions in the compounds, and $c_v = 1.0$.

For oxides, such as SrO, one lets $R = 1.0$, and c_f is determined to be 0.852 by fitting the ionicity (0.926, see Table 5) of SrO from Phillips [39]. For SrS, SrSe, and SrTe, c_f was calculated to be 0.828, 0.834, and 0.806, respectively, by similar fitting of these compounds to their ionicities (see Table 5), as determined by Phillips. It can be seen that the differences between the various c_f values are very small. The ionicity values of these compounds, f_{IT} , calculated using Eqs. (2.2) and (2.7), as well as the parameters used in the calculation process, are listed in Table 5. Here, f_i and f_{i1} are the ionicities calculated by Pauling in 1932 and 1939, respectively; N is the ion coordination number in the compounds; V_C is the second ionization energy of the cations in the compound identified in column 1; V_D is the second ionization energy of Sr; and $r = r_C = r_D$ is the effective

Table 6

Ionicities of spinel ferrites, f_{IT} , as calculated by Ji et al. [63], where R is the probability ratio, between the ferrite in question and Fe_3O_4 , of the third electron in the cation jumping to the anions through the potential barrier with height V_C and width r , where V_C is the third ionization energy of the question cation and r is the effective radius of the O anion.

Material	f_{IT}	Cation total valence per formula	V_C (eV)	r (nm)	R
Mn_3O_4	0.8293	6.6343	33.67	0.144	0.6146
Fe_3O_4	0.8790	7.0320	30.65	0.144	1.0000
Co_3O_4	0.8314	6.6515	33.5	0.144	0.6313
Ni_3O_4	0.8129	6.5029	35.17	0.144	0.4873
Cu_3O_4	0.7990	6.3916	36.83	0.144	0.3795
Zn_3O_4	0.7822	6.2573	39.72	0.144	0.2493
Cr_3O_4	0.8726	6.9805	30.96	0.144	0.9501
MnFe_2O_4	0.8624	6.8994			
CoFe_2O_4	0.8631	6.9052			
NiFe_2O_4	0.8570	6.8556			
CuFe_2O_4	0.8523	6.8185			
ZnFe_2O_4	0.8467	6.7738			
CrFe_2O_4	0.8769	7.0148			

radius of the anions with coordination number N . The calculated f_{IT} values are close to the ionicities determined by Phillips and Pauling, indicating that Eq. (2.2) provides a reasonable method of estimating the ionicities of various compounds.

Similarly, f_{IT} of the $(\text{A})[\text{B}]_2\text{O}_4$ spinel ferrites can be calculated by fitting the ionicity of Fe_3O_4 (0.879). If $f_i = 1.00$, the eight electrons of the three Fe atoms should be ionized. If only two electrons per Fe atom are ionized, then $f_i = 0.75$. Therefore, the ionicity of spinel ferrites can be estimated using

$$f_{\text{IT}} = 0.75 + 0.25 \times c_f \times R. \quad (2.8)$$

For Fe_3O_4 , we let $R = 1.0$, and then $c_f = 0.516$ was obtained by fitting the ionicity of Fe_3O_4 (0.879). Consequently, the ionicities of the $M_3\text{O}_4$ ($M = \text{Cr}, \text{Mn}, \text{Co}, \text{Ni}, \text{or Cu}$) compounds could be calculated, which in turn could be considered to be the ionicities of the Cr, Mn, Co, Ni, or Cu ions in those ferrites.

The parameters used in these calculations and the results are listed in Table 6. In each case, R was calculated using Eqs. (2.2) and (2.8), c_v was set to 1.0, and V_C and V_D are the third ionization energies of the cations in the ferrites identified in column 1 and Fe, respectively. $r_C = r_D = 0.144$ nm is the effective radius of an O anion with a coordination number 12. Furthermore, these results may be extended to estimate the ionicities of $M\text{Fe}_2\text{O}_4$ ($M = \text{Cr}, \text{Mn}, \text{Co}, \text{Ni}, \text{or Cu}$) compounds, by averaging the ionicities of one M and two Fe cations. These ionicities are also shown in Table 6.

3. O 2p itinerant electron model for magnetic oxides (IEO model)

As mentioned in Section 1, a number of difficulties are faced when attempting to explain the magnetic ordering of oxides using the traditional magnetic SE and DE interaction models. In these models, all of the O anions are assumed to be O^{2-} ions; however, as shown in Section 2, the effect of O^{1-} ions (in addition to the O^{2-} ions) should be incorporated when considering magnetic oxides.

3.1. O 2p hole model: A simple introduction

The fact that there are O^{1-} ions in addition to O^{2-} ions has been proven through a number of important experiments. Nücker et al. [66] investigated the superconducting compounds $\text{YBa}_2\text{Cu}_3\text{O}_{7-y}$ with electron energy-loss spectroscopy (EELS) and found that the charge carriers in these compounds are holes in the O 2p band. Ibrahim et al. [67] analyzed X-ray absorption spectra (XAS) at the O K -edge and the photon-energy dependence of the O 1s, 2p Auger line at the O K -threshold, below the Mn $L_{2,3}$ edge, and at the Mn $L_{2,3}$ edge of the CMR manganites $\text{Pr}_{1-x}\text{Sr}_x\text{MnO}_3$ with $x = 0.0$ and 0.3. They also concluded that O 2p holes were present, the number of which increased with x . Papavassiliou et al. [68] compared NMR results with XAS data at the Mn K -edges of $\text{La}_{1-x}\text{Ca}_x\text{MnO}_{3+\delta}$ systems and observed the formation of a spin-polarized hole arrangement in the 2p O orbitals. Ju et al. [69] analyzed the O K -edge through EELS for $\text{La}_{1-x}\text{Sr}_x\text{MnO}_3$ ($0 \leq x \leq 0.7$) films grown epitaxially on (100) LaAlO_3 . They observed a prepeak corresponding to unoccupied states in the O 2p band and a correlation between the peak intensity and x . However, this prepeak was not observed for LaAlO_3 . It was thus concluded that these materials are charge-transfer-type oxides with carriers having significant O 2p hole characteristics. Subsequently, Alexandrov et al. [70] pointed out that the DE model is in conflict with these experimental results (EELS, XAS), which have shown unambiguously that the charge current carriers in ferromagnetic manganites are O 2p holes rather than 3d electrons.

3.2. IEO model

According to the assumption made in Section 2.2 that f_i is related to V_{alO} in oxides by $f_i = |V_{\text{alO}}|/2$ and the fact that the ionicities of several monoxides decrease with increasing second ionization energy of the cations, as shown in Fig. 4(a) [39] and Fig. 6 [58] and the results reported by Ju et al. [69] can be explained as follows.

Since O^{1-} anions (with O 2p holes) were found in LaMnO_3 , while no O^{1-} anions were found in LaAlO_3 [69] due to the third ionization energy of Mn (33.67 eV) being higher than that of Al (28.45 eV), it can be concluded that a Mn cation is less likely to lose its third electron than an Al cation. This characteristic suggests that the average valence of Mn is less than +3 and that both Mn^{2+} and Mn^{3+} cations are present in LaMnO_3 . Furthermore, it can be assumed that there are no Mn^{4+} cations in perovskite manganites, since $V_{4i} = 51.2$ eV for Mn, which makes it virtually impossible for an Mn cation to lose its fourth electron (see Fig. 4(b)). This argument is crucial to the understanding of the magnetic ordering in perovskite manganites, such as $\text{La}_{1-x}\text{Sr}_x\text{MnO}_3$ and $\text{Pr}_{1-x}\text{Sr}_x\text{MnO}_3$. Similarly, since V_{4i} is between 43.3 eV and 55.2 eV for the transition metals from Ti to Cu, there should be no +4 valence cations of these elements in ABO_3 perovskite manganites.

Accounting for the requirement that some of the O ions present in oxides are O^{1-} anions [55–59], Tang et al. proposed the IEO model to explain the magnetic structures of spinel ferrites [71] and ABO_3 perovskite manganites [72]. The IEO model, which is closely related to the O 2p hole charge carrier model [70] mentioned above, but with more attention paid to the electron spin, is based on the following four postulates.

(i) The outer orbits of O^{1-} anions contain O 2p holes. Thus, in a given sublattice, an O 2p electron with a constant spin direction can hop from an O^{2-} anion to the O 2p hole of an adjacent O^{1-} anion with a metal cation acting as an intermediary. This hopping process can, of course, also be understood as 2p hole hopping in the opposite direction.

We consider the reasons for this feature to be the electron affinity energy of O and the ionization energies of the cations. The second electron affinity energy of O is 8.08 eV, while the second and third ionization energies of 3d transition metals (from Ti to Zn) are between 13.58 eV and 39.72 eV. These values, which are valid for free atoms, must affect how ions gain and lose electrons in oxides and result in the itinerant electron originating as an O 2p electron from the O anions rather than as a 3d electron from the metal cations in spinel ferrites and perovskite manganites [70].

(ii) The two O 2p electrons in the outer orbit of an O^{2-} anion, which have opposite spin directions, become itinerant electrons in the two different sublattices, such as, (A) or [B] sites of spinel ferrites. This restriction arises since the spin direction of the itinerant electron remains constant throughout the hopping process in a given sublattice [22], so the two O 2p electrons with opposite spin directions in the outer orbit of an O^{2-} anion must belong to the two different sublattices of the magnetic oxides. In other words, in magnetic oxides, the itinerant electrons must have opposite spin directions in the two sublattices.

(iii) In a given sublattice, since they are constrained by Hund's rules [2] and because an itinerant electron has a constant spin direction, the magnetic moments of cations with 3d electron numbers $n_d \leq 4$ (such as Mn^{3+} or divalent/trivalent Ti or Cr cations), will be antiparallel to those of the cations with $n_d \geq 5$ (such as Mn^{2+} or divalent/trivalent Fe, Co, or Ni cations) whether at the (A) or [B] sites.

(iv) In the itinerating process of an electron, if the electron passes through the highest energy level of the intermediary cation (for example, $\text{Mn}^{3+}(3d^4)$ in ABO perovskite manganites or $\text{Fe}^{3+}(3d^5)$ in (A)[B] $_2\text{O}_4$ spinel ferrites), it will expend only a small amount of energy of the system. Otherwise, it will expend more energy. This behavior may be the reason that the average molecular magnetic moments and T_C decrease rapidly and present the cant magnetic structures, since the Fe content is less than 2.0 in (A)[B] $_2\text{O}_4$ spinel ferrites and since the Mn cations are substituted by other cations in ABO_3 perovskite manganites. These features will be discussed in Sections 4.5, 4.6, 5.3 and 5.4.

Thus, the magnetic ordering in a given sublattice is dependent on the number of 3d electrons, including both the local and the itinerant 3d electrons in the cations, and moreover, is subject to constraints arising from Hund's rules [2]. For example, in the 3d subshell of a transition metal atom, a maximum of five electrons can have their spins aligned in one direction. Since $n_d \leq 4$ for Mn^{3+} and divalent/trivalent Cr and Ti cations, when an itinerant electron hops to a Mn^{3+} (or Cr, Ti) cation in a spinel ferrite, the spin direction of this itinerant electron must be parallel to the direction of the local 3d electrons (majority spins). However, when an itinerant electron hops to a Mn^{2+} cation or a divalent/trivalent Fe, Co, Ni, or Cu cation (where $n_d \geq 5$), the spin direction of this itinerant electron must be antiparallel to the direction of the local 3d electrons. Therefore, whether at the [B] or (A) sites of the spinel ferrite, the magnetic moment directions of the Mn^{3+} (and divalent/trivalent Cr or Ti) cations must be antiparallel to those of the cations with $n_d \geq 5$, because the spin direction of the itinerant electron remains constant during the hopping process [71,72].

As an example, we discuss the transition of an itinerant electron along an ion chain as shown in Fig. 7. In Fig. 7, an arrow drawn on a 3d energy level represents an electron with a specific spin direction. Δ represents a 2p hole, which in the illustrated case represents the absence of a spin-up electron. A spin-up O 2p electron is assumed to hop along the bonds $\text{O}^{\downarrow\uparrow}-\text{Mn}^{2+}-\text{O}^{\downarrow\uparrow}-\text{Mn}^{3+}-\text{O}^{\downarrow\Delta}$, as shown in Fig. 7(a). An itinerant electron can hop from the middle O ion to the 2p hole of the right O ion via Mn^{3+} , as depicted in Fig. 7(b), yielding the state $\text{O}^{\downarrow\uparrow}-\text{Mn}^{2+}-\text{O}^{\downarrow\Delta}-\text{Mn}^{3+}-\text{O}^{\downarrow\uparrow}$, as illustrated in Fig. 7(c). Alternatively, an O 2p electron can hop from the left O ion to the middle O ion via Mn^{2+} , as shown in Fig. 7(d), yielding the $\text{O}^{\downarrow\Delta}-\text{Mn}^{2+}-\text{O}^{\downarrow\uparrow}-\text{Mn}^{3+}-\text{O}^{\downarrow\uparrow}$ state, as depicted in Fig. 7(e). In contrast, if the magnetic moment direction of the Mn^{2+} cation is parallel to that of the Mn^{3+} cation, a spin-up itinerant electron cannot hop from the left O ion to the middle O via Mn^{2+} , as illustrated in Fig. 7(f), since it is subject to constraints arising from Hund's rules, i.e., no two electrons with the same spin direction can be present in the same energy level.

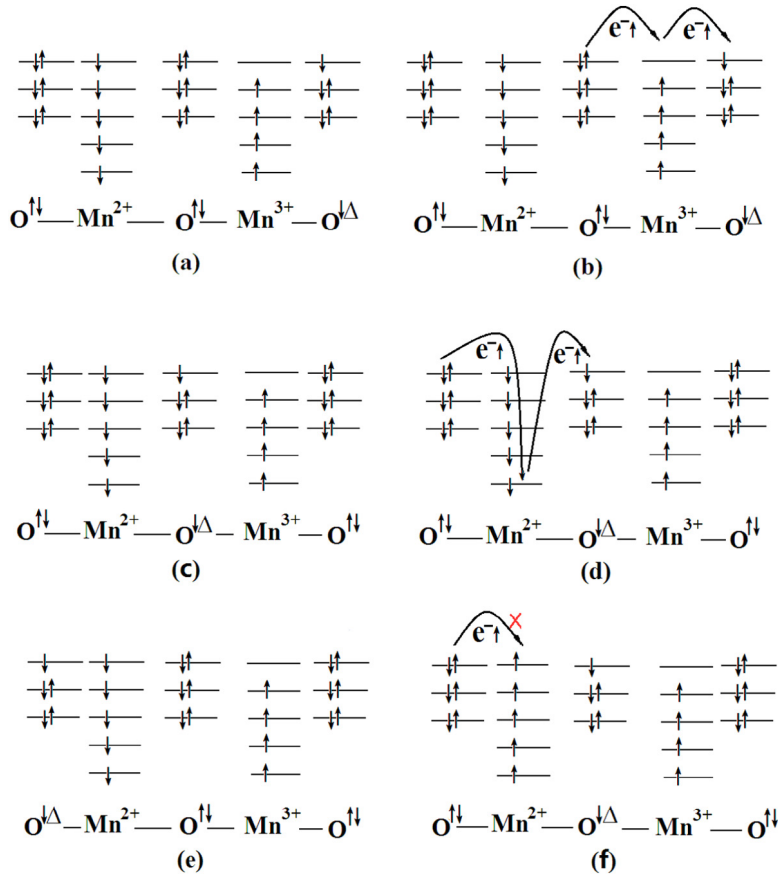


Fig. 7. (a)–(e) An itinerant electron with spin up can transit in a given sublattice only when the direction of the magnetic moment of Mn²⁺ is antiparallel to that of the magnetic moment of Mn³⁺. (f) Transitions are prevented when the direction of the magnetic moment of Mn²⁺ is parallel to that of the magnetic moment of Mn³⁺ (cf. Xu et al. [71]). An arrow drawn on a 3d energy level represents an electron with a specific spin direction. Δ represents a 2p hole, which in the illustrated case represents the absence of a spin-up electron.

The difference between Figs. 7(b)–7(d) should be carefully noted. Kisker et al. [73] investigated the spin- and angle-resolved photoemission spectra of Fe. They found that the valence electrons were distributed in a region with an energy ~ 6 eV, while the spin-down (minority spin) electrons were distributed near the Fermi level, as shown in Fig. 8. Johnson [74] reviewed the spin-polarized photoemission investigations and obtained many similar results. However, the Fermi energy level should correspond to the highest energy level when the spin direction is up, which is precisely why the paths of the itinerant electrons in Figs. 7(b)–7(d) are different. When a spin-up electron hops between the O²⁻–Mn³⁺–O¹⁻ bonds, as shown in Fig. 7(b), it expends little energy; however, when it hops between the O²⁻–Mn²⁺–O¹⁻ bonds, as shown in Fig. 7(d), it must expend more energy, resulting in a lower transition probability. This fact will be used to discuss the T_C variation of the magnetic oxides in Section 5.1.

The IEO model could be used to explain the magnetic structures of not only Co-, Ni-, and Cu-doped spinel ferrites, but also Cr-, Mn-, and Ti-doped spinel ferrites and ABO₃ perovskite manganites, as we will see in Sections 4 and 5.

4. Applications of the IEO model to spinel ferrites

In this section, we consider the application of the IEO model to spinel ferrites and the experimental evidence supporting this model.

4.1. Cation distributions and magnetic moment directions in Cr- and Co-substituted spinel ferrites Ni_{0.7}Fe_{2.3}O₄

Ferrite powder samples, which were labeled as CrNi, CoNi, and CrFe, with nominal compositions of Cr_xNi_{0.7-x}Fe_{2.3}O₄ (0.0 $\leq x \leq 0.3$), Co_xNi_{0.7-x}Fe_{2.3}O₄ (0.0 $\leq x \leq 0.3$), and Cr_xNi_{0.7}Fe_{2.3-x}O₄ (0.0 $\leq x \leq 0.3$), respectively, were synthesized via the chemical co-precipitation method [75]. Analysis of the XRD data taken from each sample indicated that each one had

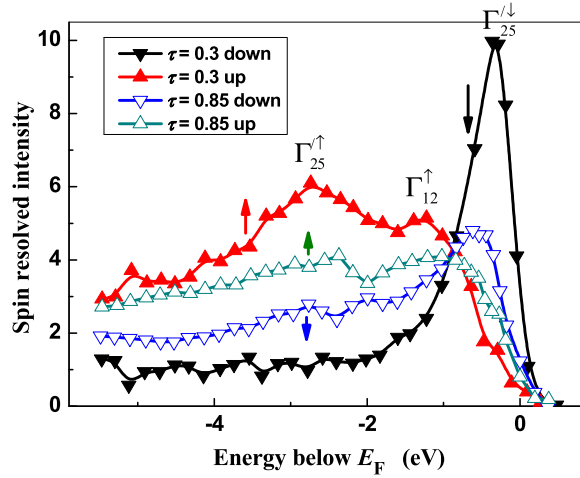


Fig. 8. Spin- and angle-resolved photoemission spectra for Fe metal (from Kisker et al. [73]), where $\tau = T/T_C$, T and T_C represent the test temperature and Curie temperature. The arrows represent the spin directions of the electrons.

Table 7

Rietveld fitting results for the XRD diffraction patterns for the three series of samples, $\text{Co}_x\text{Ni}_{0.7-x}\text{Fe}_{2.3}\text{O}_4$, $\text{Cr}_x\text{Ni}_{0.7-x}\text{Fe}_{2.3}\text{O}_4$, and $\text{Cr}_x\text{Ni}_{0.7}\text{Fe}_{2.3-x}\text{O}_4$. Here, a is the lattice parameter; d_{AO} and d_{BO} are the distances from the O anion to the cations at the (A) and [B] sites, respectively, and d_{AB} is the distance from the cations at the (A) sites to those at the [B] sites (from Xue et al. [75]).

x	a (Å)	d_{AO} (Å)	d_{BO} (Å)	d_{AB} (Å)
$\text{Co}_x\text{Ni}_{0.7-x}\text{Fe}_{2.3}\text{O}_4$				
0.00	8.3483	1.894	2.038	3.461
0.10	8.3547	1.896	2.040	3.464
0.20	8.3587	1.897	2.041	3.465
0.30	8.3645	1.898	2.042	3.468
$\text{Cr}_x\text{Ni}_{0.7-x}\text{Fe}_{2.3}\text{O}_4$				
0.00	8.3489	1.894	2.038	3.461
0.15	8.3573	1.896	2.040	3.465
0.25	8.3592	1.897	2.041	3.466
0.30	8.3622	1.897	2.042	3.467
$\text{Cr}_x\text{Ni}_{0.7}\text{Fe}_{2.3-x}\text{O}_4$				
0.00	8.3517	1.895	2.039	3.462
0.05	8.3491	1.894	2.038	3.461
0.10	8.3472	1.894	2.038	3.461
0.15	8.3473	1.894	2.038	3.461
0.20	8.3453	1.894	2.037	3.460
0.25	8.3433	1.893	2.037	3.459
0.30	8.3412	1.893	2.036	3.458

a single-phase cubic spinel structure, $(\text{A})[\text{B}]_2\text{O}_4$, and since the volume-averaged crystallite sizes of all of the samples were larger than 100 nm, the surface effects of the crystallites were expected to be very weak.

As outlined in Section 1.2.1, by analyzing the XRD data, the crystal lattice constant a , the distances d_{AO} , d_{BO} , and d_{AB} for these samples were obtained and are listed in Table 7. For the CrFe samples, a decreases with the Cr doping level x , while it increases with the doping level for the CrNi and CoNi samples. Also, while the observed average values of d_{AO} and d_{BO} were 1.05 and 0.98 times the ideal values, respectively, the observed value of d_{AB} was equal to its ideal value for all three series of samples, i.e.,

$$d_{AO} = 1.05 \times \frac{\sqrt{3}}{8}a, \quad d_{BO} = 0.98 \times \frac{1}{4}a, \quad \text{and} \quad d_{AB} = \frac{\sqrt{11}}{8}a. \quad (4.1)$$

The magnetic measurements shown in Fig. 9 were taken at $T = 10$ K and indicate that the magnetic moments (μ_{obs}), for the CoNi samples increases with x . However, for the CrNi and CrFe samples, μ_{obs} decreases with increasing x . As is evident from Fig. 9, the slope of the curve for the CrFe samples is greater than that of the curve for the CrNi samples. In the figure, the points represent the observed values, while the curves represent a fit resulting from using the IEO model. In the fitting process, the following five factors were taken into account:

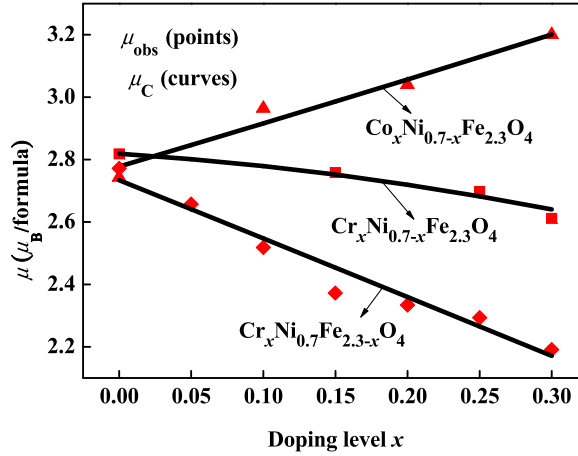


Fig. 9. Observed and fitted magnetic moment, μ_{obs} (points) and μ_{C} (curves), as functions of x for the spinel ferrites $\text{Cr}_x\text{Ni}_{0.7-x}\text{Fe}_{2.3}\text{O}_4$, $\text{Co}_x\text{Ni}_{0.7-x}\text{Fe}_{2.3}\text{O}_4$, and $\text{Cr}_x\text{Ni}_{0.7}\text{Fe}_{2.3-x}\text{O}_4$ (from Xue et al. [75]).

(i) The content ratio, R , of the different cations in the samples was estimated using Eq. (2.2).

(ii) The Pauli repulsion energy of the electron cloud between adjacent cations and anions was taken into account by considering the effective ionic radius [76], which implies that smaller ions should be located at the sites with less available space in the crystal lattice. Notably, the volume of space surrounding the (A) sites is smaller than that surrounding the [B] sites in spinel ferrites.

(iii) In the thermal treatment process for each sample, due to the fact that the cations at the (A) and [B] sites have four and six adjacent O ions, respectively, a tendency toward achieving a charge density balance forces some of the divalent cations (which have large effective ionic radii) to enter the (A) sites (which have less available space) from the [B] sites (which have more available space) by traversing an equivalent potential barrier V_{BA} . V_{BA} depends on the ionization energy, ionic radius, and thermal treatment temperature and was assumed to have the form

$$V_{\text{BA}}(\text{Ni}^{2+}) = \frac{V_{\text{BA}}(M^{2+})V(\text{Ni}^{3+})r(\text{Ni}^{2+})}{V(M^{3+})r(M^{2+})} \quad (4.2)$$

and

$$V_{\text{BA}}(\text{Fe}^{2+}) = \frac{V_{\text{BA}}(M^{2+})V(\text{Fe}^{3+})r(\text{Fe}^{2+})}{V(M^{3+})r(M^{2+})}, \quad (4.3)$$

where $r(M^{2+})$, $r(\text{Ni}^{2+})$, and $r(\text{Fe}^{2+})$ are the effective radii [76] of the Cr^{2+} (Co^{2+}), Ni^{2+} , and Fe^{2+} cations, respectively, and $V(M^{3+})$, $V(\text{Ni}^{3+})$, and $V(\text{Fe}^{3+})$ are the third ionization energies of the Cr (Co), Ni, and Fe cations, respectively, as shown in Table 4.

(iv) The ionicity of the ions in the oxides (see Table 6) [63] caused both the total valence and the total number of trivalent cations per formula N_3 to be less than the assumed traditional values of 8 and 2, respectively, in the (A)[B]₂O₄ spinel ferrites.

(v) As mentioned in Section 3, according to the IEO model, the magnetic moment directions of Cr^{3+} and Cr^{2+} are antiparallel to those of the divalent and trivalent Fe, Co, and Ni cations, whether at (A) or [B] sites [71].

The chemical formulas for the ferrite samples $\text{Co}_x\text{Ni}_{0.7-x}\text{Fe}_{2.3}\text{O}_4$, $\text{Cr}_x\text{Ni}_{0.7-x}\text{Fe}_{2.3}\text{O}_4$, and $\text{Cr}_x\text{Ni}_{0.7}\text{Fe}_{2.3-x}\text{O}_4$ are rewritten here as $M_{x_1}\text{Ni}_{x_2}\text{Fe}_{3-x_1-x_2}\text{O}_4$. In this way, the cation distributions can be described by the formula

$$(M_{y_1}^{3+}\text{Ni}_{y_2}^{3+}\text{Fe}_{y_3}^{3+}M_{y_4}^{2+}\text{Ni}_{y_5}^{2+}\text{Fe}_{y_6}^{2+})[M_{x_1-y_1-y_4-z_1}^{2+}\text{Ni}_{x_2-y_2-y_5-z_2}^{2+}\text{Fe}_{3-x_1-x_2-y_3-y_6-z_3}^{2+}M_{z_1}^{3+}\text{Ni}_{z_2}^{3+}\text{Fe}_{z_3}^{3+}]\text{O}_4. \quad (4.4)$$

It can be seen from Eq. (4.4) that the following conditions hold:

$$y_1 + y_2 + y_3 + y_4 + y_5 + y_6 = 1 \quad (4.5)$$

and

$$y_1 + y_2 + y_3 + z_1 + z_2 + z_3 = N_3. \quad (4.6)$$

N_3 may also be written in terms of the ionicities as

$$N_3 = \frac{8}{3} [f_M x_1 + f_{\text{Ni}} x_2 + f_{\text{Fe}} (3.0 - x_1 - x_2)] - 6.0, \quad (4.7)$$

where f_{Fe} , f_M (f_{Cr} , f_{Co}), and f_{Ni} represent the ionicities (see Table 6) of the Fe, Cr (Co), and Ni ions, respectively. From Eq. (4.4), one then has

$$R_{A1} \frac{x_1}{3 - x_1 - x_2} = \frac{y_1}{y_3}, \quad R_{A2} \frac{x_2}{3 - x_1 - x_2} = \frac{y_2}{y_3}, \quad R_{A4} \frac{x_1}{3 - x_1 - x_2} = \frac{y_4}{y_3}, \quad (4.8)$$

$$R_{A5} \frac{x_2}{3 - x_1 - x_2} = \frac{y_5}{y_3}, \quad R_{A6} = \frac{y_6}{y_3},$$

$$R_{B1} \frac{x_1 - y_1 - y_4}{3 - x_1 - x_2 - y_3 - y_6} = \frac{z_1}{z_3}, \quad \text{and} \quad R_{B2} \frac{x_2 - y_2 - y_5}{3 - x_1 - x_2 - y_3 - y_6} = \frac{z_2}{z_3}, \quad (4.9)$$

where R_{A1} , R_{A2} , R_{A4} , R_{A5} , and R_{A6} are the probability ratios of M^{3+} (Cr^{3+} , Co^{3+}), Ni^{3+} , M^{2+} (Cr^{2+} , Co^{2+}), Ni^{2+} , and Fe^{2+} ions, respectively, with respect to the Fe^{3+} ions at the (A) sites. Similarly, R_{B1} and R_{B2} are the probability ratios of the M^{3+} (Cr^{3+} , Co^{3+}) and Ni^{3+} ions, respectively, with respect to the Fe^{3+} ions at the [B] sites.

From Eqs. (4.5) and (4.8), y_3 can be rewritten as

$$y_3 = \frac{3 - x_1 - x_2}{(R_{A1} + R_{A4})x_1 + (R_{A2} + R_{A5})x_2 + (1 + R_{A6})(3 - x_1 - x_2)}, \quad (4.10)$$

and from Eqs. (4.6) and (4.9), z_3 can be expressed as

$$z_3 = \frac{N_3 - \left[1 + R_{A1} \frac{x_1}{3 - x_1 - x_2} + R_{A2} \frac{x_2}{3 - x_1 - x_2}\right] y_3}{1 + R_{B1} \frac{x_1 - y_1 - y_4}{3 - x_1 - x_2 - y_3 - y_6} + R_{B2} \frac{x_2 - y_2 - y_5}{3 - x_1 - x_2 - y_3 - y_6}}. \quad (4.11)$$

According to the quantum-mechanical potential barrier model for estimating the cation distributions in spinel ferrites (cf. Eq. (2.2)), R_{A1} , R_{A2} , R_{A4} , R_{A5} , R_{A6} , R_{B1} , and R_{B2} can be derived as follows:

$$R_{A1} = \frac{P(M^{3+})}{P(\text{Fe}^{3+})} = \frac{V(\text{Fe}^{3+})}{V(M^{3+})} \exp \left\{ 10.24 d_{\text{AO}} \left[V(\text{Fe}^{3+})^{1/2} - V(M^{3+})^{1/2} \right] \right\}, \quad (4.12)$$

$$R_{A2} = \frac{P(\text{Ni}^{3+})}{P(\text{Fe}^{3+})} = \frac{V(\text{Fe}^{3+})}{V(\text{Ni}^{3+})} \exp \left\{ 10.24 d_{\text{AO}} \left[V(\text{Fe}^{3+})^{1/2} - V(\text{Ni}^{3+})^{1/2} \right] \right\}, \quad (4.13)$$

$$R_{A4} = \frac{P(M^{2+})}{P(\text{Fe}^{3+})} = \frac{V(\text{Fe}^{3+})}{V(M^{2+})} \exp \left\{ 10.24 \left[d_{\text{AO}} V(\text{Fe}^{3+})^{1/2} - d_{\text{AO}} V(M^{2+})^{1/2} - d_{\text{AB}} V_{\text{BA}}(M^{2+})^{1/2} \right] \right\}, \quad (4.14)$$

$$R_{A5} = \frac{P(\text{Ni}^{2+})}{P(\text{Fe}^{3+})} = \frac{V(\text{Fe}^{3+})}{V(\text{Ni}^{2+})} \exp \left\{ 10.24 \left[d_{\text{AO}} V(\text{Fe}^{3+})^{1/2} - d_{\text{AO}} V(\text{Ni}^{2+})^{1/2} - d_{\text{AB}} V_{\text{BA}}(\text{Ni}^{2+})^{1/2} \right] \right\}, \quad (4.15)$$

$$R_{A6} = \frac{P(\text{Fe}^{2+})}{P(\text{Fe}^{3+})} = \frac{V(\text{Fe}^{3+})}{V(\text{Fe}^{2+})} \exp \left\{ 10.24 \left[d_{\text{AO}} V(\text{Fe}^{3+})^{1/2} - d_{\text{AO}} V(\text{Fe}^{2+})^{1/2} - d_{\text{AB}} V_{\text{BA}}(\text{Fe}^{2+})^{1/2} \right] \right\}, \quad (4.16)$$

$$R_{B1} = \frac{P(M^{3+})}{P(\text{Fe}^{3+})} = \frac{V(\text{Fe}^{3+})}{V(M^{3+})} \exp \left\{ 10.24 d_{\text{BO}} \left[V(\text{Fe}^{3+})^{1/2} - V(M^{3+})^{1/2} \right] \right\}, \quad (4.17)$$

and

$$R_{B2} = \frac{P(\text{Ni}^{3+})}{P(\text{Fe}^{3+})} = \frac{V(\text{Fe}^{3+})}{V(\text{Ni}^{3+})} \exp \left\{ 10.24 d_{\text{BO}} \left[V(\text{Fe}^{3+})^{1/2} - V(\text{Ni}^{3+})^{1/2} \right] \right\}, \quad (4.18)$$

where $M = \text{Cr}$ or Co and V (M^{2+}), V (M^{3+}), V (Ni^{2+}), V (Ni^{3+}), V (Fe^{2+}), and V (Fe^{3+}) are the second and third ionization energies of Cr or Co, Ni, and Fe, respectively (see Table 4). Likewise, $V_{\text{BA}}(M^{2+})$, $V_{\text{BA}}(\text{Ni}^{2+})$, and $V_{\text{BA}}(\text{Fe}^{2+})$ are the heights of the equivalent potential barriers, all of width d_{AB} , that must be overcome by the M^{2+} , Ni^{2+} , and Fe^{2+} ions as they move from the [B] sites to the (A) sites during the thermal treatment process (the values of d_{AO} , d_{BO} , and d_{AB} are taken from Table 7).

As stated in point (v) above, according to the IEO model, the magnetic moment directions of Cr^{3+} and Cr^{2+} are antiparallel to those of the Co^{3+} , Co^{2+} , Ni^{3+} , Ni^{2+} , Fe^{3+} , and Fe^{2+} ions in the same sublattice [71]. Thus, the magnetic moments of the M^{2+} , M^{3+} , Ni^{2+} , Ni^{3+} , Fe^{2+} , and Fe^{3+} ions can be written as m_2 , m_3 , $2 \mu_{\text{B}}$, $3 \mu_{\text{B}}$, $4 \mu_{\text{B}}$, and $5 \mu_{\text{B}}$, respectively, where $m_2 = -4 \mu_{\text{B}}$ and $m_3 = -3 \mu_{\text{B}}$ for $M = \text{Cr}$, while $m_2 = 3 \mu_{\text{B}}$ and $m_3 = 4 \mu_{\text{B}}$ for $M = \text{Co}$. Therefore, the average magnetic moment per

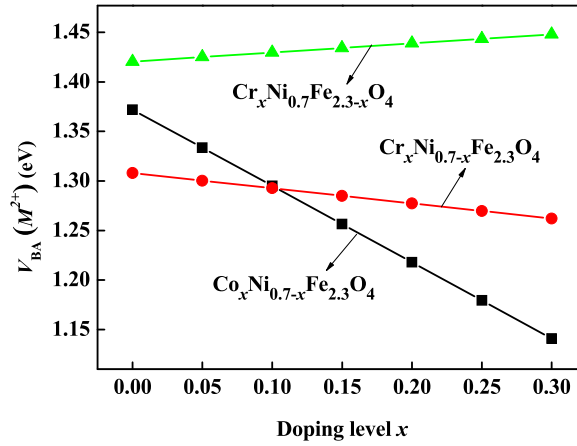


Fig. 10. Dependence of the equivalent potential barrier height, $V_{BA}(M^{2+})$, on the doping level x for the three series of samples (from Xue et al. [75]). Where $M = \text{Cr}$, Cr and Co , for CrFe , CrNi and CoNi sample, respectively.

formula in $M_{x_1}\text{Ni}_{x_2}\text{Fe}_{3-x_1-x_2}\text{O}_4$ samples can be determined from Eq. (4.4):

$$\left. \begin{aligned} \mu_C &= \mu_{BT} - \mu_{AT} \\ \mu_{AT} &= m_3y_1 + 3y_2 + 5y_3 + m_2y_4 + 2y_5 + 4y_6, \\ \mu_{B1} &= m_2(x_1 - y_1 - y_4 - z_1) + m_3z_1, \\ \mu_{B2} &= 2(x_2 - y_2 - y_5 - z_2) + 3z_2 = 2(x_2 - y_2 - y_5) + z_2, \\ \mu_{B3} &= 4(3 - x_1 - x_2 - y_3 - y_6 - z_3) + 5z_3 = 4(3 - x_1 - x_2 - y_3 - y_6) + z_3, \end{aligned} \right\} \quad (4.19)$$

and

$$\mu_{BT} = \mu_{B1} + \mu_{B2} + \mu_{B3},$$

where μ_C is the calculated magnetic moment per formula of the sample; μ_{AT} and μ_{BT} are the magnetic moments of the (A) and [B] sublattices, respectively; and μ_{B1} , μ_{B2} , and μ_{B3} are the magnetic moments of the Cr (Co), Ni, and Fe ions, respectively, at the [B] sites.

Altogether, there are 20 independent equations to be considered: Eqs. (4.2), (4.3), (4.5)–(4.9), and (4.12)–(4.19), where Eq. (4.8) contains five equations and Eq. (4.9) contains two equations. There are also 21 parameters in these equations: y_1 – y_6 , z_1 – z_3 , N_3 , R_{A1} , R_{A2} , R_{A4} , R_{A5} , R_{A6} , R_{B1} , R_{B2} , $V_{BA}(M^{2+})$, $V_{BA}(\text{Ni}^{2+})$, $V_{BA}(\text{Fe}^{2+})$, and μ_C for each value of x . Therefore, for a given sample, it is necessary to obtain a value for at least one independent parameter to fit μ_{obs} .

However, if all of the samples in a series are considered, then there are only two independent fitting parameters when it is assumed that $V_{BA}(M^{2+})$ varies linearly with the doping level, as shown in Fig. 10. The resulting data for CoNi, CrNi, and CrFe sample series are shown in Tables 8–10, respectively. The fitted dependences of the magnetic moments on x at 10 K for the three series of samples are shown in Fig. 9. It can be seen that the fitted magnetic moments μ_C (curves) are very close to their experimental values μ_{obs} (points) as a function of x for the three series of samples. The resulting cation distributions of the CoNi, CrNi, and CrFe series of samples are shown in Figs. 11–13.

4.2. Discussion of the magnetic structures and cation distributions in $M_x\text{Ni}_{1-x}\text{Fe}_2\text{O}_4$ ferrites

To date, Tang et al. have examined the cation distributions of several series of spinel ferrites $M_x\text{Ni}_{1-x}\text{Fe}_2\text{O}_4$ ($M = \text{Cr}$ or Mn , $N = \text{Fe}$, Co , Ni and Cu) by fitting the magnetic moments measured at 10 K using the method outlined above [64,71,77–80]. It is very interesting to compare these results. The dependences of μ_{obs} and μ_C on x are shown in Fig. 14 for the ferrite samples $\text{Cr}_x\text{Fe}_{3-x}\text{O}_4$ [64], $\text{Cr}_x\text{Co}_{1-x}\text{Fe}_2\text{O}_4$ [77], $\text{Cr}_x\text{Ni}_{1-x}\text{Fe}_2\text{O}_4$ [78], $\text{Cu}_{x_1}\text{Cr}_{x_2}\text{Fe}_{3-x_1-x_2}\text{O}_4$ ($0.0 \leq x_1 \leq 0.284$ with $1.04 \geq x_2 \geq 0.656$) [79], and $\text{Mn}_x\text{Ni}_{1-x}\text{Fe}_2\text{O}_4$ [71]. It can be seen that the fitted curves are very close to the observed values (points) for all of these samples, regardless of whether the samples contain Cr or Mn.

Table 11 lists the data used in the fitting process, as well as the data obtained for the $M\text{Fe}_2\text{O}_4$ samples ($M = \text{Cr}$, Mn , Fe , Co , or Ni). Here, $r_2(M^{2+})$ is the effective radius of the divalent M cations with a coordination number of 6 [76]; $V(M^{2+})$ and $V(M^{3+})$ are the second and third ionization energies (as shown in Table 4), respectively; μ_{m2} and μ_{m3} are the magnetic moments of the M^{2+} and M^{3+} cations, respectively, where the negative signs in the magnetic moments for the Cr^{2+} , Cr^{3+} , and Mn^{3+} cations represent the fact that their magnetic moments are antiparallel to those of Fe (Co, Ni, Cu). d_{AO} , d_{BO} , and d_{AB} are the lengths of the A–O, B–O, and A–B bonds, respectively, measured by performing XRD at room temperature; μ_{obs} and μ_C are the observed (measured at 10 K) and fitted magnetic moments per formula of the samples, respectively; f_i is the ionicity (as shown in Table 6) of the M cations in the spinel ferrites; and N_3 is the number of trivalent cations per formula calculated taking the ionicity into consideration, which is distinctly less than the value of 2 used in the conventional view. T_{TH} is the thermal treatment temperature employed during sample preparation.

Table 8

Cation distributions obtained by fitting the dependence of the magnetic moments of the $\text{Co}_x\text{Ni}_{0.7-x}\text{Fe}_{2.3}\text{O}_4$ samples on x . Here, $V_{\text{BA}}(\text{Co}^{2+})$, $V_{\text{BA}}(\text{Ni}^{2+})$ and $V_{\text{BA}}(\text{Fe}^{2+})$ are the heights of the potential barriers that must be jumped by the Co^{2+} , Ni^{2+} , and Fe^{2+} ions when moving from the [B] sites to the (A) sites during the thermal treatment of the sample; N_3 is the total number of trivalent cations per formula. μ_{C} and μ_{obs} are the fitted and observed values of the sample magnetic moments at 10 K (from Xue et al. [75]).

x	0.0	0.1	0.2	0.3
N_3	0.9086	0.9137	0.9186	0.9233
$V_{\text{BA}}(\text{Co}^{2+})$ (eV)	1.3720	1.2950	1.2180	1.1410
$V_{\text{BA}}(\text{Ni}^{2+})$ (eV)	1.3341	1.2592	1.1843	1.1094
$V_{\text{BA}}(\text{Fe}^{2+})$ (eV)	1.3143	1.2405	1.1667	1.0930
A sites				
Co^{3+}	0.0000	0.0126	0.0237	0.0334
Ni^{3+}	0.0669	0.0544	0.0428	0.0321
Fe^{3+}	0.5428	0.5150	0.4863	0.4566
Co^{2+}	0.0000	0.0109	0.0233	0.0372
Ni^{2+}	0.0552	0.0504	0.0447	0.0380
Fe^{2+}	0.3351	0.3567	0.3792	0.4026
B sites				
Co^{2+}	0.0000	0.0682	0.1349	0.2000
Ni^{2+}	0.5377	0.4574	0.3782	0.3000
Fe^{2+}	1.1633	1.1427	1.1212	1.0987
Co^{3+}	0.0000	0.0083	0.0180	0.0294
Ni^{3+}	0.0401	0.0378	0.0344	0.0298
Fe^{3+}	0.2588	0.2856	0.3134	0.3420
μ_{C} (μ_{B} /formula)	2.7778	2.9159	3.0570	3.2008
μ_{obs} (μ_{B} /formula)	2.7426	2.9635	3.0397	3.2001

Table 9

Cation distributions obtained by fitting the dependence of the magnetic moments of the $\text{Cr}_x\text{Ni}_{0.7-x}\text{Fe}_{2.3}\text{O}_4$ samples on x . Here, $V_{\text{BA}}(\text{Cr}^{2+})$, $V_{\text{BA}}(\text{Ni}^{2+})$, and $V_{\text{BA}}(\text{Fe}^{2+})$ are the heights of the potential barriers that must be jumped by the Cr^{2+} , Ni^{2+} , and Fe^{2+} ions when moving from the [B] sites to the (A) sites during the thermal treatment of the samples; N_3 is the total number of trivalent cations per formula. μ_{C} and μ_{obs} are the fitted and observed values of the sample magnetic moments at 10 K (from Xue et al. [75]).

x	0.00	0.15	0.25	0.30
N_3	0.9086	0.9326	0.9483	0.9563
$V_{\text{BA}}(\text{Cr}^{2+})$ (eV)	1.3080	1.2850	1.2697	1.2620
$V_{\text{BA}}(\text{Ni}^{2+})$ (eV)	1.2816	1.2590	1.2440	1.2365
$V_{\text{BA}}(\text{Fe}^{2+})$ (eV)	1.2625	1.2403	1.2255	1.2181
A sites				
Cr^{3+}	0.0000	0.0307	0.0496	0.0587
Ni^{3+}	0.0648	0.0486	0.0385	0.0337
Fe^{3+}	0.5257	0.5021	0.4871	0.4798
Cr^{2+}	0.0000	0.0260	0.0431	0.0516
Ni^{2+}	0.0580	0.0450	0.0366	0.0324
Fe^{2+}	0.3516	0.3476	0.3451	0.3439
B sites				
Cr^{2+}	0.0000	0.0754	0.1261	0.1515
Ni^{2+}	0.5346	0.4207	0.3446	0.3064
Fe^{2+}	1.1472	1.1528	1.1562	1.1578
Cr^{3+}	0.0000	0.0179	0.0312	0.0382
Ni^{3+}	0.0426	0.0357	0.0303	0.0274
Fe^{3+}	0.2755	0.2976	0.3116	0.3185
μ_{C} (μ_{B} /formula)	2.8186	2.7520	2.6822	2.6402
μ_{obs} (μ_{B} /formula)	2.8183	2.7584	2.6977	2.6114

It should be noted that $V_{\text{BA}}(M^{2+})$ is the height of the equivalent potential barrier that must be transited by the M^{2+} ions as they move from [B] to (A) sites upon treatment of the samples at high temperatures during their preparation. This transiting between sites was forced by a tendency toward achieving a charge density balance and competing against the Pauli repulsion

Table 10

Cation distributions obtained by fitting the dependence of the magnetic moments of the $\text{Cr}_x\text{Ni}_{0.7}\text{Fe}_{2.3-x}\text{O}_4$ samples on x . Here, $V_{\text{BA}}(\text{Cr}^{2+})$, $V_{\text{BA}}(\text{Ni}^{2+})$, and $V_{\text{BA}}(\text{Fe}^{2+})$ are the heights of the potential barriers that must be jumped by the Cr^{2+} , Ni^{2+} , and Fe^{2+} ions when moving from the [B] sites to the (A) sites during the thermal treatment of the samples; N_3 is the total number of trivalent cations per formula. μ_{C} and μ_{obs} are the fitted and observed values of the sample magnetic moments at 10 K (from Xue et al. [75]).

x	0.00	0.05	0.10	0.15	0.20	0.25	0.30
N_3	0.9087	0.9078	0.9069	0.9060	0.9052	0.9044	0.9035
$V_{\text{BA}}(\text{Cr}^{2+})$ (eV)	1.4204	1.4250	1.4296	1.4342	1.4388	1.4434	1.4480
$V_{\text{BA}}(\text{Ni}^{2+})$ (eV)	1.3917	1.3962	1.4007	1.4052	1.4097	1.4142	1.4187
$V_{\text{BA}}(\text{Fe}^{2+})$ (eV)	1.3710	1.3755	1.3799	1.3843	1.3888	1.3932	1.3977
A sites							
Cr^{3+}	0.0000	0.0115	0.0230	0.0345	0.0461	0.0578	0.0695
Ni^{3+}	0.0692	0.0693	0.0695	0.0696	0.0698	0.0700	0.0701
Fe^{3+}	0.5611	0.5501	0.5390	0.5279	0.5167	0.5055	0.4942
Cr^{2+}	0.0000	0.0079	0.0157	0.0234	0.0310	0.0386	0.0461
Ni^{2+}	0.0523	0.0521	0.0518	0.0516	0.0514	0.0512	0.0510
Fe^{2+}	0.3175	0.3092	0.3011	0.2929	0.2849	0.2769	0.2690
B sites							
Cr^{2+}	0.0000	0.0258	0.0517	0.0777	0.1037	0.1297	0.1559
Ni^{2+}	0.5411	0.5413	0.5415	0.5417	0.5419	0.5421	0.5423
Fe^{2+}	1.1805	1.1559	1.1313	1.1066	1.0818	1.0570	1.0322
Cr^{3+}	0.0000	0.0048	0.0096	0.0144	0.0191	0.0238	0.0285
Ni^{3+}	0.0374	0.0373	0.0371	0.0370	0.0369	0.0367	0.0366
Fe^{3+}	0.2410	0.2348	0.2287	0.2226	0.2166	0.2106	0.2046
μ_{C} (μ_{B} /formula)	2.7339	2.6408	2.5474	2.4536	2.3596	2.2653	2.1707
μ_{exp} (μ_{B} /formula)	2.7715	2.6570	2.5185	2.3722	2.3337	2.2932	2.1909

Table 11

Cation distributions of the ferrites $M\text{Fe}_2\text{O}_4$ ($M = \text{Cr, Mn, Fe, Co, or Ni}$) obtained by fitting the magnetic moments per formula measured at 10 K. Here, T_{TH} is the calcination temperature during preparation; r is the effective ionic radius; $V(M^{2+})$ and $V(M^{3+})$ are the second and third cation ionization energies; $\mu_{\text{m}2}$ and $\mu_{\text{m}3}$ are the magnetic moments of the M^{2+} and M^{3+} cations; d_{AO} , d_{BO} , and d_{AB} are the lengths of the A–O, B–O, and A–B bonds, respectively; μ_{obs} and μ_{C} are the observed and fitted magnetic moments per formula at 10 K; f_i are the ionicities of the M cations; N_3 is the average number of trivalent cations per formula; and $V_{\text{BA}}(M^{2+})$ is the height of the equivalent potential barrier that must be jumped by the M^{2+} ions passing from the [B] to the (A) sites when the samples were treated at high temperatures. (The magnetic moment of the Fe_3O_4 sample was measured at 116 K, at which the Verwey transition occurs.)

M	Cr	Mn	Fe	Co	Ni
T_{TH} ($^{\circ}\text{C}$)	1400	1200	1450	1400	1400
$r_2(M^{2+})$ (\AA)	0.80	0.83	0.78	0.745	0.69
$V(M^{2+})$ (eV)	15.50	15.64	16.18	17.06	18.17
$V(M^{3+})$ (eV)	30.96	33.67	30.65	33.50	35.17
$\mu_{\text{m}2}(\mu_{\text{B}})$	−4	5	4	3	2
$\mu_{\text{m}3}(\mu_{\text{B}})$	−3	−4	5	4	3
d_{AO} (\AA)	1.938	2.014	1.883	1.936	1.890
d_{BO} (\AA)	2.031	2.037	2.062	2.029	2.034
d_{AB} (\AA)	3.480	3.505	3.481	3.476	3.454
$\mu_{\text{obs}}(\mu_{\text{B}}/\text{formula})$	2.044	4.505	3.927*	3.344	2.3426
μ_{C} ($\mu_{\text{B}}/\text{formula}$)	1.998	4.477	4.201	3.266	2.3603
ionicity of M ion f_i	0.8726	0.8293	0.8790	0.8314	0.8129
N_3	1.015	0.899	1.032	0.905	0.8557
$V_{\text{BA}}(M^{2+})$ (eV)	0.8617	1.129	0.815	1.2477	1.3714
$V_{\text{BA}}(\text{Fe}^{2+})$ (eV)	0.8760	1.098	0.815	1.2390	1.3608
Average ion content at (A) site					
Fe^{3+}	0.271	0.403	0.277	0.440	0.5160
Fe^{2+}	0.368	0.319	0.390	0.318	0.2975
M^{3+}	0.127	0.096	0.139	0.122	0.1047
M^{2+}	0.234	0.182	0.195	0.120	0.0818
Average ion content at [B] site					
Fe^{2+}	0.932	0.961	0.923	1.017	1.0003
Fe^{3+}	0.429	0.317	0.411	0.225	0.1862
M^{2+}	0.451	0.639	0.461	0.639	0.7647
M^{3+}	0.188	0.083	0.205	0.118	0.0488
$M^{2+}+M^{3+}$	0.639	0.722	0.666	0.757	0.8135
Ref.	[77] Shang et al., 2014	[71] Xu et al., 2015	[64] Tang et al., 2014	[77] Shang et al., 2014	[78] Lang et al., 2014

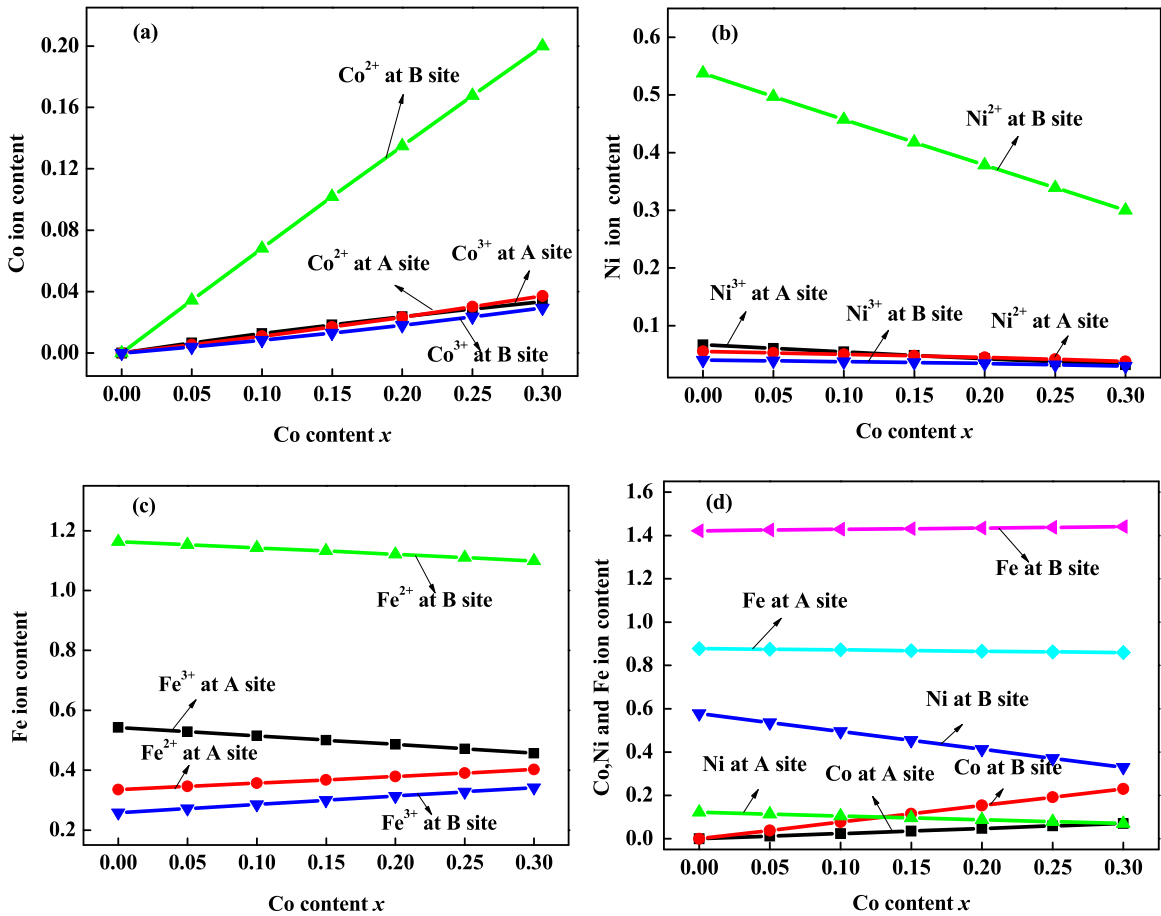


Fig. 11. (a) Co, (b) Ni, and (c) Fe cation contents and (d) the total content of Co, Ni, and Fe at the (A) and [B] sites as functions of x for $\text{Co}_x\text{Ni}_{0.7-x}\text{Fe}_{2.3}\text{O}_4$ samples (from Xue et al. [75]).

energy of the electron cloud, as discussed in Section 4.1. For all of these samples, $V_{\text{BA}}(M^{2+})$ was the only independent fitting parameter per sample used in the fitting process.

In Table 11, $V_{\text{BA}}(M^{2+})$ was determined to be between 0.81 eV and 1.37 eV for all of the samples, which are reasonable values, i.e., the energies that could be jumped by the M^{2+} ions moving from [B] to (A) sites during the sample treatment at high temperatures. It should also be noted that the percentages of M cations (including M^{2+} and M^{3+} cations) occupying [B] sites are in the range of 64%–82% for $M\text{Fe}_2\text{O}_4$ ($M = \text{Cr}, \text{Mn}, \text{Fe}, \text{Co},$ or Ni), indicating that the distributions of Cr and Mn cations are similar to those of Fe, Co, and Ni, except that the directions of the magnetic moments of the Cr^{2+} , Cr^{3+} , and Mn^{3+} cations are antiparallel to those of the magnetic moments of the other cations. In addition, the estimated concentrations of Cr cations at the (A) sites relative to the total Cr content for the $\text{Cr}_x\text{M}_{1-x}\text{Fe}_2\text{O}_4$ samples ($M = \text{Fe}, \text{Co},$ and Ni) [64,77,78] are close to the experimental results for the Cr cation distribution obtained by neutron diffraction in $\text{Cr}_x\text{NiFe}_{2-x}\text{O}_4$ ($0.0 \leq x \leq 1.0$), as reported by Ghatage et al. [21] and shown in Fig. 15.

4.3. Important experimental evidence for the IEO model from Ti-doped spinel ferrites

It has been assumed in many reports, according to traditional models, that Ti cations in ferrites appear in the form Ti^{4+} . However, as was the case for the Mn- and Cr-doped ferrites, there are numerous conflicting reports regarding the distributions of Ti ions in spinel ferrites that follow from this assumption. Kale et al. [81] prepared $\text{Ni}_{1+x}\text{Ti}_x\text{Fe}_{2-2x}\text{O}_4$ ($0 \leq x \leq 0.7$) polycrystalline samples and found that both the lattice constants and saturation magnetizations of the samples decreased with increasing Ti doping. They concluded that the percentage of Ti^{4+} cations occupying (A) sites increased from 5% (when $x = 0.1$) to 71% (when $x = 0.7$). Srivastava et al. [82] prepared $\text{Ni}_{0.7+x}\text{Zn}_{0.3}\text{Ti}_x\text{Fe}_{2-2x}\text{O}_4$ ($0 \leq x \leq 0.08$) ferrite samples and concluded that all of the Ti^{4+} cations entered the lattice at the [B] sites, resulting in a canted spin structure, based on Mössbauer spectra analysis. Kobayashi et al. [83] prepared $\text{Zn}_{0.6-x}\text{Ni}_{0.4+x}\text{Ti}_x\text{Fe}_{2-x}\text{O}_4$ ($x = 0.0, 0.2,$ or 0.3) films, claiming that most of the Ti ions in the samples were Ti^{4+} cations. Dwivedi et al. [84] prepared $\text{CoTi}_{2x}\text{Fe}_{2-2x}\text{O}_4$ ($x = 0.0, 0.05,$ or 0.1) and

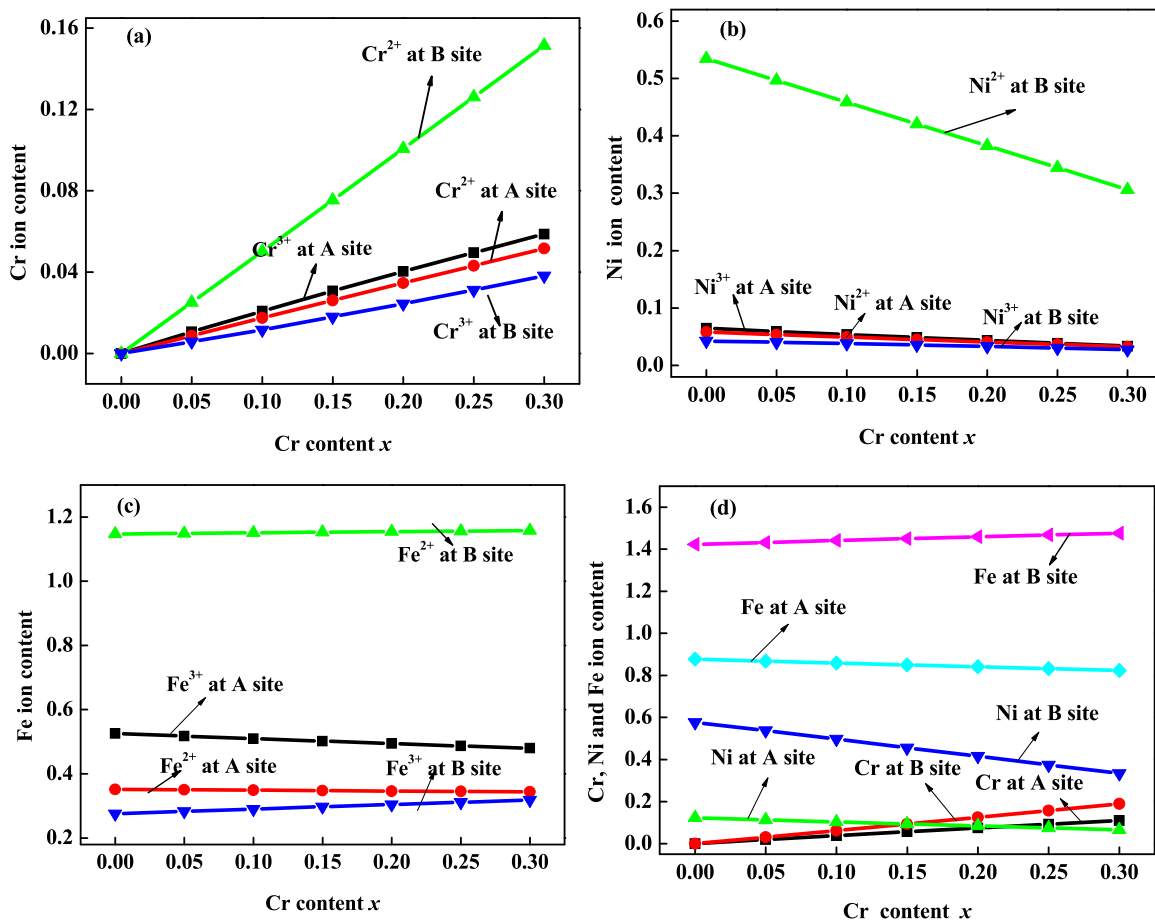


Fig. 12. (a) Cr, (b) Ni, and (c) Fe cation contents and (d) the total content of Cr, Ni, and Fe at the (A) and [B] sites as functions of x for $\text{Cr}_x\text{Ni}_{0.7-x}\text{Fe}_{2.3}\text{O}_4$ samples (from Xue et al. [75]).

concluded that Ti cations, being tetravalent, entered at the [B] sites. Srinivasa Rao et al. [85] prepared Ti-substituted Co ferrite with the general formula $\text{CoFe}_{2-x}\text{Ti}_x\text{O}_4$ ($0 \leq x \leq 0.3$) and found that the magnetization of the samples decreased with increasing x . In addition, they considered that all of the Ti cations, being tetravalent, entered at the [B] sites. In contrast, Jin et al. [86] prepared $\text{Fe}_{3-x}\text{Ti}_x\text{O}_4$ ($0 \leq x \leq 0.09$) films on (001)-oriented MgO substrates and determined that all of the Ti^{4+} cations occupied the (A) sites.

To explain why there are such large discrepancies among the reported Ti cation distributions, Xu et al. [87–89] investigated Ti-doped spinel ferrite powder samples using the IEO model. They prepared three series of Ti-doped spinel ferrite powder samples with nominal compositions of $\text{Ni}_{0.68-0.8x}\text{Ti}_x\text{Fe}_{2.32-0.2x}\text{O}_4$ ($0 \leq x \leq 0.312$), $\text{Ni}_{0.68+0.26x}\text{Ti}_x\text{Fe}_{2.32-1.26x}\text{O}_4$ ($0 \leq x \leq 0.4$), and $\text{Ti}_x\text{Ni}_{1-x}\text{Fe}_2\text{O}_4$ ($0 \leq x \leq 0.4$) using a solid phase reaction method and investigated the crystal structure, magnetic properties, and cation distributions for each sample. A transition temperature, T_N , was found when the Ti doping level x was greater than 0.15; below T_N , the magnetization of the samples abruptly decreased with decreasing measurement temperature T rather than rising or remaining nearly constant, as in samples with less doping. Fig. 16(a)–(c) show the dependences of the specific magnetizations, σ , of the three series of samples on the temperature, T , measured from 300 K to 10 K, under an applied magnetic field of 50 mT. It was also found that T_N increased with increasing x . These phenomena indicate that Ti doping can induce an additional antiferromagnetic structure in the traditional spinel phase of ferrites. This result is unexpected because Ti is usually thought to appear as quadrivalent ions with zero net magnetic moment.

Using an approach similar to that in Section 4.1, the cation distribution was obtained by fitting the dependence of μ_{obs} on x for $\text{Ni}_{0.68-0.8x}\text{Ti}_x\text{Fe}_{2.32-0.2x}\text{O}_4$ ($0 \leq x \leq 0.312$) [88] and $\text{Ti}_x\text{Ni}_{1-x}\text{Fe}_2\text{O}_4$ ($0 \leq x \leq 0.4$) [89]. Fig. 16(d) shows μ_{obs} (points) and μ_c (curves) for the samples at 10 K. In the fitting process, we assumed that the magnetic moment directions of the Ti^{3+} ($3d^1$) and Ti^{2+} ($3d^2$) cations were antiparallel to those of the Fe and Ni cations at both the [B] and (A) sites. The results indicate that Ti^{2+} cations at the [B] sites constituted about 80% of the total Ti content for all of the samples. Therefore, the Ti cation distribution is similar to that of Ni cations, except that the magnetic moments of the Ti cations are antiparallel to those of Ni and Fe cations.

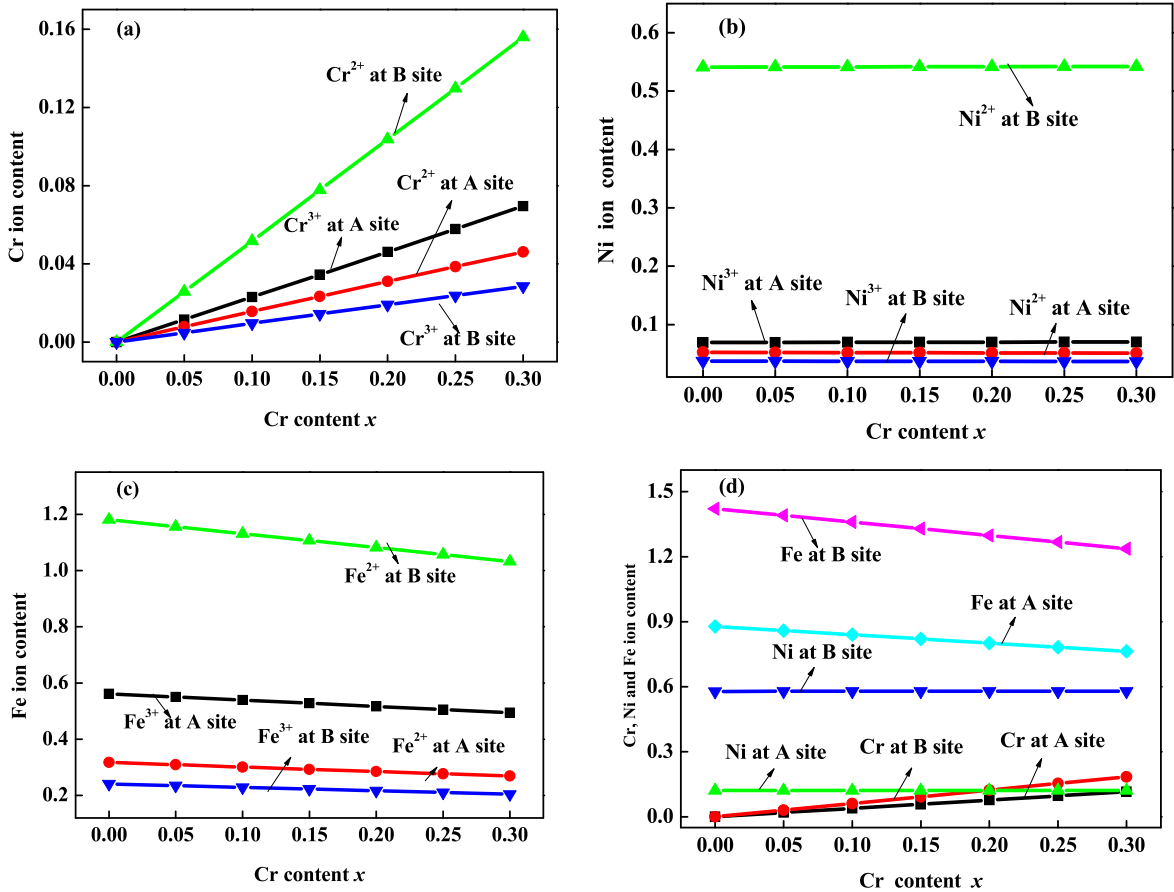


Fig. 13. (a) Cr, (b) Ni, and (c) Fe cation contents and (d) the total content of Cr, Ni, and Fe at the (A) and [B] sites as functions of x for $\text{Cr}_x\text{Ni}_{0.7}\text{Fe}_{2.3-x}\text{O}_4$ samples (from Xue et al. [75]).

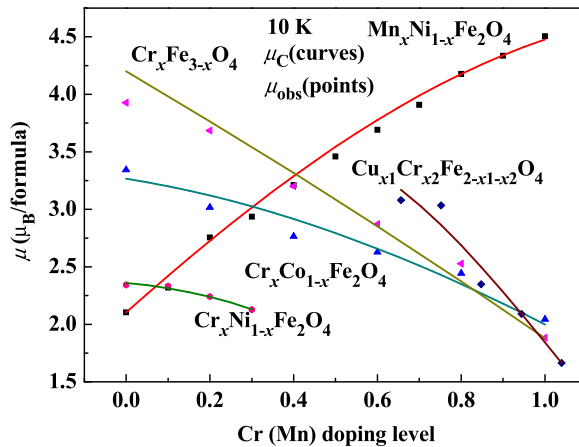


Fig. 14. Dependence of the observed, μ_{obs} (points), and fitted, μ_{C} (curves), magnetic moments on the doping level, x , for the ferrite samples $\text{Cr}_x\text{Fe}_{3-x}\text{O}_4$ (Tang et al. [64]), $\text{Cr}_x\text{Co}_{1-x}\text{Fe}_2\text{O}_4$ (Shang et al. [77]), $\text{Cr}_x\text{Ni}_{1-x}\text{Fe}_2\text{O}_4$ (Lang et al. [78]), $\text{Cu}_{x_1}\text{Cr}_{x_2}\text{Fe}_{2-x_1-x_2}\text{O}_4$ ($0.0 \leq x \leq 0.4$, $x_1 = 0.71x$, $x_2 = 1.04 - 0.96x$) (Zhang et al. [79]), and $\text{Mn}_x\text{Ni}_{1-x}\text{Fe}_2\text{O}_4$ (Xu et al. [71]).

The listed investigations therefore provide important experimental evidence for the IEO model. Specifically, they demonstrate that: (i) Ti ions in spinel ferrites have magnetic moments, which is contrary to the traditional assumption of Ti^{4+} cations, which have zero magnetic moments, and therefore, the traditional viewpoint that Ti cations are quadrivalent

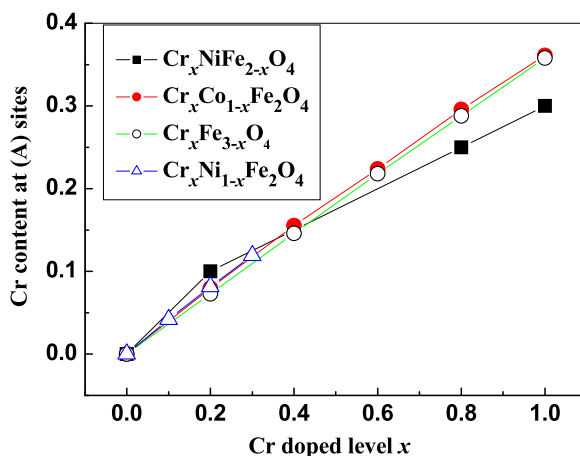


Fig. 15. Dependence of the estimated Cr content at the (A) sites on x for the ferrite samples $\text{Cr}_x\text{Fe}_{3-x}\text{O}_4$ (Tang et al. [64]), $\text{Cr}_x\text{Co}_{1-x}\text{Fe}_2\text{O}_4$ (Shang et al. [77]), $\text{Cr}_x\text{Ni}_{1-x}\text{Fe}_2\text{O}_4$ (Lang et al. [78]), and $\text{Cr}_x\text{NiFe}_{2-x}\text{O}_4$ (Ghatage et al. [21]).

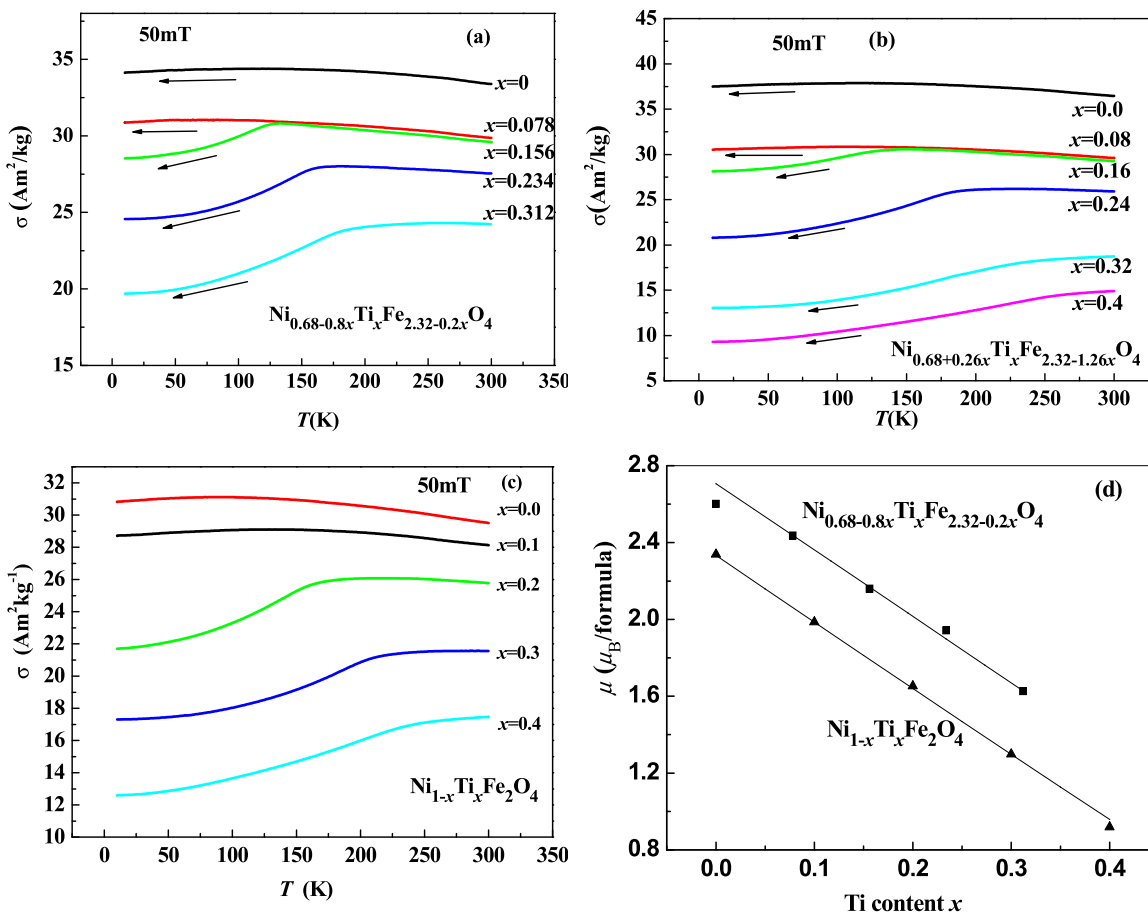


Fig. 16. Dependences on the temperature, T , of the specific magnetization, σ , of the samples $\text{Ni}_{0.68-0.8x}\text{Ti}_x\text{Fe}_{2.32-0.2x}\text{O}_4$, (b) $\text{Ni}_{0.68+0.26x}\text{Ti}_x\text{Fe}_{2.32-1.26x}\text{O}_4$, and (c) $\text{Ti}_x\text{Ni}_{1-x}\text{Fe}_2\text{O}_4$, measured from 300 K to 10 K, under an applied magnetic field of 50 mT; (d) dependences on Ti-doping level, x , of observed and fitted magnetic moment values, μ_{obs} (points) and μ_{C} (curves), for the samples at 10 K. From Xu et al. [87–89].

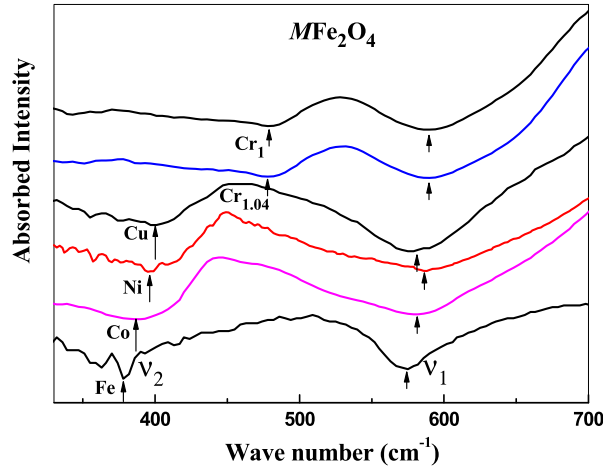


Fig. 17. Infrared spectra of the cubic spinel ferrites $M\text{Fe}_2\text{O}_4$ ($M = \text{Fe}, \text{Co}, \text{Ni}, \text{or Cr}$) and $\text{Cu}_{0.85}\text{Fe}_{2.15}\text{O}_4$, measured at room temperature (from Tang et al. [90]).

Table 12

Observed and estimated values of the infrared absorption peak position (Tang et al. [90]), $\nu_{2\text{exp}}$ and $\nu_{2\text{cal}}$, respectively, corresponding to lattice thermal vibrations of the octahedral sites in $M\text{Fe}_2\text{O}_4$ ($M = \text{Cr}, \text{Fe}, \text{Co}, \text{or Ni}$) and $\text{Cu}_{0.85}\text{Fe}_{2.15}\text{O}_4$ samples. μ_{m2} is the magnetic moment of the M^{2+} cations, $|V_{\text{AIO}}|$ is the absolute value of the average valence of O, and k_{exp} and k_{cal} are the observed and calculated values, respectively, of the force constant.

Samples	$\nu_{2\text{exp}}$ (cm^{-1})	$\nu_{2\text{cal}}$ (cm^{-1})	μ_{m2} (μ_B)	$ V_{\text{AIO}} $	k_{exp} (N m^{-1})	k_{cal} (N m^{-1})	Reference
Fe_3O_4	378	372	4	1.758	105.4	101.9	[90] Tang et al. (2015)
CoFe_2O_4	387	387	3	1.727	111.2	111.3	[90] Tang et al. (2015)
NiFe_2O_4	396	398	2	1.714	116.4	117.3	[90] Tang et al. (2015)
$\text{Cu}_{0.85}\text{Fe}_{2.15}\text{O}_4$	400	403	1	1.713	119.8	121.6	[90] Tang et al. (2015)
CrFe_2O_4 (Cr_1)	479	479	-4	1.754	167.3	167.4	[90] Tang et al. (2015)
$\text{Cr}_{1.04}\text{Fe}_{1.96}\text{O}_4$ ($\text{Cr}_{1.04}$)	478		-4				[90] Tang et al. (2015)
CoFe_2O_4	395		3				[91] Ati et al. (2013)
NiFe_2O_4	403		2				[91] Ati et al. (2013)
NiFe_2O_4	404		2				[92] Gabal et al. (2011)
CuFe_2O_4	402		1				[92] Gabal et al. (2011)
$\text{Co}_{0.8}\text{Ni}_{0.2}\text{Fe}_2\text{O}_4$	382		3				[93] Wahba et al. (2014)

is not tenable; (ii) the actual valence of an oxide is distinctly less than its ideal value and the ionicity must consequently be accounted for when investigating the magnetic ordering of an oxide; and (iii) the magnetic moment directions of cations with $n_d \leq 4$ are antiparallel to those of cations with $n_d \geq 5$, whether at the [B] or (A) sites of spinel ferrites.

4.4. Experimental evidence for the IEO model from the infrared spectra of $M\text{Fe}_2\text{O}_4$ samples

The infrared spectra of samples of (A)[B]₂O₄ spinel ferrites $M\text{Fe}_2\text{O}_4$ ($M = \text{Fe}, \text{Co}, \text{Ni}, \text{Cu}, \text{or Cr}$) were investigated by Tang et al. [90]. It was found that the wave number ν_2 corresponding to the thermal vibration of B–O–B bonds increased with decreasing magnetic moment, μ_{m2} , of the M^{2+} cations, as calculated with the assumption that the magnetic moment of the Cr^{2+} cation was antiparallel to those of the other cations.

Fig. 17 shows the infrared spectra of the single-phase, cubic spinel ferrites $M\text{Fe}_2\text{O}_4$ ($M = \text{Fe}, \text{Co}, \text{Ni}, \text{or Cr}$) and $\text{Cu}_{0.85}\text{Fe}_{2.15}\text{O}_4$ measured at room temperature. In Fig. 17, the arrows indicate the two absorption bands for each sample. The higher-wave-number band is labeled by ν_1 at its peak and corresponds to vibrations of the tetrahedral sites (A–O–A bonds). The lower-wave-number band is labeled by ν_2 and corresponds to vibrations of the octahedral sites (B–O–B bonds). These spectra are similar to those reported by Ati et al. [91], Gabal et al. [92], Wahba et al. [93], and Pervaiz et al. [94]. For the $M\text{Fe}_2\text{O}_4$ samples, it can be seen that ν_2 is shifted by 22 cm^{-1} toward higher wave numbers, i.e., from 378 cm^{-1} ($M = \text{Fe}$) to 400 cm^{-1} ($M = \text{Cu}$), while ν_2 is shifted by 101 cm^{-1} toward higher wave numbers, from 378 cm^{-1} ($M = \text{Fe}$) to 479 cm^{-1} ($M = \text{Cr}$). No convincing explanation based on traditional models has yet been found for this difference in wave number between Cr-doped samples and other ferrites. However, it can be explained using the IEO model.

Table 11 demonstrates that the number of M^{2+} cations occupying the (A) sites is far less than that of those occupying the [B] sites. Therefore, in what follows, we discuss only the dependence of ν_2 on M^{2+} , which corresponds to the vibration of the [B] sublattice.

Fig. 18 and Table 12 show the dependence of ν_2 on μ_{m2} . Interestingly, Fig. 18 reveals that ν_2 increases as μ_{m2} of the divalent M^{2+} cations decreases. Here, the magnetic moment of the Cr^{2+} cation is $-4\mu_B$ and is thus antiparallel to those of

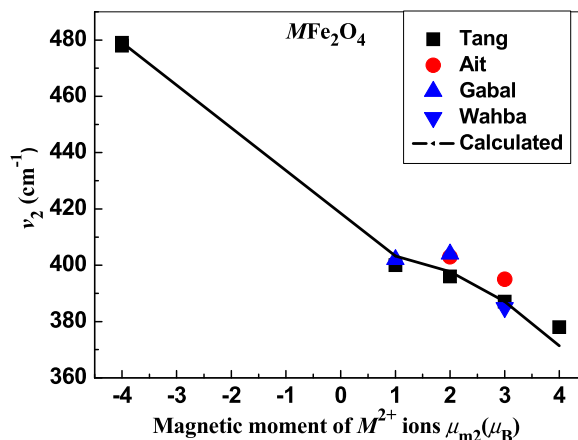


Fig. 18. Dependence of the wave number, ν_2 , of the infrared peak corresponding to vibrations of the octahedral sites (B–O–B bonds) on the magnetic moment, μ_{m2} , of the divalent M cations in the spinel ferrites $M\text{Fe}_2\text{O}_4$ ($M = \text{Fe, Co, Ni, or Cr}$) and $\text{Cu}_{0.85}\text{Fe}_{2.15}\text{O}_4$ (from Tang et al. [90]). Here, the points are the observed results, including the results reported by Aiti et al. [91], Gabal et al. [92], Wahba et al. [93], the curve is an estimated result using the theory of crystal lattice vibrations in a one-dimensional diatomic lattice [95].

the other cations according to the IEO model. The ν_2 data for the spinel ferrites reported by other groups are also shown in Fig. 18 and Table 12, including data for CoFe_2O_4 and NiFe_2O_4 reported by Aiti et al. [91], NiFe_2O_4 and CuFe_2O_4 reported by Gabal et al. [92], and $\text{Co}_{0.8}\text{Ni}_{0.2}\text{Fe}_2\text{O}_4$ reported by Wahba et al. [93]. In Fig. 18, the displayed curve was estimated using the theory of crystal lattice vibrations in a one-dimensional diatomic lattice [90,95].

It should be noted from Section 3 that the magnetic moments of the Cr cations were assumed to be antiparallel to those of the other cations in the calculations. The consistency of the calculation results shown in Fig. 18 indicates that this assumption in the IEO model is highly reasonable.

4.5. Canted magnetic structures and cation distributions in the spinel ferrites $MN_x\text{Fe}_{2-x}\text{O}_4$

In Sections 4.1–4.4, the cation magnetic moments in spinel ferrites $M\text{Fe}_2\text{O}_4$ ($M = \text{Ti, Cr, Mn, Fe, Co, Ni, Cu}$) were considered to be parallel or antiparallel to each other, and the Fe content of each sample was not less than 2.0. However, when the Fe content is less than 2.0, $MN_x\text{Fe}_{2-x}\text{O}_4$ will have a canted magnetic structure [96–98]. The reason may be understood using the IEO model: there are many Fe^{3+} cations at the (A) and [B] sites, as shown in Table 11. The itinerant electrons pass through the highest energy level of the intermediary cations $\text{Fe}^{3+}(3d^5)$, as shown in Fig. 19(a)–(e), when the Fe content is not less than 2.0, and they will expend only a small amount of energy of the system. Otherwise, the itinerant electrons will expend more energy, and cause the total magnetic ordering energy to decrease, such as in Fig. 19 (f), an itinerant electron with spin down passes through the second-highest energy level of the intermediary cations $\text{Co}^{3+}(3d^6)$. In Fig. 19, An arrow drawn on a $3d$ energy level represents an electron with a specific spin direction. ∇ represents a $2p$ hole, which in the illustrated case represents the absence of a spin-down electron.

Liu et al. [96] prepared $\text{Co}_{1+x}\text{Fe}_{2-x}\text{O}_4$ samples ($0.0 \leq x \leq 2.0$) via chemical co-precipitation. The samples exhibited (A)[B]₂O₄ single-phase, cubic spinel structures. Magnetic measurements indicated that the specific saturation magnetization σ_s of the samples at 10 K decreased from a maximum of $75.2 \text{ A m}^2 \text{ kg}^{-1}$ ($x = 0.0$) to a minimum of $0.0 \text{ A m}^2 \text{ kg}^{-1}$ ($x = 2.0$), with a local minimum at $x = 1.4$, as shown in Fig. 20. The dependence of σ_s on x at 10 K is very similar to that measured at 77 K by Takahashi et al. [99], as shown in the inset of Fig. 20.

Because the magnetic moments of the samples decreased with increasing Co concentration x ($0.0 \leq x \leq 1.4$), it was assumed that the average angle between neighboring cation magnetic moments in the samples increased with increasing Co^{2+} concentration, C_{2A} or C_{2B} , at the (A) or [B] sites, respectively. This assumption can be accounted for using the magnetic moment attenuation factors

$$[1 - c_1(C_{2A} - C_{2A0})^{1.2}] \text{ for the (A) sublattice} \quad (4.20)$$

and

$$[1 - c_1(C_{2B} - C_{2B0})^{1.2}] \text{ for the [B] sublattice.} \quad (4.21)$$

In these two factors, c_1 is a constant, and the content factors C_{2A0} and C_{2B0} are equal to C_{2A} and C_{2B} , respectively, when $x = 0$. C_{2A0} and C_{2B0} can be deduced from the attenuation factors resulting from the fact that the cation moments are parallel to each other at the (A) and [B] sites, respectively, in CoFe_2O_4 [77].

By applying the cation distribution estimation method described in Section 4.1 as well as these attenuation factors, Liu et al. [96] estimated the cation distributions of $\text{Co}_{1+x}\text{Fe}_{2-x}\text{O}_4$ samples ($0.0 \leq x \leq 1.4$), as shown in Table 13 and Fig. 21. In

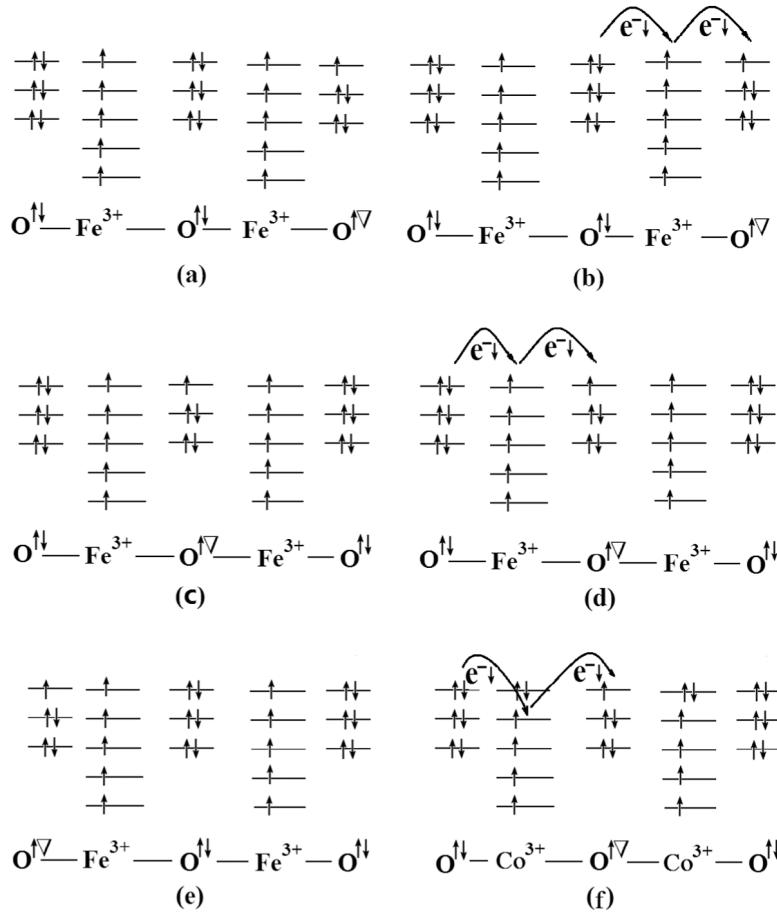


Fig. 19. (a)–(e) An itinerant electron with spin down passes through the highest energy level of the intermediary cations Fe^{3+} ($3d^5$), (f) an itinerant electron with spin down passes through the second-highest energy level of the intermediary cations Co^{3+} ($3d^6$). An arrow drawn on a $3d$ energy level represents an electron with a specific spin direction. ∇ represents a $2p$ hole, which in the illustrated case represents the absence of a spin-down electron.

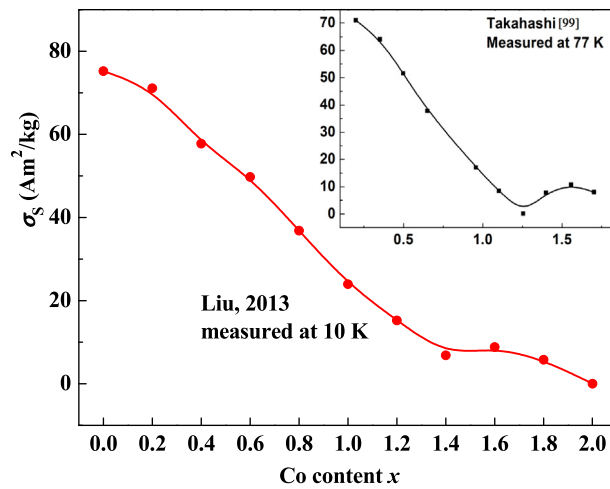


Fig. 20. Specific saturation magnetization σ_s of the $Co_{1+x}Fe_{2-x}O_4$ samples at 10 K versus x (from Liu et al. [96]). The inset shows the results at 77 K reported by Takahashi et al. [99]).

Table 13

Fitted results for the dependences of the cation distributions and magnetic moments of $\text{Co}_{1+x}\text{Fe}_{2-x}\text{O}_4$ samples on x (Liu et al. [96]). Here, μ_{AT} , μ_{BT} , and μ_{C} are the fitted magnetic moments per formula of the (A) sublattice, [B] sublattice, and full samples, respectively; $V_{\text{BA}}(\text{Fe}^{2+})$ and $V_{\text{BA}}(\text{Co}^{2+})$ are the heights of the potential barriers that must be jumped by the Fe^{2+} and Co^{2+} ions from [B] to (A) sites when the samples were treated at high temperature, respectively; and N_3 is the number of trivalent cations per formula of sample.

x		0	0.2	0.4	0.6	0.8	1.0	1.2	1.4
	$V_{\text{BA}}(\text{Fe}^{2+})$ (eV)	1.095	1.126	1.157	1.188	1.219	1.250	1.281	1.312
	$V_{\text{BA}}(\text{Co}^{2+})$ (eV)	1.102	1.133	1.164	1.196	1.227	1.258	1.289	1.320
	$\mu_{\text{AT}}(\mu_{\text{B}}/\text{formula})$	4.303	4.233	4.154	4.068	3.976	3.879	3.775	3.666
	$\mu_{\text{BT}}(\mu_{\text{B}}/\text{formula})$	7.602	7.150	6.635	6.105	5.572	5.043	4.524	4.017
	$\mu_{\text{C}}(\mu_{\text{B}}/\text{formula})$	3.299	2.917	2.482	2.037	1.596	1.165	0.749	0.352
	N_3	0.905	0.880	0.854	0.829	0.804	0.778	0.753	0.727
(A)site	Fe^{3+}	0.428	0.404	0.376	0.345	0.311	0.272	0.228	0.180
	Co^{3+}	0.122	0.154	0.189	0.227	0.269	0.314	0.363	0.416
	Fe^{2+}	0.325	0.292	0.260	0.228	0.196	0.164	0.131	0.099
	Co^{2+}	0.128	0.150	0.175	0.200	0.225	0.251	0.278	0.305
[B]site	Fe^{2+}	0.978	0.880	0.780	0.681	0.582	0.483	0.385	0.287
	Co^{2+}	0.667	0.799	0.931	1.062	1.193	1.324	1.453	1.581
	Fe^{3+}	0.269	0.224	0.183	0.146	0.112	0.082	0.056	0.035
	Co^{3+}	0.086	0.097	0.105	0.111	0.113	0.111	0.106	0.097

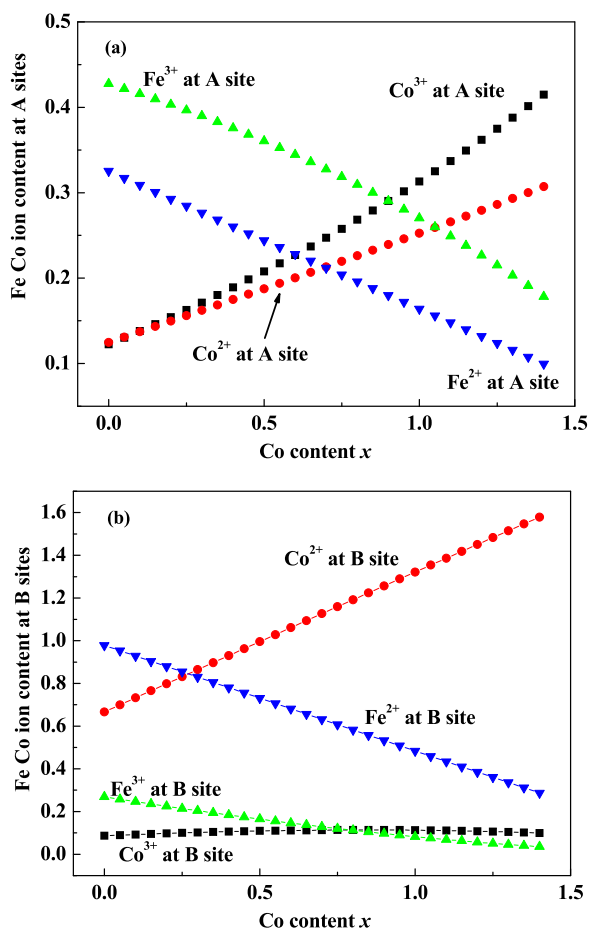


Fig. 21. Estimated cation distributions at the (a) (A) and (b) [B] sites for the $\text{Co}_{1+x}\text{Fe}_{2-x}\text{O}_4$ samples, as functions of x (from Liu et al. [96]).

the fitting process, c_1 was determined to be 0.420. The fitted magnetic moments of the (A) and [B] sublattices and the full samples per formula, μ_{AT} , μ_{BT} , and μ_{C} , are presented as functions of x at 10 K in Fig. 22. It can be seen that μ_{C} (curve) is very close to μ_{obs} (points) for these samples.

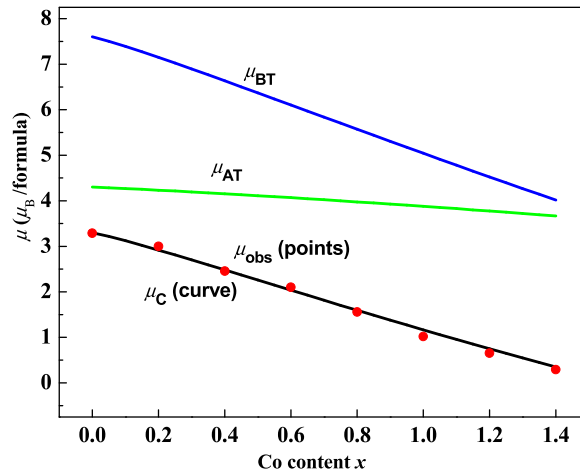


Fig. 22. Fitted magnetic moments per formula of the (A) and [B] sublattices and the full samples, μ_{AT} , μ_{BT} , and μ_C (curves), and observed magnetic moment μ_{obs} (points) at 10 K as functions of x for the $\text{Co}_{1+x}\text{Fe}_{2-x}\text{O}_4$ samples (from Liu et al. [96]).

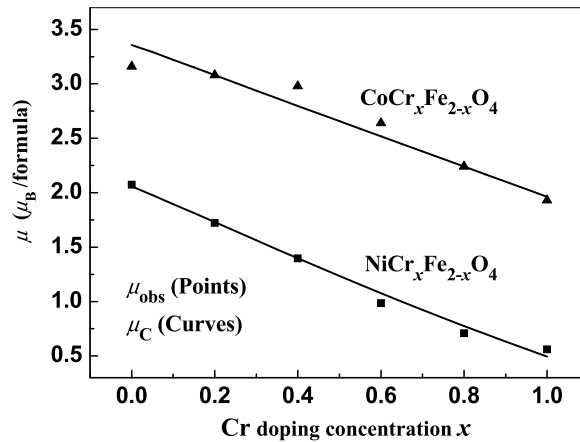


Fig. 23. Fitted, μ_C (curve) and observed μ_{obs} (points), magnetic moments, as functions of x for the $\text{NiCr}_x\text{Fe}_{2-x}\text{O}_4$ (Bian [97]) and $\text{CoCr}_x\text{Fe}_{2-x}\text{O}_4$ (Shang [98]) samples.

(A)[B]₂O₄ spinel ferrite samples with nominal compositions of $\text{NiCr}_x\text{Fe}_{2-x}\text{O}_4$ ($0.0 \leq x \leq 1.0$) and $\text{CoCr}_x\text{Fe}_{2-x}\text{O}_4$ ($0.0 \leq x \leq 1.0$) were prepared by Bian [97] and Shang [98]. Their XRD patterns indicated that the samples exhibited single-phase cubic spinel structures. Magnetic measurements showed that the magnetic moments of the samples at 10 K decreased with increasing x . These results are similar to those mentioned above for $\text{Co}_{1+x}\text{Fe}_{2-x}\text{O}_4$. Using the IEO model, the cation distributions in all of the samples were estimated using the magnetic moments of the samples at 10 K. As in the previous example, μ_C is very close to μ_{obs} , as shown in Fig. 23.

4.6. Canted magnetic structures and cation distributions in $M_x\text{Mn}_{1-x}\text{Fe}_2\text{O}_4$ ($M = \text{Zn}, \text{Mg}, \text{or Al}$)

The effects of Zn (or Mg and Al) doping on the crystal structures and physical properties of spinel ferrites have been reported in many studies, but as for the cases of Mn-, Cr-, and Ti-doped spinel ferrites, the resulting ion distributions have been disputed in a number of studies. Angadi et al. [100] prepared a series of $\text{Mn}_{1-x}\text{Zn}_x\text{Fe}_2\text{O}_4$ ($0.0 \leq x \leq 1.0$) nanocrystalline materials and claimed that the Fe^{3+} ions migrated from the [B] sites to the (A) sites and that the Mn^{2+} concentration decreased in both the (A) and [B] sites as x increased. Mathuret et al. [101] prepared a series of $\text{Zn}_x\text{Mn}_{1-x}\text{Fe}_2\text{O}_4$ ferrites, with $x = 0.1, 0.3, 0.5, 0.7,$ and 0.9 , and concluded that the Zn^{2+} ions tended to go to the (A) sites at low concentrations but also went to the [B] sites when $x \geq 0.3$. Singh [102] prepared $\text{Mg}_x\text{Mn}_{1-x}\text{Fe}_2\text{O}_4$ ($0.0 \leq x \leq 0.8$) ferrites and thought that the Mg^{2+} ions tended to go to the (A) sites but also went to the [B] sites when $x \geq 0.4$. Antic et al. [103] synthesized MgFe_2O_4 nanoparticles and investigated the cation distribution using a Rietveld refinement, concluding that the cation distribution was given by $(\text{Mg}_{1-\delta}\text{Fe}_\delta)[\text{Mg}_\delta\text{Fe}_{2-\delta}]\text{O}_4$ with $\delta = 0.69$. Khot et al. [104] prepared nanocrystalline samples of $\text{Mn}_x\text{Mg}_{1-x}\text{Fe}_2\text{O}_4$ ($x = 0.0, 0.2, 0.4, 0.6, 0.8,$ or 1.0), concluding that Mg^{2+} ions entered only the [B] sites when $(1-x) \leq 0.6$. To study the effects of Al doping,

Pandit et al. [105] prepared polycrystalline samples of $\text{CoAl}_x\text{Fe}_{2-x}\text{O}_4$ with $x = 0.0, 0.2, 0.4, 0.6,$ and 0.8 and concluded that the ratio of the number of Al cations at the (A) sites to that at the [B] sites was approximately 3/7 based on XRD data analysis.

To resolve these disparities, Han et al. [106,107] investigated the cation distributions of Zn-doped spinel ferrites using the quantum-mechanical potential barrier model [61]. Ding et al. [108] prepared $M_x\text{Mn}_{1-x}\text{Fe}_2\text{O}_4$ ($M = \text{Zn, Mg, or Al}$) spinel ferrite samples and determined μ_{obs} of the samples at 10 K. They obtained the cation distributions of the samples by fitting the curves of μ_{obs} versus x using the method described in Section 4.1. The only difference in this case was that in Eqs. (4.2) and (4.3), the following barrier height was substituted in place of the original one:

$$V_{\text{BA}}(\text{Fe}^{2+}) = \frac{V_{\text{BA}}(\text{Mn}^{2+})V(\text{Fe}^{3+})r(\text{Fe}^{2+})}{V(\text{Mn}^{3+})r(\text{Mn}^{2+})}, \quad (4.22)$$

which gives the relation between $V_{\text{BA}}(\text{Fe}^{2+})$ and $V_{\text{BA}}(\text{Mn}^{2+})$. $V_{\text{BA}}(M^{2+})$ for the non-magnetic cations $M = \text{Zn, Mg, or Al}$ were obtained by fitting the curves of μ_{obs} versus x . The fitted curves are very close to the experimental results for the three series of samples, as shown in Fig. 24. Here, μ_{C} (curve) describes the calculated magnetic moments of the samples, while μ_{AT} and μ_{BT} are the magnetic moments of the (A) and [B] sublattices, respectively. In the fitting process, it was assumed that the average angle between the magnetic moments of the cations increased with increasing x , and the results of this analysis are presented in Fig. 25. The cation distributions obtained by the fitting process are shown in Figs. 26–28 and can be described as follows.

(i) For all three series of samples, the portion of Fe (Fe^{2+} and Fe^{3+}) cations occupying [B] sites lies between 62% and 74% of the total Fe content, and the number of Mn^{2+} cations occupying [B] sites lies between 55% and 65% of the total Mn content. Consequently, the magnetic moments of the samples have the same direction as that of the [B] sublattice.

(ii) For $\text{Mg}_x\text{Mn}_{1-x}\text{Fe}_2\text{O}_4$ ($0.0 \leq x \leq 1.0$) and $\text{Al}_x\text{Mn}_{1-x}\text{Fe}_2\text{O}_4$ ($0.0 \leq x \leq 0.5$), it can be seen from Figs. 27(d) and 28(d) that the numbers of Mg^{2+} and Al (including Al^{2+} and Al^{3+}) cations increase approximately linearly at both the (A) and [B] sites, with the content at the [B] sites being greater than that at the (A) sites for every doping level. This feature may be the underlying reason that the magnetic moments of the [B] sublattices decrease more rapidly than those of the (A) sublattices (see Fig. 24(b) and 24(c)), while the total magnetic moments decrease approximate linearly with increasing x . It is also worth recalling that the net magnetic moments of Mg^{2+} , Al^{2+} , and Al^{3+} cations are all zero.

(iii) For the cation distributions of the Zn-doped samples, shown in Fig. 26, one can see that when $x < 0.4$, the Zn^{2+} content at the (A) sites increases rapidly and the Fe^{2+} , Fe^{3+} , and Mn^{2+} contents at the (A) sites decrease gradually with increasing x , causing the magnetic moment of the (A) sublattice to decrease rapidly and the total magnetic moment of the samples to increase. In contrast, when $x > 0.4$, the Zn^{2+} content at the [B] sites increases rapidly and the Mn^{2+} content at the [B] sites decreases gradually with increasing x , causing both the magnetic moment of the [B] sublattice and the total magnetic moment of the samples to decrease rapidly. These cation distributions can be understood based on the lattice energy as follows: (a) when $x < 0.4$, the Zn^{2+} content at the (A) sites increases rapidly, maybe because doping of Zn cations without magnetic moments can decrease the magnetic repulsion energy in the (A) sublattice; and (b) the radius of Zn^{2+} (0.074 nm) is larger than those of Fe^{3+} (0.0645 nm) and Mn^{3+} (0.0645 nm) [76]. The substitution of Zn^{2+} cations for Fe^{3+} and Mn^{3+} cations causes the Pauli repulsion energy in the (A) sublattice to increase, and thus, when $x > 0.4$, the (A) sublattice can no longer gain more Zn^{2+} cations, and the Zn^{2+} content at the [B] sites increases rapidly.

5. Applications of the IEO model to ABO_3 perovskite manganites

As mentioned in Section 1.2.2, no satisfactory explanation regarding the dependence of the magnetic moment of the manganites $\text{R}_{1-x}\text{T}_x\text{MnO}_3$ on x has been found. Based on the experimental results for O 2p holes (in the outer orbits of O^{1-} anions) of the CMR manganites [66–70], Tang et al. provided a reasonable explanation for the magnetic structures of ABO_3 perovskite manganites by applying the IEO model to these materials, while also fitting the doping level dependence of the magnetic moments for several series of perovskite manganites.

5.1. Magnetic structures of the perovskite manganites $\text{La}_{1-x}\text{Sr}_x\text{MnO}_3$ ($0 \leq x \leq 0.4$)

Following the above investigations of (A)[B]₂O₄ spinel ferrites, Wu et al. [109,110] chose to study the doping level dependences of the magnetic moments of the $\text{La}_{1-x}\text{Sr}_x\text{MnO}_3$ perovskite manganites using the IEO model. Powder samples with the composition $\text{La}_{1-x}\text{Sr}_x\text{MnO}_3$ ($0 \leq x \leq 0.4$) were prepared via the sol-gel method [111–115], and XRD patterns indicated that all of the samples had only a single phase, ABO_3 perovskite structures with the space group $\text{R}\bar{3}\text{c}$. The volume-averaged diameter of the crystallites in the samples was estimated based on the Scherrer equation and was greater than ~ 100 nm for all of the samples. The impact of crystallite surface effects was expected to be very weak. Rietveld fitting of the XRD patterns of the samples was also conducted, and the fitted results for the lattice parameters a and c ; the crystal cell volume v ; the A–O and B–O (Mn–O) bond lengths d_{AO} and d_{BO} , respectively; the B–O–B (Mn–O–Mn) bond angle θ ; and the fitting parameters, i.e., the profile factor R_p , weighted profile factor R_{wp} , and goodness of fit indicator s , are all presented in Table 14.

Fig. 29 shows the dependences of a , c , v , d_{BO} , and θ on x . As x increases, the following observations can be made: (i) there is a characteristic doping level, $x_1 = 0.15$, for d_{BO} , such that when $x < 0.15$, d_{BO} experiences little change in magnitude, while d_{BO} decreases with increasing x when $x > 0.15$; (ii) there is another characteristic doping level, $x_2 = 0.20$, for a and v , such

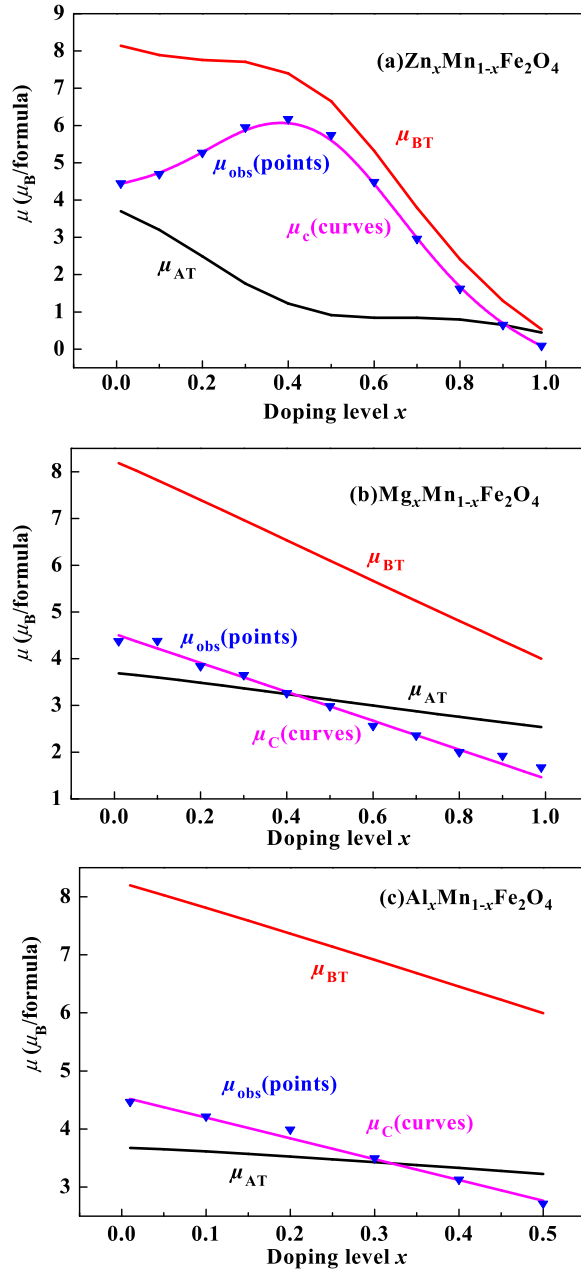


Fig. 24. Fitted magnetic moments per formula of the (A) and [B] sublattices and the full samples, μ_{AT} , μ_{BT} , and μ_C (curves), and observed magnetic moment μ_{obs} (points) at 10 K, as functions of the doping level x of (a) $Zn_x Mn_{1-x} Fe_2 O_4$, (b) $Mg_x Mn_{1-x} Fe_2 O_4$, and (c) $Al_x Mn_{1-x} Fe_2 O_4$ samples (from Ding et al. [108]).

that both a and v change only slightly when $x < 0.20$, while both of them decrease with increasing x when $x > 0.20$; and (iii) θ gradually increases. These crystal structure dependencies on x are related to those of the magnetic moment and T_C .

The magnetic hysteresis loops of the $La_{1-x} Sr_x MnO_3$ samples ($0 \leq x \leq 0.4$) were measured at $T = 10$ K. σ_s and μ_{obs} per formula are listed in Table 15. It can be seen that μ_{obs} rapidly increases with increasing x when $x \leq 0.15$, while it slowly decreases with increasing x when $x \geq 0.15$. The maximum value obtained is $\mu_{obs} = 4.19 \mu_B$, which occurs at $x = 0.15$. The observed trend in μ_{obs} is similar to those reported by Jonker and Van Santen [28] and Urushibara et al. [33], as shown in Table 15 and Fig. 30.

To discuss the dependence of the magnetic moments of the samples on x , the ionicities of the samples were studied using XPS analysis. Fig. 31(a)–(e) show the O 1s spectra for the $La_{1-x} Sr_x MnO_3$ samples ($x = 0.05, 0.10, 0.15, 0.20$ and 0.25) [110]. One can see that the O 1s spectrum can be fitted using three peaks with different binding energies (BEs). According to the interpretation proposed by Dupin et al. [57] and Wu et al. [58,59], the lower BE peak can be assigned to O^{2-} ions, the middle

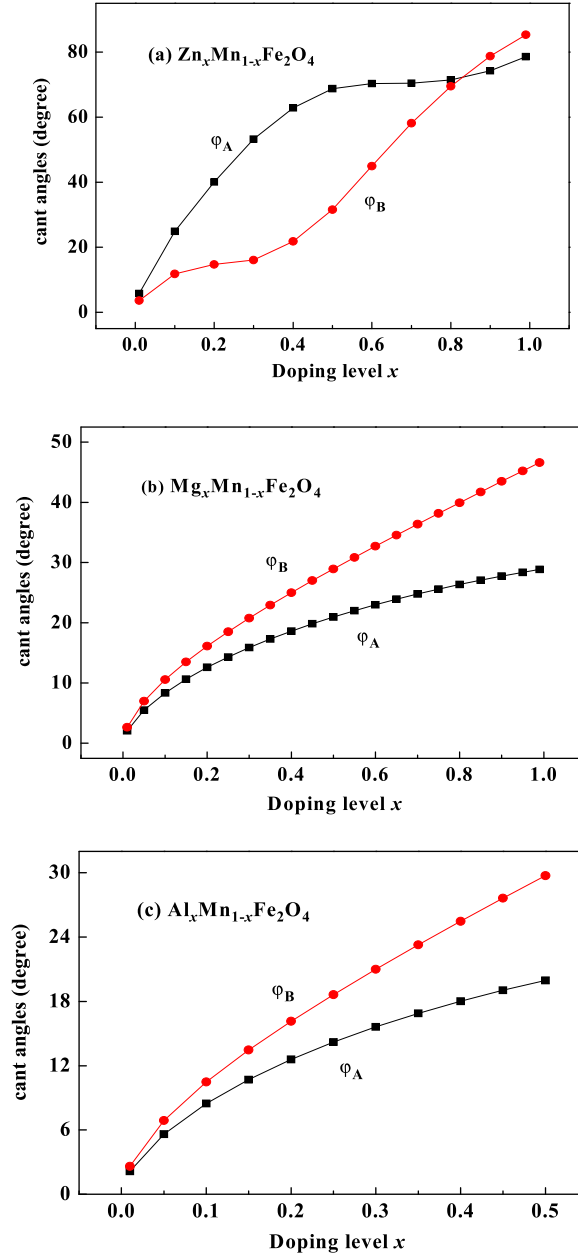


Fig. 25. Angles between the magnetic moments of neighboring metal cations in the (A) and [B] sublattices, φ_A and φ_B , in (a) $Zn_xMn_{1-x}Fe_2O_4$, (b) $Mg_xMn_{1-x}Fe_2O_4$, and (c) $Al_xMn_{1-x}Fe_2O_4$ samples, as functions of x (from Ding et al. [108]).

BE peak to O^{1-} ions, and the higher BE peak to O^{chem} , i.e., chemically adsorbed O on the sample surface. Fig. 31(f) shows the same O 1s photoelectron spectra with the peak intensities normalized to the same maximum value. It can be seen from Fig. 31 (f) that the ratio of the peak intensity of the O^{1-} ions to that of the O^{2-} ions reaches a minimum when $x = 0.15$. The XPS fitting data are shown in Table 16. Setting $O_1/O_2 = S_1/S_2$, where O_1/O_2 and S_1/S_2 represent the ratios between the amounts and peak areas, respectively, of the O^{1-} and O^{2-} anions and requiring that $O_1 + O_2 = 1$, we can write

$$O_2 = \frac{1}{1 + S_1/S_2}, \quad O_1 = 1 - O_2. \quad (5.1)$$

V_{alO} can then be obtained as

$$V_{alO} = -2O_2 - O_1. \quad (5.2)$$

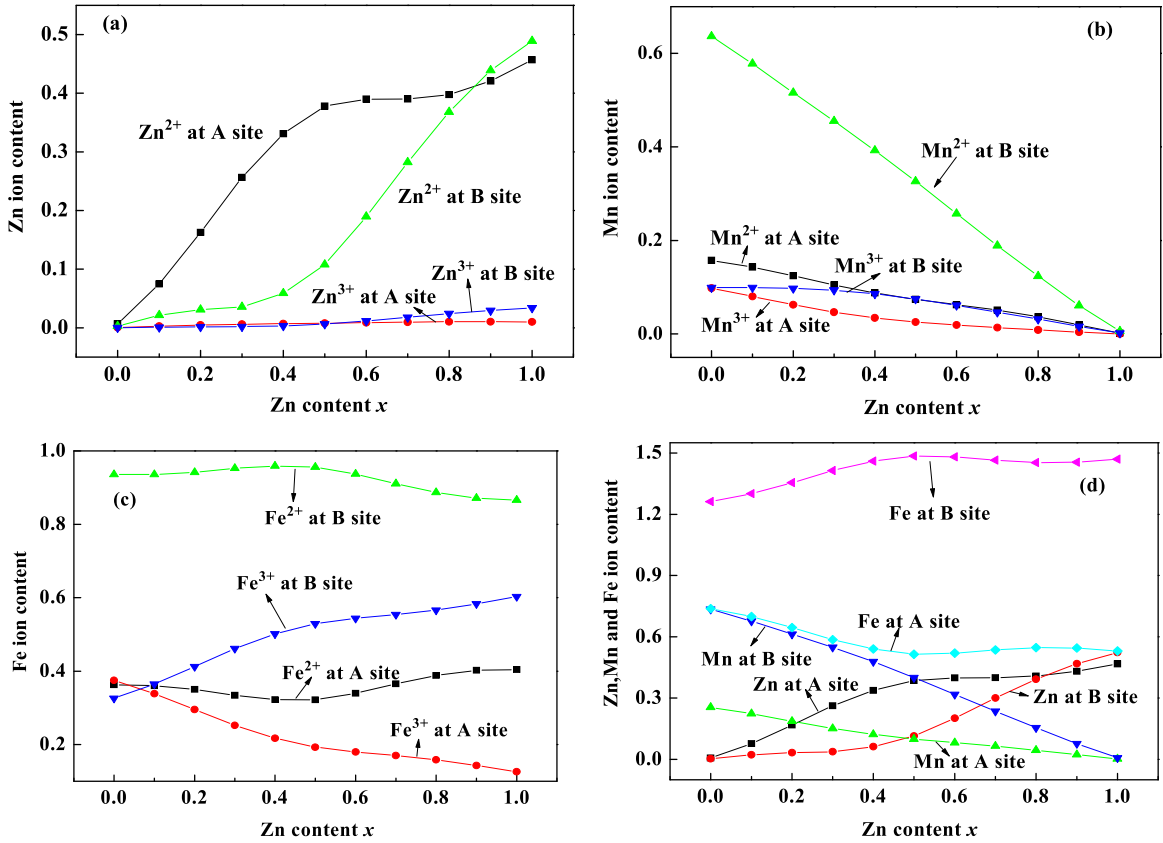


Fig. 26. Estimated cation distributions at the (A) and [B] sites of (a) Zn, (b) Mn, (c) Fe, and (d) the sum of the divalent and trivalent cations in the $Zn_x Mn_{1-x}Fe_2O_4$ samples, as functions of x (from Ding et al. [108]).

Table 14

Rietveld fitted results of the XRD pattern for $La_{1-x}Sr_xMnO_3$ samples (Wu et al. [110]). Here, R_p , R_{wp} , and s are the profile factor, weighted profile factor, and goodness of fit indicator, respectively. a and c are the lattice parameters; v , d_{AO} , d_{BO} , and θ are the cell volume, La/Sr–O bond length, Mn–O bond length, and Mn–O–Mn bond angle, respectively.

Content	a (Å)	c (Å)	v (Å ³)	d_{AO} (Å)	d_{BO} (Å)	θ (deg.)	$R_p(\%)$	$R_{wp}(\%)$	s
0.00	5.5247	13.3326	352.427	2.4696	1.9656	162.9	4.69	6.12	1.47
0.05	5.5247	13.3322	352.405	2.4768	1.9645	163.3	4.82	6.33	1.54
0.10	5.5231	13.3408	352.428	2.4846	1.9633	163.8	4.68	6.16	1.50
0.15	5.5198	13.3505	352.274	2.4950	1.9614	164.5	4.86	6.24	1.56
0.20	5.5196	13.3560	352.396	2.5082	1.9598	165.2	4.39	5.73	1.46
0.25	5.5117	13.3609	351.508	2.5183	1.9564	166.1	4.44	5.64	1.46
0.30	5.5045	13.3647	350.693	2.5377	1.9523	167.4	4.05	5.10	1.33
0.35	5.4973	13.3673	349.849	2.5530	1.9487	168.5	3.88	4.89	1.30
0.40	5.4870	13.3634	348.433	2.5648	1.9445	169.5	3.77	4.79	1.30

From V_{alO} , the ionicities of the materials can be obtained by setting the ionicity of O f_{iO} equal to $|V_{alO}|/2$. The resulting V_{alO} and f_{iO} data are presented in Table 16. It can be seen that f_{iO} for the $La_{1-x}Sr_xMnO_3$ samples ($0.05 \leq x \leq 0.25$) measured using XPS is between 0.825 and 0.855, while V_{alO} is between -1.65 and -1.71 . These values are close to V_{alO} (-1.63) in $BaTiO_3$, as was calculated by Cohen [56]. Here, the contribution from chemically adsorbed O on the surface was not accounted for here.

To explore the valence of Mn in these compounds, the average valences for powder samples of the Mn oxides MnO , Mn_3O_4 , $CaMnO_3$, and $SrMnO_3$ were studied using XPS analysis. Fig. 32 shows the fitted results of the O 1s spectra for each sample. V_{alO} for the MnO and Mn_3O_4 samples was determined to be -1.73 and -1.78 , respectively, while the average valences of Mn ions in the samples were found to be $+1.73$ and $+2.37$, respectively, using the principle of valence balance. For the $CaMnO_3$ and $SrMnO_3$ samples, V_{alO} was determined to be -1.54 and -1.66 , respectively, while the average valences of the Sr and Ca cations in the samples were taken to be $+2.00$, as for the valences of Ba in $BaTiO_3$ [56,58] and Sr in $SrTiO_3$ [59]. The average valence of the Mn ions in the samples was then determined, by valence balance, to be $+2.62$ and $+2.98$, respectively. These

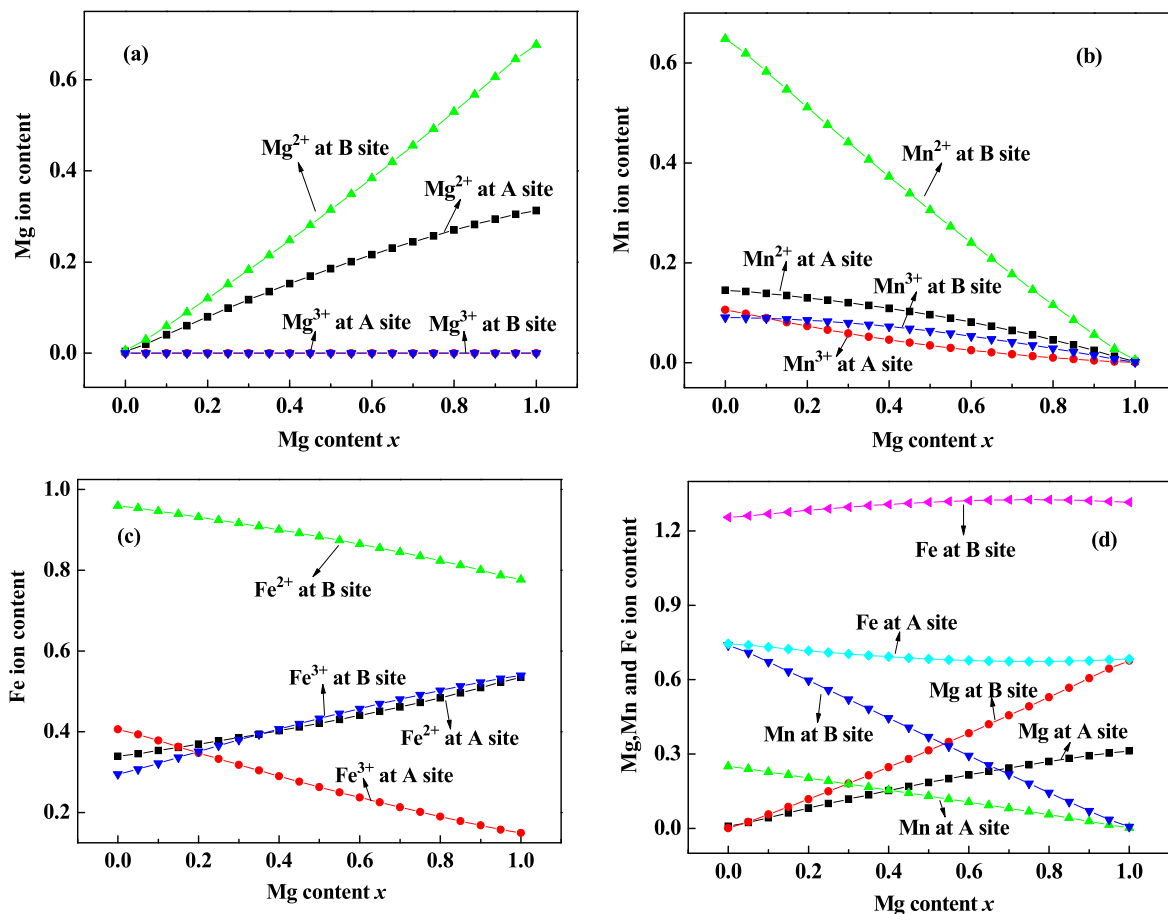


Fig. 27. Estimated cation distributions at the (A) and [B] sites of (a) Mg, (b) Mn, (c) Fe, and (d) the sum of the divalent and trivalent cations in the $Mg_x Mn_{1-x}Fe_2O_4$ samples, as functions of x (from Ding et al. [108]).

Table 15

Specific saturation magnetization σ_s of $La_{1-x}Sr_xMnO_3$ samples measured at 10 K (Wu et al. [109,110]). μ_{obs} is the magnetic moment per formula measured at 10 K, and T_C is the Curie temperature. The results reported by Urushibara et al. [33] and Jonker et al. [28] are listed as well.

Content x	σ_s (Am ² /kg) Wu [109]	Magnetic moment μ_{obs} (μ_B /formula)			T_C (K)	
		Wu [109]	Urushibara et al. [33]	Jonker et al. [28]	Wu [109]	Urushibara et al. [33]
0.00	–	–	–	0	–	–
0.05	54.45	2.33	–	–	107.7	139
0.10	77.20	3.27	3.6	3.08	168.3	145
0.15	99.91	4.19	4.2	–	216.5	238
0.20	85.15	3.53	3.9	3.73	292.7	309
0.25	84.09	3.45	3.9	–	313.7	342
0.30	83.72	3.39	3.5	3.71	337.2	369
0.35	79.95	3.21	–	3.66	350.4	–
0.40	79.88	3.17	3.4	3.51	348.9	371

results are listed in Table 17, which clearly indicates that the average valence of the Mn ions increases as the anion/cation ratio increases. Since the average valences of Mn in $CaMnO_3$ and $SrMnO_3$, which have anion/cation ratios of 3:2, are +2.62 and +2.98, respectively (i.e., both less than 3.00), the average valence of Mn in $La_{1-x}Sr_xMnO_3$, which has the same anion/cation ratio of 3:2, should therefore also be less than +3.00. In other words, both Mn^{2+} and Mn^{3+} cations should be present in $LaMnO_3$.

As is well known, Mn cations have antiferromagnetic structures in $LaMnO_3$ [22–24]. According to the IEO model in Fig. 8, the magnetic moments of the Mn^{2+} cations in $LaMnO_3$ are directed oppositely to those of the Mn^{3+} cations. Since the ratio between the magnetic moments of Mn^{2+} and Mn^{3+} cations is 5/4 and the total magnetic moment of the sample is zero [28], it can easily be determined that the ratio between the contents of Mn^{2+} and Mn^{3+} cations is 4/5 and, therefore, that the

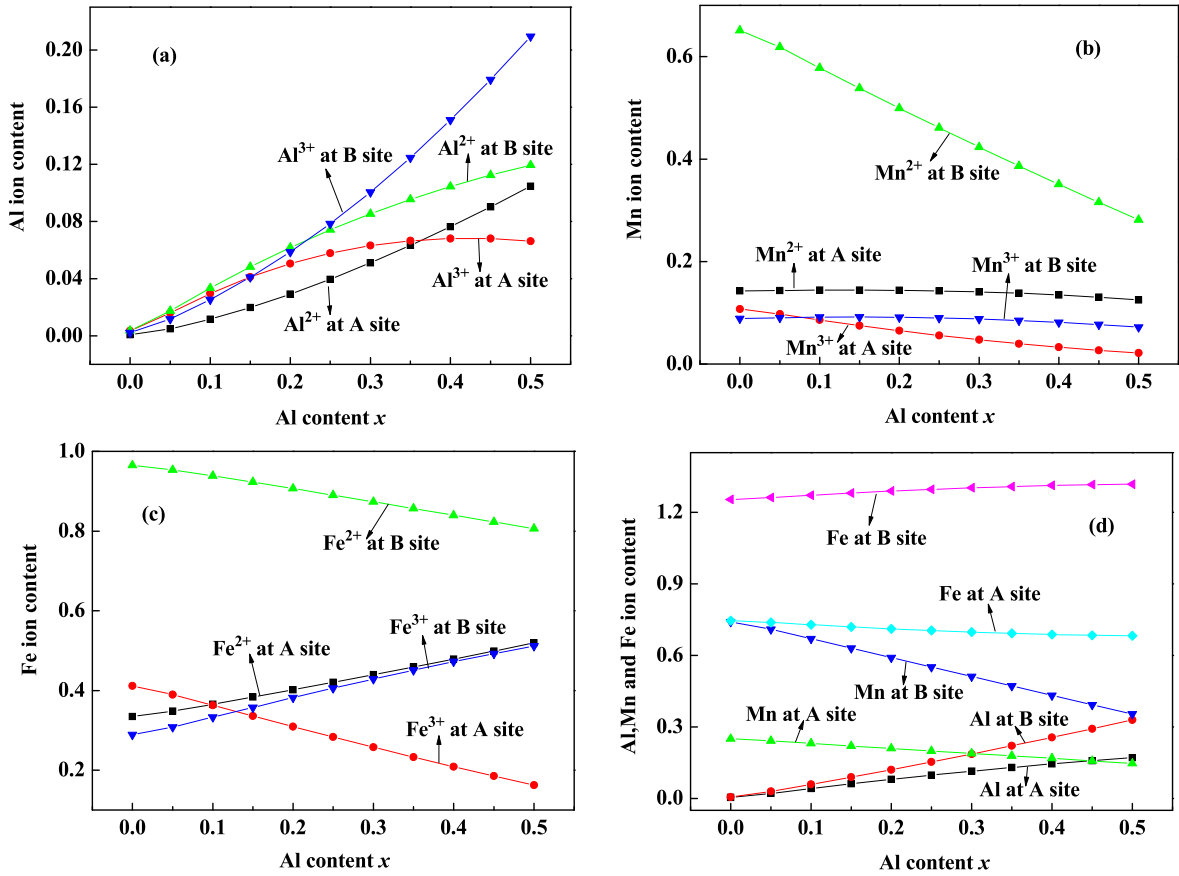


Fig. 28. Estimated cation distributions at the (A) and [B] sites of (a) Al, (b) Mn, (c) Fe, and (d) the sum of the divalent and trivalent cations in the $\text{Al}_x\text{Mn}_{1-x}\text{Fe}_2\text{O}_4$ samples, as functions of x (from Ding et al. [108]).

Table 16

Fitting results for the O 1s photoelectron spectra of $\text{La}_{1-x}\text{Sr}_x\text{MnO}_3$ samples. E , ΔE , FWHM, S , V_{aio} , and f_{io} represent the binding energy at the peak position, chemical shift from Peak P2 or P3 to P1, full-width at half-maximum, peak area normalized to 100%, average valence of O ions, and ionicity of O, respectively (from Wu et al. [110]).

Composition	E (eV)	ΔE (eV)	FWHM (eV)	S (%)	V_{aio}	f_{io}
$\text{La}_{0.95}\text{Sr}_{0.05}\text{MnO}_3$	529.43	–	1.54	47.37	–1.65	0.825
	531.04	1.61	1.41	25.15		
	532.14	2.71	1.85	27.48		
$\text{La}_{0.9}\text{Sr}_{0.1}\text{MnO}_3$	529.23	–	1.59	49.33	–1.68	0.840
	530.81	1.58	1.50	23.36		
	532.06	2.83	2.11	27.31		
$\text{La}_{0.85}\text{Sr}_{0.15}\text{MnO}_3$	529.31	–	1.40	55.05	–1.71	0.855
	530.92	1.61	1.56	22.20		
	532.09	2.78	2.07	22.75		
$\text{La}_{0.8}\text{Sr}_{0.2}\text{MnO}_3$	529.19	–	1.40	51.28	–1.68	0.840
	530.99	1.80	1.56	24.39		
	532.36	3.17	2.07	24.33		
$\text{La}_{0.75}\text{Sr}_{0.25}\text{MnO}_3$	528.98	–	1.96	51.13	–1.67	0.835
	530.72	1.74	1.88	25.75		
	532.16	3.18	2.30	23.12		

ionicity of the Mn cations is given by

$$f_{\text{Mn},0.0} = \left(2 \times \frac{4}{9} + 3 \times \frac{5}{9} \right) / 3 = 0.8519. \quad (5.3)$$

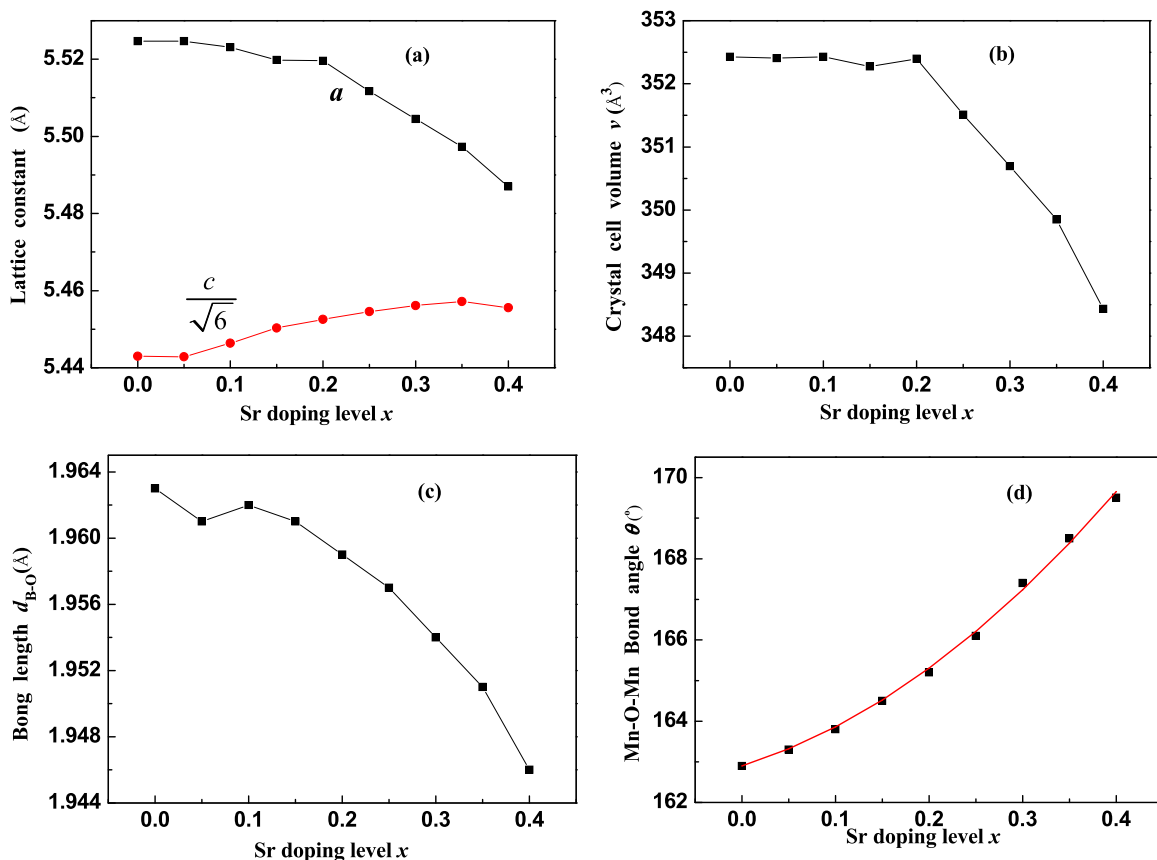


Fig. 29. (a) The lattice parameters, a and c , (b) the crystal cell volume, v , (c) the B–O (Mn–O) bond length, d_{B-O} , and (d) the B–O–B (Mn–O–Mn) bond angle, θ for $\text{La}_{1-x}\text{Sr}_x\text{MnO}_3$ samples, as functions of x (from Wu et al. [109]).

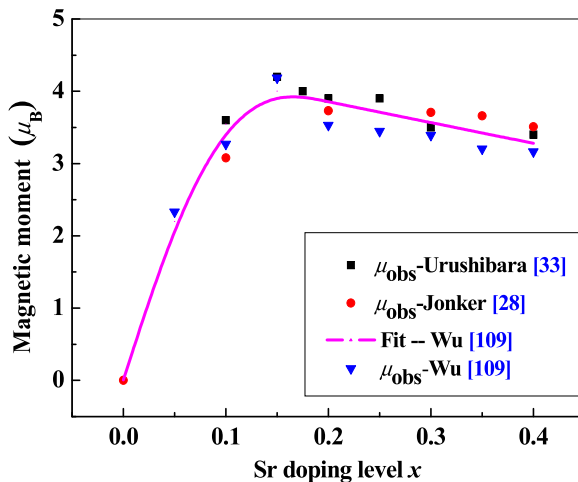


Fig. 30. Fitted magnetic moments μ_{cal} (curve) by Wu et al. [109] and observed values μ_{obs} by Wu et al. [109] (\blacktriangledown), Urushibara et al. [33] (\blacksquare), and Jonker Van Santen [28] (\bullet), for $\text{La}_{1-x}\text{Sr}_x\text{MnO}_3$ samples, as functions of x .

In their investigations, both Urushibara et al. [33] and Wu et al. [109,110] found that the magnetic moment achieved its maximum value at $x = 0.15$. One can therefore assume that when $x = 0.15$, all of the Mn ions are Mn^{3+} cations. Thus, at this point, the valence of all of the Mn cations is 3.0, and consequently, the ionicity of the Mn cations is given by $f_{\text{Mn}^{3+}} = 1.00$. To fit the observed trend in the sample magnetic moments as a function of x when $x \leq 0.15$ (as shown in Table 15 and Fig. 30),

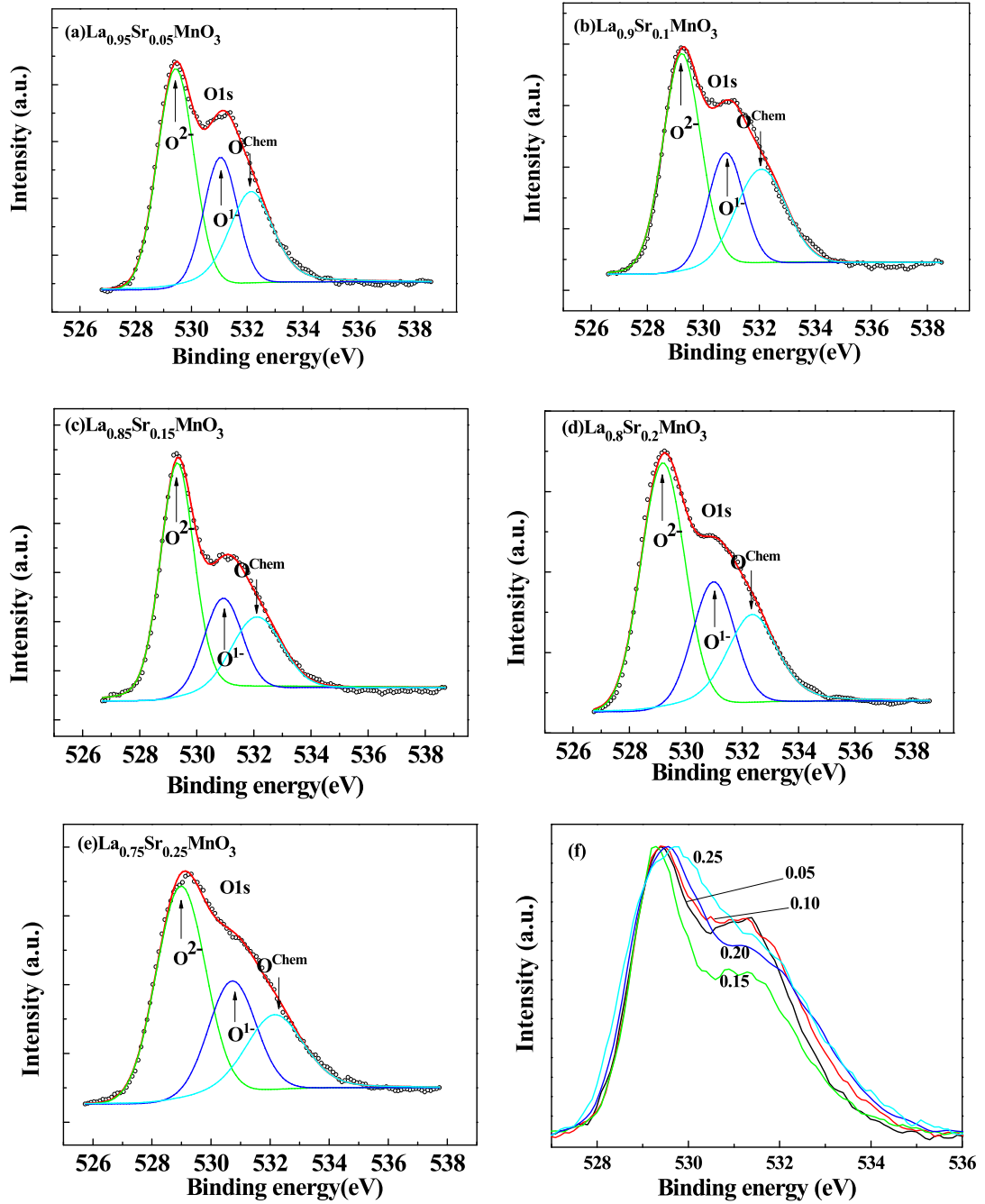


Fig. 31. O 1s photoelectron spectra with fitted results for (a) $\text{La}_{0.95}\text{Sr}_{0.05}\text{MnO}_3$, (b) $\text{La}_{0.9}\text{Sr}_{0.1}\text{MnO}_3$, (c) $\text{La}_{0.85}\text{Sr}_{0.15}\text{MnO}_3$, (d) $\text{La}_{0.8}\text{Sr}_{0.2}\text{MnO}_3$, and (e) $\text{La}_{0.75}\text{Sr}_{0.25}\text{MnO}_3$ powder samples. (f) Normalized O 1s photoelectron spectra for the $\text{La}_{1-x}\text{Sr}_x\text{MnO}_3$ samples (from Wu et al. [110]).

the ionicity of the Mn cations was assumed to vary as

$$f_{\text{Mn}} = \sin(\theta_1 + cx), \quad (0.00 \leq x \leq 0.15).$$

Applying the boundary conditions, $f_{\text{Mn},0.00} = 0.8519$ and $f_{\text{Mn},0.15} = 1.00$, one can then easily determine that

$$f_{\text{Mn}} = \sin(1.0196 + 3.6747x), \quad (0.00 \leq x \leq 0.15), \quad (5.4)$$

where radians were used as the angular units. Using Eq. (5.4), the ionicity of Mn for the $\text{La}_{1-x}\text{Sr}_x\text{MnO}_3$ samples at $x = 0.05$, 0.10, and 0.15 was determined to be 0.933, 0.981, and 1.000, respectively.

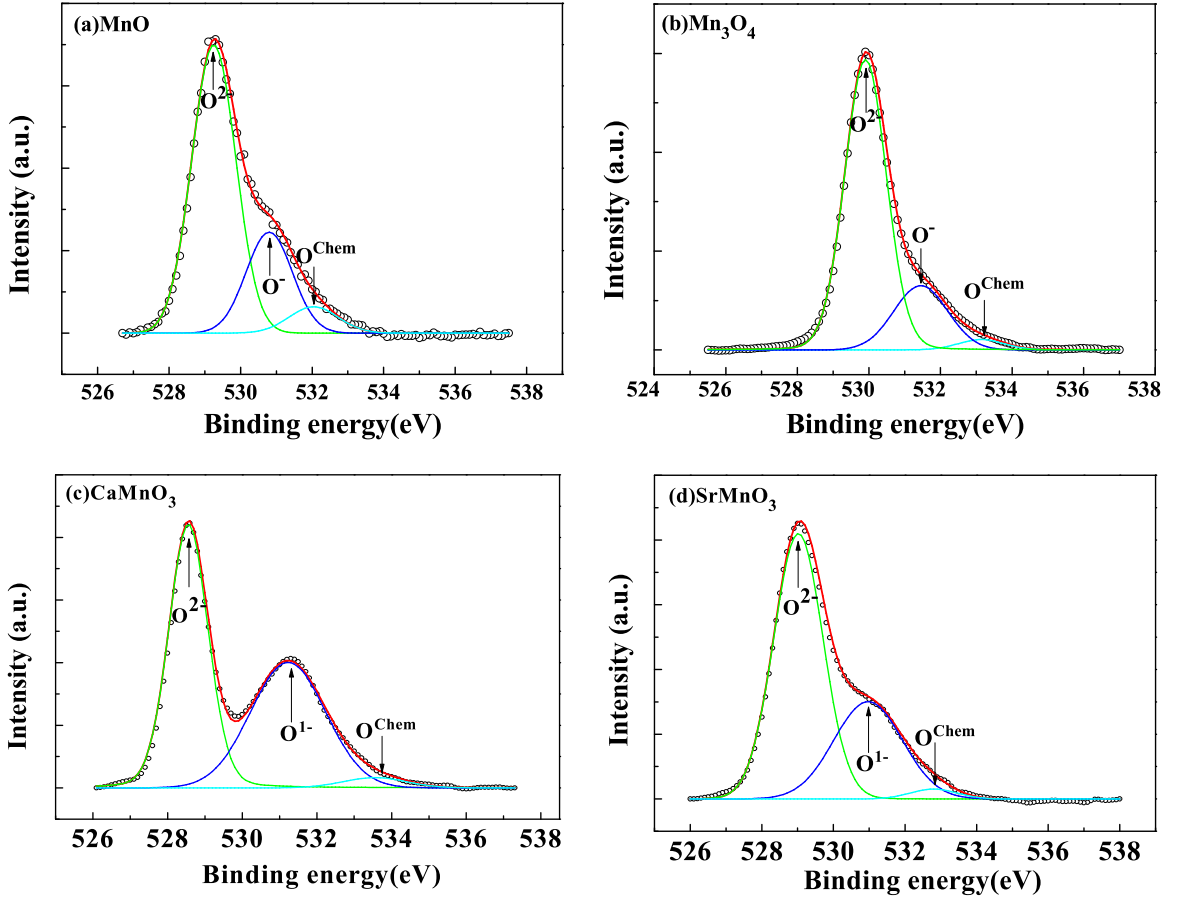


Fig. 32. O 1s photoelectron spectra for (a) MnO, (b) Mn₃O₄, (c) CaMnO₃, and (d) SrMnO₃ samples with fitted results (from Wu et al. [110]).

Table 17

Average valence of Mn cations V_{alM} in MnO, Mn₃O₄, CaMnO₃, and SrMnO₃ samples, as calculated using the average valences of O, V_{alO} , and the average valence of Sr(Ca) $V_{\text{alS(alC)}}$ (from Wu et al. [110]).

Sample	Average Valence		
	V_{alO}	$V_{\text{alS(alC)}}$	V_{alM}
MnO	-1.73	-	1.73
Mn ₃ O ₄	-1.78	-	2.37
CaMnO ₃	-1.54	2.00	2.62
SrMnO ₃	-1.66	2.00	2.98

Moreover, the contents of Mn²⁺ and Mn³⁺ cations can also be obtained from Eq. (5.4) and are given by

$$M_2 = 3 - 3f_{\text{Mx}} \quad \text{and} \quad M_3 = 1 - M_2 \quad (0.00 \leq x \leq 0.15), \quad (5.5)$$

respectively. From these values, the magnetic moment of the samples is then given by

$$\mu_{\text{cal}} = 4M_3 - 5M_2 \quad (0.00 \leq x \leq 0.15). \quad (5.6)$$

To explain the fact that the magnetic moments decrease with increasing x when $x > 0.15$, it was assumed that the samples had canted ferromagnetic structures when $x > 0.15$ and that the magnetic moments varied linearly with x as

$$\mu_{\text{cal}} = 4[1 - 0.72(x - 0.15)] \quad (0.15 \leq x \leq 0.40), \quad (5.7)$$

where the fitting parameter, 0.72, was obtained by fitting the data with the values of the magnetic moments vs. x in Table 15. Fig. 30 shows the dependence of the magnetic moments on x for the La_{1-x}Sr_xMnO₃ samples, where the curve represents the fitted results obtained using Eqs. (5.6) and (5.7). The triangles (▼), squares (■), and circles (●) represent the results reported

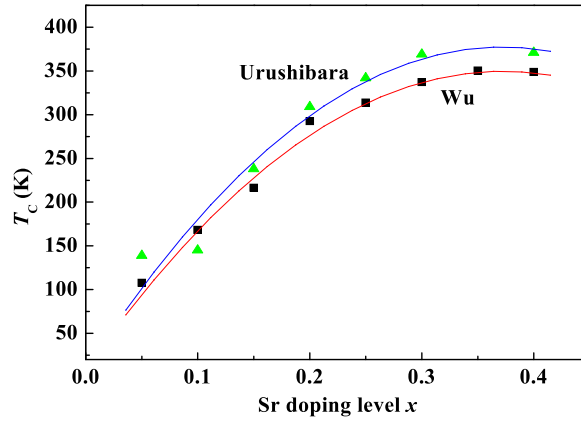


Fig. 33. Curie temperature T_C of $\text{La}_{1-x}\text{Sr}_x\text{MnO}_3$ samples as functions of x , reported by Wu et al. [110] (■) and Urushibara et al. [33] (▲).

Table 18

Mn^{3+} and Mn^{2+} contents, m_3 and m_2 , calculated using μ_{obs} of the $\text{La}_{0.95}\text{Sr}_{0.05}\text{MnO}_3$ samples with different thermal treatment conditions (from Wu et al. [72]).

Sample	State of samples/temperature (K)/time(h) of thermal-treatment	$\mu_{\text{obs}} (\mu_B)$	m_3	m_2
A ₁	powder/1073/10, pellet/1273/10	1.853	0.7614	0.2386
A ₂	powder/1073/10, pellet/1273/10, powder/1273/10	2.638	0.8487	0.1513
A ₃	powder/873/5, powder/1073/10, pellet/1273/10, powder/1273/10	3.220	0.9133	0.0867

by Wu et al. [109,110], Urushibara et al. [33], and Jonker and Van Santen [28], respectively (cf. Table 15). It can be seen that the fitted curve is very close to the average of the observed results.

The angles between the magnetic moments of the Mn^{3+} cations can be obtained from Eq. (5.7):

$$\phi = \frac{180}{\pi} \arccos [1 - 0.72(x - 0.15)] \quad (0.15 \leq x \leq 0.40), \quad (5.8)$$

where ϕ is measured in degrees. It is easy to calculate that $\phi = 34.9^\circ$ when $x = 0.40$. This assumption regarding the canted magnetic structures of the cations in $\text{La}_{1-x}\text{Sr}_x\text{MnO}_3$ when $x > 0.15$ has also been confirmed by magnetoresistance (MR) experiments, which will be discussed in Section 5.4.

It can be seen from Table 15 and Fig. 33 that T_C increases with increasing x for the $\text{La}_{1-x}\text{Sr}_x\text{MnO}_3$ samples, while the slopes of the curves decrease with increasing x . Moreover, the experimental results obtained from powder samples and reported by Wu et al. [109,110] agree well with those obtained from single crystals and reported by Urushibara et al. [33]. This phenomenon can be explained using the IEO model as follows. (i) When $x < 0.15$, the content of Mn^{2+} cations decreases and the amount of Mn^{3+} cations increases with increasing x . According to the IEO model, when a spin-up electron transits between the $\text{O}^{2-}-\text{Mn}^{3+}-\text{O}^{1-}$ bonds, as shown in Fig. 7(b), it expends little energy. However, when a spin-up electron transits between $\text{O}^{2-}-\text{Mn}^{2+}-\text{O}^{1-}$ bonds, as shown in Fig. 7(d), it must expend more energy because the magnetic moment of the Mn^{2+} cations is opposite to the spin of the itinerant electron. This characteristic causes the total magnetic ordering energy to increase as the ratio between the contents of Mn^{2+} and Mn^{3+} cations decreases, and consequently, T_C increases as the amount of Mn^{2+} cations decreases. (ii) When $x > 0.15$, the Mn–O bond length decreases with increasing x , while the Mn–O–Mn bond angle increases, as shown in Fig. 29. Both of these phenomena may cause T_C to increase [22–24].

5.2. Influence of thermal treatment on the ionic valences and magnetic structures of the perovskite manganites $\text{La}_{0.95}\text{Sr}_{0.05}\text{MnO}_3$

As mentioned in Section 5.1, the ratio between the amounts of Mn^{2+} and Mn^{3+} cations is related to x in $\text{La}_{1-x}\text{Sr}_x\text{MnO}_3$ when $x < 0.15$. In addition, the average valence of the Mn cations is related to the thermal treatment conditions. Töpfer et al. [116] and Prado et al. [117] reported that the magnetic moment of LaMnO_3 can vary from $0 \mu_B$ to $3 \mu_B$ under different preparation conditions. Wu et al. [72] prepared three samples with nominal compositions of $\text{La}_{0.95}\text{Sr}_{0.05}\text{MnO}_3$ with different thermal-treatment conditions (cf. Table 18). They found the magnetic moments of the samples at $T = 10$ K to be 1.85, 2.64, and $3.22 \mu_B$. Using the method mentioned in Section 5.1, they determined from their XPS analysis that there were only Mn^{2+} and Mn^{3+} cations in these three samples and that the average valence of Mn in the samples increased with increasing thermal treatment. Using the IEO model, they explained this magnetic structure and provided the contents of Mn^{2+} and Mn^{3+} cations, m_2 and m_3 , respectively, as listed in Table 18.

Table 19

Thermal treatment conditions of the two different series of samples $\text{La}_{0.95}\text{T}_{0.05}\text{Cr}_x\text{Mn}_{1-x}\text{O}_3$ ($T = \text{Ca}$ or Sr , $0.00 \leq x \leq 0.30$): states of the samples, temperature (K), and duration (h) of thermal treatment.

Samples	First	Second	Third	Fourth
Ca-series	Powder; 1073; 10	Pellet; 1273; 10	–	–
Sr-series	Powder; 873; 10	Powder; 1073; 10	Pellet; 1273; 10	Powder; 1273; 10

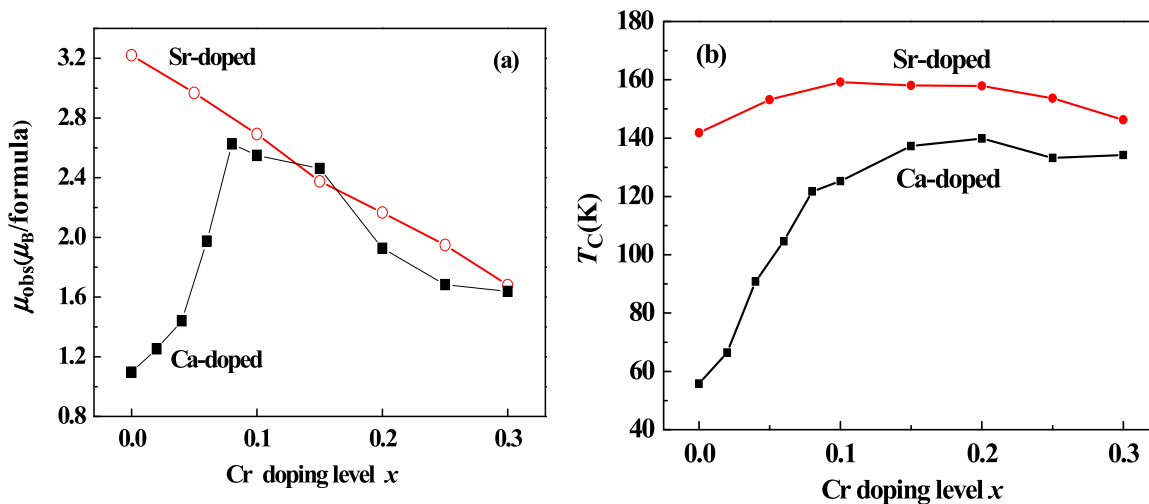


Fig. 34. Cr-doping level x dependences of (a) the observed magnetic moments, μ_{obs} , and (b) Curie temperature, T_C , for powder samples with the composition $\text{La}_{0.95}\text{Ca}_{0.05}\text{Cr}_x\text{Mn}_{1-x}\text{O}_3$ (Ca-doped samples) and $\text{La}_{0.95}\text{Sr}_{0.05}\text{Cr}_x\text{Mn}_{1-x}\text{O}_3$ (Sr-doped samples) (from Li et al. [122]).

5.3. Magnetic structures in several series of perovskite manganites with Fe and Cr doping

A number of studies have been focused on the effects of doping in perovskite manganites. Jiang and Gong [118] found that the specific magnetizations of samples of $\text{La}_{0.8}\text{Sr}_{0.2}\text{Mn}_{1-y}\text{Co}_y\text{O}_3$ decreased with increasing y . They explained this behavior by assuming that the Co and Mn cations were coupled antiferromagnetically. In contrast, Sun et al. [119] investigated the magnetic properties of $\text{La}_{0.67}\text{Sr}_{0.33}\text{Mn}_{1-x}\text{Cr}_x\text{O}_3$ samples and determined that there was a ferromagnetic interaction between the Cr and Mn cations. Blanco et al. [120] examined the magnetic properties of $\text{Nd}_{0.7}\text{Pb}_{0.3}\text{Mn}_{1-x}\text{Fe}_x\text{O}_3$ samples, concluding that the magnetic moments of the samples decreased with increasing x . They assumed that the ferromagnetic interaction was weakened and the antiferromagnetic interaction was strengthened due to the Fe doping. Yang et al. [121] studied the magnetic properties of $\text{La}_{2/3}\text{Sr}_{1/3}\text{Fe}_x\text{Mn}_{1-x}\text{O}_3$ samples. They also found that the magnetic moments of the samples decreased with increasing x .

According to Sections 3 and 5.1, all of these experimental results can be easily explained using the third postulate of the IEO model. Since the divalent element content at A sites in all of these perovskite manganites is greater than 0.15, all of the cations at B sites are trivalent. Thus, Cr^{3+} ($3d^3$) is coupled ferromagnetically with Mn^{3+} ($3d^4$), while Co^{3+} ($3d^6$) and Fe^{3+} ($3d^5$) are coupled antiferromagnetically with Mn^{3+} ($3d^4$), since the spin direction of the itinerant electron remains constant throughout the B sublattice of the ABO_3 perovskite structure, and further constraints arising from Hund's rules. Thus, the IEO model can explain all of these results simply and reasonably.

Li et al. [122] synthesized powder samples of $\text{La}_{0.95}\text{T}_{0.05}\text{Cr}_x\text{Mn}_{1-x}\text{O}_3$ ($T = \text{Ca}$ or Sr , $0.00 \leq x \leq 0.30$), two series of ABO_3 perovskite manganites, via the sol-gel method. As shown in Table 19, the thermal treatment conditions were different for the two series of samples. The Ca-doped samples were thermally treated twice: after the samples were calcined at 1073 K for 10 h, the powders were then compressed into pellets measuring 13 mm in diameter and 2 mm in thickness to promote contact at the grains boundaries before they were finally calcined at 1273 K for 10 h. The Sr-doped samples were thermally treated in four steps: first, they were thermally treated at 873 K for 5 h, after which they were thermally treated two more times using the same procedure that was employed for the Ca-doped samples; finally, the sample powders were calcined at 1273 K for 10 h. XRD analysis showed that all of the samples had single ABO_3 perovskite phases with space group $R\bar{3}c$. Unique magnetic properties were obtained for the oxides: (i) the average molecular magnetic moment reached the maximum value when $x = 0.08$ for the Ca-doped samples, but it monotonically decreased with increasing x for the Sr-doped samples, as shown Fig. 34(a); and (ii) T_C of each series of samples first increased and then decreased with increasing x , as shown Fig. 34(b). Using the IEO model and the magnetic moments of the samples, the ion contents of Mn^{2+} , Mn^{3+} , Cr^{2+} , and Cr^{3+} , M_2 , M_3 , C_2 , and C_3 , respectively, in the samples were estimated and the following phenomena were identified. (i) The magnetic moments of the Mn^{2+} cations coupled antiferromagnetically with those of the Mn^{3+} and Cr cations in the Ca-doped samples with x

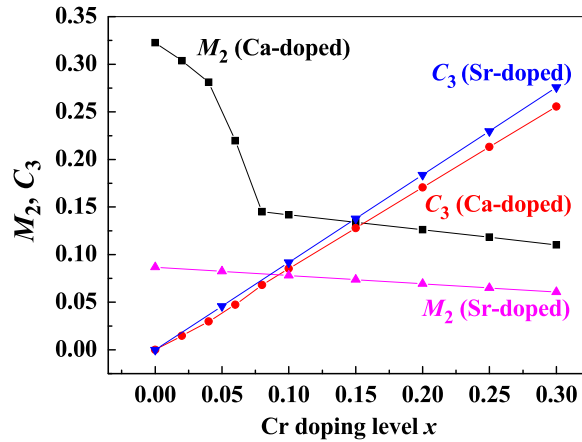


Fig. 35. Dependences of contents of Mn^{2+} and Cr^{3+} cations (M_2 and C_3) on Cr doping level x for Ca- and Sr-doped samples (from Li et al. [122]).

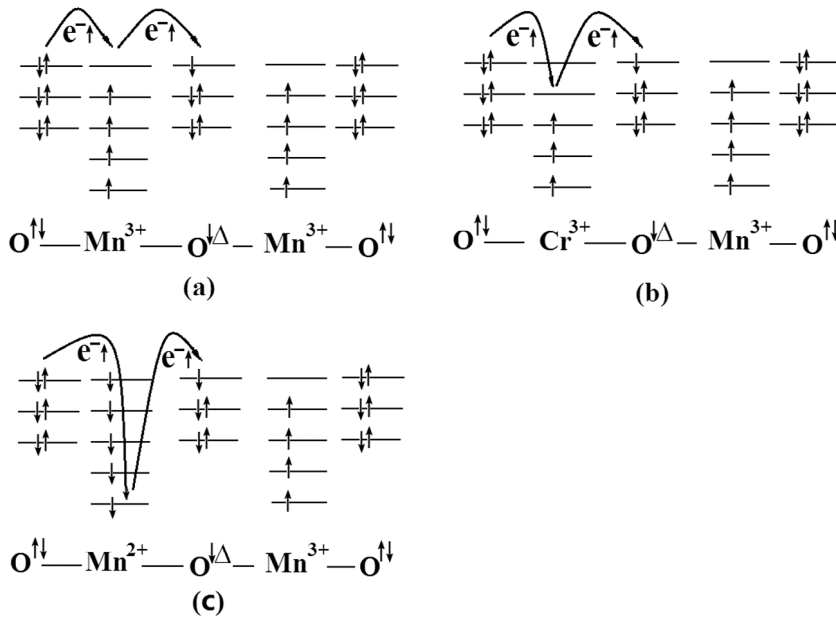


Fig. 36. Schematic diagrams of the transfer process of spin-up itinerant electrons along the (a) $O^{2-}-Mn^{3+}-O^{1-}-Mn^{3+}-O^{2-}$, (b) $O^{2-}-Cr^{3+}-O^{1-}-Mn^{3+}-O^{2-}$, and (c) $O^{2-}-Mn^{2+}-O^{1-}-Mn^{3+}-O^{2-}$ ion chains. An arrow drawn on a $3d$ energy level represents an electron with a specific spin direction. Δ represents a $2p$ hole, which in the illustrated case represents the absence of a spin-up electron (from Li et al. [122]).

≤ 0.08 and the Sr-doped sample with $x = 0.00$. (ii) There were canted antiferromagnetic structures between the magnetic moments of the Mn^{2+} cations and those of the Mn^{3+} and Cr cations in the Ca-doped samples with $x \geq 0.10$ and the Sr-doped samples with $x \geq 0.05$. (iii) M_2 and C_3 are shown as functions of x in Fig. 35. Similarly to Fig. 7 and Fig. 19, Fig. 36 suggests that the consumed energy increased successively when an itinerant electron was transferred via Mn^{3+} , Cr^{3+} , and Mn^{2+} . Therefore, a decrease in Mn^{2+} cations when $x < 0.08$ resulted in an increase in T_C , and an increase in Cr^{3+} cations when $x > 0.20$ resulted in a decrease in T_C . Therefore, the IEO model reasonably explains the dependence of T_C on x for both Sr- and Ca-doped perovskite manganites.

5.4. Magnetic structures of the perovskite manganites $Pr_{0.6}Sr_{0.4}M_xMn_{1-x}O_3$

To study the magnetic structures of perovskite manganites, Ge et al. [123–125] synthesized powder samples of the ABO_3 perovskite manganites $Pr_{0.6}Sr_{0.4}M_xMn_{1-x}O_3$ ($M = Cr, Fe, Co, \text{ or } Ni$) and investigated the crystal structures and magnetic and electrical transport properties of the samples. All of the samples had single-phase, orthorhombic structures with the space group $Pbnm$. As before, the volume-averaged diameters of the crystallites were estimated based on the Scherrer equation

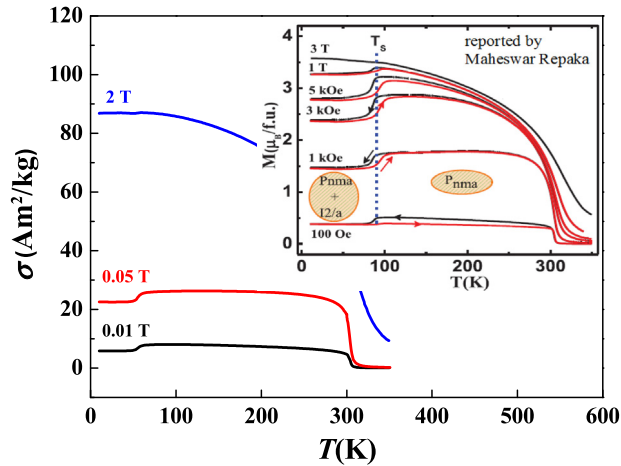


Fig. 37. Specific magnetization σ versus temperature T for $\text{Pr}_{0.6}\text{Sr}_{0.4}\text{MnO}_3$ under different magnetic fields (from Ge et al. [123]). The inset shows the results for $\text{Pr}_{0.6}\text{Sr}_{0.4}\text{MnO}_3$ reported by Maheswar Repaka et al. [126].

and were found to be greater than ~ 100 nm for all of the samples. Thus, the surface effects were again expected to be very weak. The magnetic hysteresis loops were measured at 10 K with applied magnetic fields of up to 2 T for the Cr-, Fe-, and Ni-doped samples, and up to 4 T for the Co-doped samples. Using the specific saturation magnetization σ_s , the average magnetic moments μ_{obs} was calculated per formula for each sample. The magnetic structures of the samples are discussed below.

5.4.1. Magnetic structure of $\text{Pr}_{0.6}\text{Sr}_{0.4}\text{MnO}_3$

Applying XPS and a procedure similar to that outlined in Section 5.1, the ionic valences in the $\text{Pr}_{0.6}\text{Sr}_{0.4}\text{MnO}_3$ sample were estimated to be $\text{Pr}^{2.68+}$, $\text{Sr}^{2.00+}$, $\text{Mn}^{2.91+}$, and $\text{O}^{1.77-}$. The dependences of the specific magnetization on the measurement temperature and applied field are shown in Fig. 37 and are similar to those reported by Maheswar Repaka et al. [126], as shown in the inset of Fig. 37. The sample evidently underwent a transition from paramagnetism to ferromagnetism with decreasing temperature. The Curie temperature T_{CM} , defined as the temperature at which $d\sigma/dT$ reaches its minimum value, was determined to be 304 K. A second transition temperature T_{CP} , defined as the temperature at which $d\sigma/dT$ reaches its maximum value, can also be seen, at 55.3 K. A similar transition temperature, $T = 65$ K, was observed for a single-crystal $\text{Pr}_{0.6}\text{Sr}_{0.4}\text{MnO}_3$ sample by Rößler et al. [127].

The transition at T_{CP} can be explained using the IEO model. Below T_{CP} , the magnetic moments of the Mn cations in the B sublattice are assumed to have canted ferromagnetic coupling, and the magnetic moments of the Pr^{3+} ($4f^2$) and Pr^{2+} ($4f^3$) cations in the A sublattice are also assumed to have canted ferromagnetic coupling to each other. However, the total magnetic moment of the A sublattice should be directed opposite to the moments of the B sublattice, which reasons are as follows: (i) The spin direction of the itinerant electrons in the A sublattice must be opposite to that of the itinerant electrons in the B sublattice in the IEO model. (ii) In the B sublattice, $n_d = 4$ for Mn^{3+} , the spin direction of an itinerant electron must be parallel to the spin direction of the local 3d electrons when it hops to a Mn^{3+} cation. (iii) In the A sublattice, the number of 4f electrons n_f in Pr^{3+} ($4f^2$) and Pr^{2+} ($4f^3$) cations is less than 7, which is half of the maximum capacity of the 4f shell, the spin direction of an itinerant electron must be parallel to the spin direction of the local 4f electrons when it hops to a Pr^{3+} and Pr^{2+} cations.

The average magnetic moment per formula for $\text{Pr}_{0.6}\text{Sr}_{0.4}\text{MnO}_3$ was $3.5\mu_B$ at 10 K, which is close that reported by Boujelben et al. [128], who used neutron diffraction analysis to determine that the average moments of the Mn and Pr cations were $3.47\mu_B$ and $-0.11\mu_B$, respectively. These experimental results indicate that the magnetic moments of the Mn cations in the B sublattice are canted, as are the Pr cations in the A sublattice. Otherwise, in the absence of such canting angles, the average moment of the Mn^{3+} ($3d^4$) cations should be $4\mu_B$, and those of the Pr^{3+} ($4f^2$) and Pr^{2+} ($4f^3$) cations should be between $2\mu_B$ and $3\mu_B$. Thus, according to the above discussion, T_{CP} is the magnetic ordering temperature of the Pr cations, above which their magnetic moments become disordered. A similar result was obtained for Ti-doped (A)[B]₂O₄ spinel ferrites [87–89], as mentioned in Section 4.3.

For $\text{Pr}_{0.6}\text{Sr}_{0.4}\text{MnO}_3$, the dependence on the applied magnetic field H of the specific magnetization step $\Delta\sigma$ at T_{CP} is shown in Fig. 37 and is similar to that reported by Maheswar Repaka et al. [126], as shown the inset of Fig. 37. These observations can be explained as follows. (i) When $\mu_0 H \geq 0.5$ T, $\Delta\sigma$ increases with increasing H because the direction of the magnetic moment of the B sublattice is the same as that of H . Moreover, the angle between the Mn moments decreases with increasing H , while the magnetic moment of the B sublattice increases with increasing H , as illustrated in Fig. 38. (ii) When $\mu_0 H \geq 0.5$ T, the magnitude of $\Delta\sigma$ decreases with increasing H since the direction of the magnetic moment of the A sublattice is opposite to that of H . The angle between the Pr cation moments then increases with increasing H , and the magnetic moment

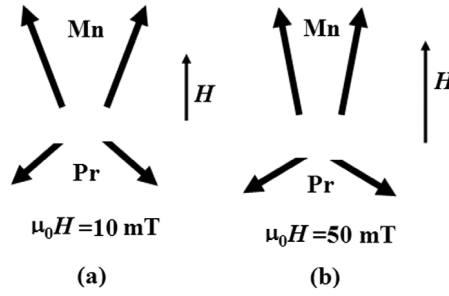


Fig. 38. Illustration of the canted magnetic structure of Mn in the B sublattice and Pr in the A sublattice in the $\text{Pr}_{0.6}\text{Sr}_{0.4}\text{MnO}_3$ sample with applied fields of (a) 10 mT and (b) 50 mT (from Ge et al. [123]).

of the A sublattice decreases with increasing H . (iii) When $\mu_0 H \geq 2.0$ T, the magnetic moments of the Pr cations become disordered, which can be understood using the IEO model. In this model, the spin direction of the itinerant electrons in the A sublattice is opposite to that of the itinerant electrons in the B sublattice, while the spin direction of the itinerant electrons in the A sublattice must be same as that of the local $4f$ electrons of the Pr^{3+} ($4f^2$) and Pr^{2+} ($4f^3$) cations when they hop to the Pr cations along the O–Pr–O–Pr–O chains. An increase in the canting angle ϕ between the Pr cations causes the itinerant electron hopping process to become more difficult. Meanwhile, the probability of forming Weiss electron pairs (see Section 8) between Pr cations decreases rapidly with increasing ϕ , causing the Pr moments to become disordered. Therefore, the measured saturation magnetizations of the samples, when H reached 2 T, were independent of the magnetic moments of the Pr cations.

5.4.2. Magnetic structure of $\text{Pr}_{0.6}\text{Sr}_{0.4}\text{Mn}_{1-x}\text{M}_x\text{O}_3$ ($M = \text{Cr}, \text{Fe}, \text{Co}, \text{or Ni}$)

According to the above analysis, all of the Mn cations at the B sites of the $\text{Pr}_{0.6}\text{Sr}_{0.4}\text{MnO}_3$ sample should be trivalent. We note, however, that the magnetic moment of a Mn^{3+} cation is $4 \mu_B$, while the average molecular magnetic moments of the $\text{Pr}_{0.6}\text{Sr}_{0.4}\text{MnO}_3$ in the different series samples [123–125] are between $3.50 \mu_B$ and $3.75 \mu_B$. Therefore, the Mn cations must assume canted ferromagnetic coupling with each other. Fig. 39(a) shows the dependences of the observed (μ_{obs} , points) and fitted (μ_{cal} , curves) molecular magnetic moments on x , for the $\text{Pr}_{0.6}\text{Sr}_{0.4}\text{M}_x\text{Mn}_{1-x}\text{O}_3$ samples ($M = \text{Cr}, \text{Fe}, \text{Co}, \text{or Ni}$). The dependence of μ_{cal} on canting angle (ϕ) was assumed to be of the form

$$\mu_{\text{cal}} = (4 - 4x + \mu_{\text{ion}}x) \times \cos \phi, \quad (5.9)$$

where μ_{ion} represents the magnetic moment of the cations. Thus, according to the IEO model, the Cr^{3+} ($3d^3$) cations are subject to canted ferromagnetic coupling with the Mn^{3+} ($3d^4$) cations, while the Fe^{3+} ($3d^5$), Co^{3+} ($3d^6$), and Ni^{3+} ($3d^7$) cations are subject to canted antiferromagnetic coupling against the Mn^{3+} ($3d^4$) cations. Therefore, $\mu_{\text{ion}} = 3, -5, -4,$ and $-3 \mu_B$ for $\text{Cr}^{3+}, \text{Fe}^{3+}, \text{Co}^{3+},$ and Ni^{3+} , respectively. The fitted curves of average canting angle, ϕ , versus x are shown in Fig. 39(b). It is worthwhile to discuss the variations observed using the IEO model.

(i) In the absence of doping, there is still a canting angle between the Mn^{3+} cations in the $\text{Pr}_{0.6}\text{Sr}_{0.4}\text{MnO}_3$ samples, due to the high repelling energy between the ferromagnetically coupled Mn^{3+} cations, and the magnetic ordering energy is too weak to arrange the magnetic moments of the Mn^{3+} cations in parallel.

(ii) When the samples were doped with Cr^{3+} cations, the Cr^{3+} ($3 \mu_B$) ions replaced the Mn^{3+} ($4 \mu_B$) ions, resulting in reduction of the magnetic repelling energy, while itinerant electrons hopping along the ion chain $\text{O}^{2-}-\text{Mn}^{3+}-\text{O}^{2-}-\text{Cr}^{3+}-\text{O}^{1-}$ could expend more energy than that they would along the ion chain $\text{O}^{2-}-\text{Mn}^{3+}-\text{O}^{2-}-\text{Mn}^{3+}-\text{O}^{1-}$. This characteristic can be understood based on Fig. 36(b): an itinerant electron has to mediate the second-highest $3d$ energy level when it transits through a Cr^{3+} ($3d^3$) cation, while it mediates the highest $3d$ energy level when it transits through a Mn^{3+} ($3d^4$) cation.

(iii) For low doping with $\text{Fe}^{3+}, \text{Co}^{3+},$ or Ni^{3+} cations, the magnetic repelling energy between the cations decreases since the Fe^{3+} (or Co^{3+} or Ni^{3+}) cations are coupled in a canted antiferromagnetic arrangement with the Mn^{3+} cations, resulting in a reduction of ϕ .

(iv) For higher doping with $\text{Fe}^{3+}, \text{Co}^{3+},$ or Ni^{3+} cations, the magnetic ordering energy is weakened, causing ϕ to increase again. This phenomenon may be understood based on Fig. 7(d). For example, an itinerant electron expends far more energy when it transits along the ion chain $\text{O}^{2-}-\text{Mn}^{3+}-\text{O}^{2-}-\text{Fe}^{3+}-\text{O}^{1-}$ than when it transits along the ion chain $\text{O}^{2-}-\text{Mn}^{3+}-\text{O}^{2-}-\text{Mn}^{3+}-\text{O}^{1-}$.

Finally, the temperature dependence of the MR value for single-crystal and polycrystalline $\text{La}_{1-x}\text{Sr}_x\text{MnO}_3$ samples can be considered, which has been reported on by Urushibara et al. [33] and Mahendiran et al. [129]. They found that the MR reaches its maximum near the Curie temperature T_C for $x = 0.15$. This phenomenon can be explained as follows: near T_C , thermal fluctuations cause the direction of the electron spin to deviate from that of the magnetic moment of the Mn cations. This deviation causes the transition probability of the itinerant electrons to decrease rapidly and increases the resistivity of the sample. Thus, an applied magnetic field can reduce the deviation of the electron spin direction and, in turn, reduce the resistivity. The MR therefore reaches its maximum value near T_C .

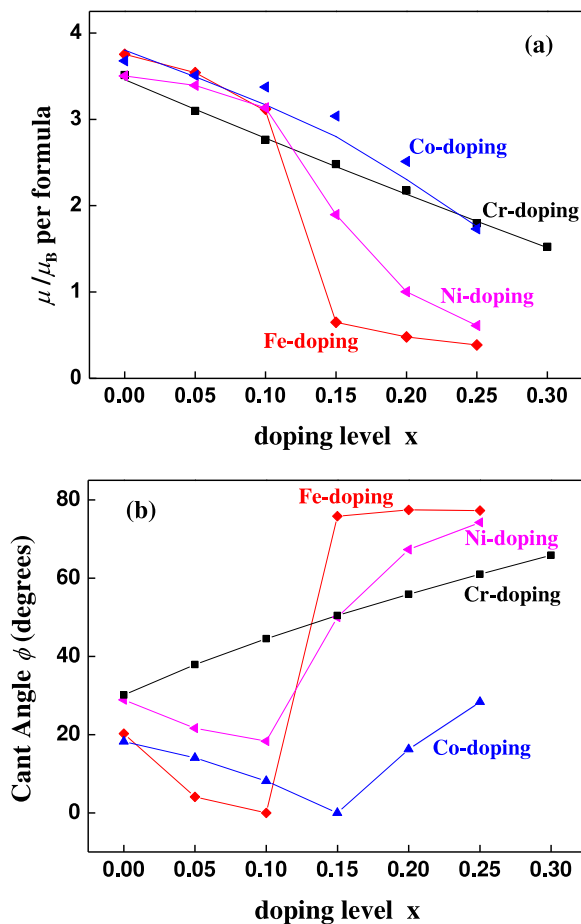


Fig. 39. (a) Dependence of the observed and fitted magnetic moments per formula, μ_{obs} (points) and μ_{cal} (curves), of $\text{Pr}_{0.6}\text{Sr}_{0.4}M_x\text{Mn}_{1-x}\text{O}_3$ ($M = \text{Cr}, \text{Fe}, \text{Co},$ or Ni) on x . (b) Dependence of the average canting angles, ϕ , between the magnetic moments of the cations on x (from Ge et al. [123,124]).

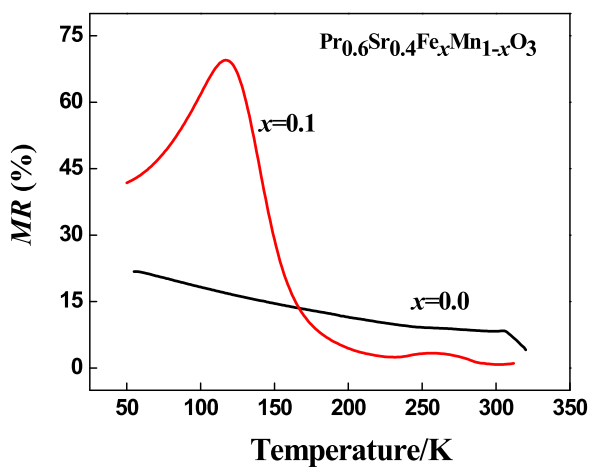


Fig. 40. Magnetoresistances of polycrystalline pellets of $\text{Pr}_{0.6}\text{Sr}_{0.4}\text{Fe}_x\text{Mn}_{1-x}\text{O}_3$ ($x = 0.0$ and 0.1) with an applied magnetic field of 2 T (from Ge et al. [124]).

In Fig. 40, an MR peak near T_{CM} is observable for the $\text{Pr}_{0.6}\text{Sr}_{0.4}\text{MnO}_3$ samples, while the MR increases with decreasing temperature. This behavior indicates that there is a finite ϕ between the Mn cation magnetic moments in the $\text{Pr}_{0.6}\text{Sr}_{0.4}\text{MnO}_3$

Table 20

Comparison of the explanations of magnetic ordering in typical oxides according to the IEO model and the SE and DE models.

Materials	Illustration of magnetic order	Explanation using IEO model	Explanation using SE and DE models
MO(M=Mn, Fe, Co, Ni)	↑↑↑↑↑↑↑↑↑↑ ↓↓↓↓↓↓↓↓↓↓	The cation magnetic moments in the (A) sites are antiparallel to those of the [B] sites. Because the spin directions of itinerant electrons are antiparallel in the two sublattices When the two magnetic sublattices have the same crystal structure, the distribution of various cations are same or close same. The total magnetic moment of the sample are always very small.	SE interaction.
MFe ₂ O ₄ (M=Fe, Co, Ni, Cu)	↑↑↑↑↑ ↓↓↓↓↓↓↓↓↓↓	3d electron number, $n_{3d} \geq 5$, of all cations. All cation magnetic moments in the (A) or the [B] sites are parallel at low temperature, and the cation magnetic moments in the (A) sites are antiparallel to those of the [B] sites. Because the spin directions of itinerant electrons are antiparallel each other in the two sublattices. The two magnetic sublattices have the different crystal structure, resulting in a larger total magnetic moment.	1. SE interaction, the cation magnetic moment are parallel when cation-O-cation bond angle, θ , is close to 90°, while the cation magnetic moment are antiparallel when $\theta > 120^\circ$. 2. The cation magnetic moment are parallel in [B] sublattice due to DE interaction. The cation magnetic moments in the (A) sublattice are antiparallel to [B] sublattice due to SE interaction.
MFe ₂ O ₄ (M=Ti, Cr)	↑↑↓↑↑ ↓↓↑↓↓↓↑	The magnetic moments ($n_{3d} \leq 4$) of Ti and Cr cations are antiparallel to those ($n_{3d} \geq 5$) of Fe cations in each sublattices.	There is no satisfactory explanation to be found.
MnFe ₂ O ₄	↑↑↓↑↑ ↓↓↑↓↓↓↑	The magnetic moments ($n_{3d} = 4$) of Mn ³⁺ cations are antiparallel to those ($n_{3d} \geq 5$) of Mn ²⁺ and Fe cations in each sublattices.	There is no satisfactory explanation to be found.
LaMnO ₃	↓↑↓↑↓↑↓↑↓	There is only one magnetic sublattice, the magnetic moments of Mn ³⁺ (3d ⁴) cations are antiparallel to those of Mn ²⁺ (3d ⁵) cations.	SE interaction between Mn ³⁺ cations.
La _{0.85} Sr _{0.15} MnO ₃	↑↑↑↑↑↑↑↑↑↑	There is only one magnetic sublattice, all of Mn ³⁺ (3d ⁴) cation magnetic moments are parallel each other. No Mn ⁴⁺ cations.	DE interaction between Mn ³⁺ and Mn ⁴⁺ cations.
La _{0.6} Sr _{0.4} MnO ₃		The magnetic moments of Mn ³⁺ (3d ⁴) are canted ferromagnetic coupling each other.	DE interaction between Mn ³⁺ and Mn ⁴⁺ cations.
La _{0.8} Sr _{0.2} Mn _{0.9} Fe _{0.1} O ₃	↑↑↑↑↓↑↑↑↑	The magnetic moments of Fe ³⁺ (3d ⁵) are antiparallel to those of Mn ³⁺ (3d ⁴)	SE interaction between Fe ³⁺ and Mn ³⁺ .
La _{0.8} Sr _{0.2} Mn _{0.9} Cr _{0.1} O ₃		The magnetic moments of Cr ³⁺ (3d ³) are canted ferromagnetic coupling with those of Mn ³⁺ (3d ⁴)	DE interaction between Cr ³⁺ and Mn ³⁺

samples at low temperatures. For Pr_{0.6}Sr_{0.4}Fe_{0.1}Mn_{0.9}O₃, it is interesting to see that there is a clear MR peak at 117 K, which is close to its T_C (129 K). Both above and below 117 K, the MR decreases rapidly. This phenomenon is similar to that observed in La_{0.85}Sr_{0.15}MnO₃ [33] and indicates that the ϕ decreases to near zero.

6. Comparison of the IEO model to the super-exchange (SE) and double-exchange (DE) models of magnetic ordering in oxides

Based on the above discussion, the IEO model presented in Sections 3–5 can be compared to the traditional SE and DE interaction models, and how each model explains the magnetic ordering in oxides can be addressed, as shown in Table 20.

Table 21

Observed values of the average atomic magnetic moment, μ_{obs} , Curie temperature, T_{C} , and electrical resistivity, ρ , for several metals, and the total number, n_{ds} , of their 3d and 4s electrons, 3d electron number, $n_{\text{d}} = 10 - \mu_{\text{obs}}$, and their free electron number, $n_{\text{f}} = n_{\text{ds}} - n_{\text{d}}$ (from Qi et al. [131]).

	μ_{obs} (μ_{B})	T_{C} (K)	$\rho(0^{\circ}\text{C})$ ($10^{-6} \Omega \text{ cm}$)	n_{ds}	n_{d}	n_{f}
Fe	2.22	1043	8.6	8	7.78	0.22
Ni	0.62	631	6.14	10	9.38	0.62
Co	1.72	1404	5.57	9	8.28	0.72
Cu	0.00	–	1.55	11	10	1.00
Ref.	[6,35]	[34]	[34]	–	–	–

7. New itinerant electron model for magnetic metals (IEM model)

Experimental values for the electrical resistivities ρ , average atomic magnetic moments μ_{obs} , and Curie temperature T_{C} for Fe, Ni, and Co can easily be found in the literature [1–3,34,35] and are provided in Table 21. Conventionally, the free electron theory of metals is used to explain the electrical transport properties of metals, and the solid energy band theory is used to explain their magnetic properties. However, there has been no quantitative explanation so far of the relation between the average magnetic moments per atom and the resistivities of Fe, Ni, and Co.

Kister et al. [73] and Sánchez-Barriga [130] reported on the spin-and-angle-resolved photoemission spectra of Fe and Co, and a review of their results was conducted by Johnson [74]. They found that the energies of the valence electrons of metals are distributed around 6 eV, while those of the spin-down electrons (minority spin) are distributed near the Fermi level, as shown in Fig. 8. In actual practice, only electrons with energies ~ 0.03 eV below the Fermi level can be thermally excited to above the Fermi level at room temperature. Thus, only a few valence electrons can be considered to be free electrons for electrical transport. According to the free electron theory of metals, there is only one free electron per atom on average in Cu that contributes to the electrical conduction. Since the electrical resistivities of Fe, Ni, and Co are higher than that of Cu, the average numbers of free electrons per atom in these metals should be less than that in Cu.

Based on these observations and analyses, Qi *et al.* [131] proposed the IEM model, which is based on the following assertions.

(i) In the process of forming a polycrystalline metal from free atoms, most of the 4s electrons in Fe, Ni, and Co enter the 3d orbits subjected to the Pauli repulsive force, while the remaining 4s electrons form free electrons. This assertion closely agrees with the experimental results obtained from XAS and X-ray magnetic circular dichroism [132], as well as γ -ray diffraction [133], they found a phenomenon to transfer of one electron from the 4s to the 3d state in the metal Fe samples.

(ii) Since the average number of 3d electrons, n_{d} , is not an integer, some atoms have one more 3d electron than the other atoms. These excess 3d electrons have a certain probability of itinerating between the 3d orbits of the adjacent atoms and form itinerant electrons. The other 3d electrons are local electrons.

(iii) The transition probability of itinerant electrons is very low, so the contribution to the overall resistivity from itinerant electrons is far lower than that from free electrons. Consequently, the resistivity of a metal decreases as the number of free electrons increases.

According to the IEM model, and using the observed average atomic magnetic moments values of Fe, Ni, and Co (2.22, 0.62, and $1.72\mu_{\text{B}}$, respectively), the average number of free electrons can be calculated. Since there are five energy levels in the 3d sub-shell of a 3d transition metal, when $n_{\text{d}} \leq 5$, every spin-up electron occupies one energy level from the lowest to the highest energy level. These electrons are called majority spin electrons, and the atomic magnetic moment μ_{at} is then $n_{\text{d}}\mu_{\text{B}}$ (neglecting the orbital magnetic moment). When $n_{\text{d}} \geq 6$, the excess spin-down electrons fill the energy levels from the highest to the lowest energy level [73,130]. These electrons are called minority spin electrons. When all five energy levels are fully occupied by 10 electrons, the atomic magnetic moment is equal to zero (as in Cu), since there are two electrons with opposite spins per energy level. Only energy levels containing only one electron yield a spin that contributes to the atomic magnetic moment, μ_{at} . Therefore, μ_{at} can be written as

$$\mu_{\text{at}} = (10 - n_{\text{d}})\mu_{\text{B}}, \quad \text{when } (6 \leq n_{\text{d}} \leq 10). \quad (7.1)$$

This relation indicates that the n_{d} of Fe, Ni, and Co metals can be calculated using their experimental values of μ_{at} , which are 2.22, 0.62, and $1.7\mu_{\text{B}}$, respectively. Thus, $n_{\text{d}} = 7.78, 9.38,$ and 8.28 for Fe, Ni, and Co, respectively.

Furthermore, the average number of free electrons per atom can be obtained as

$$n_{\text{f}} = n_{\text{ds}} - n_{\text{d}}. \quad (7.2)$$

Here, $n_{\text{ds}} = 8, 10,$ and 9 are the total numbers of 3d and 4s electrons and $n_{\text{f}} = 0.22, 0.62,$ and 0.72 for Fe, Ni, and Co, respectively. As shown in Table 21 and Fig. 41, a very interesting result was found: the electrical resistivities of Fe, Ni, Co, and Cu all decrease with increasing n_{f} .

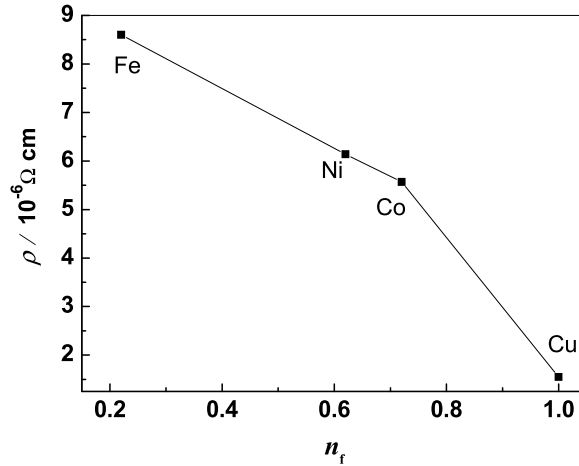


Fig. 41. Dependence of the electrical resistivity (ρ) on the average free electron number (n_f) per atom for Fe, Ni, Co, and Cu (from Qi et al. [131]).

Table 22

Divalent and trivalent effective radii, r_{eff}^{2+} and r_{eff}^{3+} (from Shannon [76]) and their difference $r_{\text{eff}}^{2+} - r_{\text{eff}}^{3+}$ for several cations with coordination numbers of 6.

Element	r_{eff}^{2+} (Å)	r_{eff}^{3+} (Å)	$r_{\text{eff}}^{2+} - r_{\text{eff}}^{3+}$ (Å)
Cr	0.80	0.615	0.185
Mn	0.83	0.645	0.185
Fe	0.78	0.645	0.135
Co	0.745	0.61	0.135
Ni	0.69	0.6	0.09
Ag	0.94	0.75	0.19

Note: Effective radius of O^{2-} with coordination number 6 is 1.40 Å.

An important difference between the IEM proposed by Qi *et al* [131] and the model proposed by Stearns [134,135] is that Stearns could only explain the magnetic properties of the metals, but not the relation between the magnetic moment and the electrical resistivity of a metal.

8. Weiss electron pair (WEP) model and magnetic ordering energy

To determine the relation between the IEO and IEM models, it is necessary to investigate the origin of the magnetic ordering energy. As mentioned in Section 1.2.4 and Table 3, the Curie temperature values of spinel ferrites are close to that of Ni, which suggests that there is an intrinsic relation between the magnetism of oxides and metals. This intrinsic relation should be related to the magnetic ordering energy; however, no phenomenological model for the magnetic ordering energy based on atomic physics has been found so far.

8.1. WEP model

In this model, the itinerant electrons in magnetic metals and oxides are considered to have similar itinerant characteristics, according to the IEO model (cf. Section 3) and IEM model (cf. Section 7), while the free electrons in metals are distinguished from the itinerant electrons. An itinerant electron in an oxide then transits between the outer orbits of neighboring anions and cations, since an electron at an O^{2-} anion has a probability of transiting to its adjacent O^{1-} anion in a hopping process that is mediated by the cation in the IEO model. Meanwhile, in a magnetic metal, an itinerant electron has a probability of transiting between the outer 3d orbits of the adjacent metal ions (excluding the free electrons). In short, the transition of an itinerant electron is by a step of an atom in the crystal lattice. This view is in accordance with that of effective ionic radius proposed by Shannon [76].

Based on many experimental results, Shannon gave the effective radii, r_{eff} , of all ions. There are distinct differences in the r_{eff} of an element with different valences in a compound. Table 22 shows the effective radii of several divalent and trivalent cations with a coordination number 6, r_{eff}^{2+} and r_{eff}^{3+} , respectively. It can be seen from Table 22 that the difference, $r_{\text{eff}}^{2+} - r_{\text{eff}}^{3+}$, is between 0.09 Å and 0.19 Å, which suggests that one electron in the outer orbit of an ion moves in a spherical shell with a thickness of about 0.1–0.2 Å.

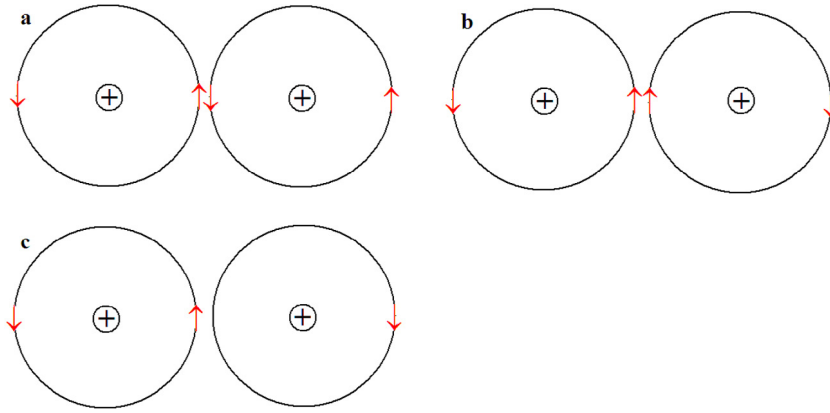


Fig. 42. Illustrations of (a) a WEP and (b) and (c) itinerant electrons in the outer orbits of adjacent ions (from Qi et al. [136]).

Table 23

Curie temperature, T_C , average molecular magnetic moment μ_{obs} , saturation magnetization, M_S , and the molecular field intensity, H_m , of $\text{La}_{0.8}\text{Ca}_{0.2}\text{MnO}_3$, $\text{La}_{0.75}\text{Ca}_{0.25}\text{MnO}_3$, $\text{La}_{0.70}\text{Sr}_{0.30}\text{MnO}_3$, and Fe. Here, Z is the molecule number per crystal cell, v is the volume of the crystal cell, w is the Weiss molecular field energy density, w_0 is the average energy of Weiss molecular field per pair of magnetic ions, and $k_B T_C$ is the thermal energy at T_C (from Qi et al. [136]).

Materials	T_C (K)	μ_{obs} (μ_B)	M_S (emu/cm ³)	H_m (10^5 Oe)	Z	v (\AA^3)	w (10^8 erg/cm ³)	w_0 (eV)	$w_0/k_B T_C$
Ca0.20	198	3.76	603.01	7.84	4	232.633 _{15K}	4.728	0.0344	2.01
Ca0.25	240	3.13	506.37	11.41	4	231.215 _{23K}	5.778	0.0417	2.01
Sr0.30	369	3.50	560.98	15.70	6	349.767 _{15K}	8.807	0.0641	2.02
Fe	1043	2.22	1740.0	69.94	2	23.394 _{293K}	121.7	0.1777	1.97

Taking these investigations into account, Qi et al. [136] recently proposed a model for the origin of the magnetic ordering energy. Assuming that a moving electron in an outer orbit of an ion has a constant spin direction, the electrons in the orbits of the adjacent ions, including the cations and anions in a compound and the ions (atoms that have lost free electrons) in metals, may have three states, as shown in Fig. 42. When the electrons have the state depicted in Fig. 42(a), the two neighboring electrons cannot be exchanged because they have opposite spin directions. The magnetic ordering energy is thus given by the difference between the static magnetic attractive energy and the Pauli repulsive energy of the two electrons. This type of electron pair, which has a particular lifetime and probability of appearing, have been called a WEP [136].

When the two electrons have the state illustrated in Fig. 42(b), there is both static magnetic and Pauli repulsive energy between the two neighboring electrons, while they can be exchanged easily since they both have the same spin direction. In the third case, when the electrons have the state shown in Fig. 42(c), it is easy for the middle electron to transit to the orbit of the right ion. Thus, both the electron exchange of Fig. 42(b) and electron transit of Fig. 42(c) may be considered to be simply transitions of itinerant electrons, in which the spin directions of the itinerant electrons cannot change. In other words, such transitions cannot occur if the two neighboring electrons have opposite spin directions. Thus, in the WEP model, it is easy to understand why an itinerant electron has a constant spin direction in the itinerating process, which is a feature that has not been explained until now, even though the itinerant electron concept has been used for many years [22–24].

8.2. Estimation of the energies of the Weiss molecular fields for several materials

As was mentioned in Section 1.1, and following both Chen [2] and Dai and Qian [6], the molecular field intensity for Fe with $T_C = 1043$ K and $gS\mu_B = 2.22\mu_B$ can be calculated easily, yielding $H_m = 6.994 \times 10^6$ Oe. H_m values were estimated similarly for the perovskite manganites $\text{La}_{0.8}\text{Ca}_{0.2}\text{MnO}_3$, $\text{La}_{0.75}\text{Ca}_{0.25}\text{MnO}_3$, and $\text{La}_{0.70}\text{Sr}_{0.30}\text{MnO}_3$, with the corresponding magnitudes listed in Table 23. Taking these values of H_m and their associated saturation magnetizations M_S , the molecular field energy density w can be calculated for these materials. For example, in Fe with $M_S = 1740$ Gs, we have

$$w = H_m M_S = 6.994 \times 10^6 \times 1740 = 1.217 \times 10^{10} \text{ erg/cm}^3. \quad (8.1)$$

Using this energy density, the average molecular field energy per magnetic ion pair w_0 can be calculated. Since $a = 2.86$ \AA for a cubic cell of Fe, there are two Fe atoms per cubic cell, we have

$$w_0 = wa^3 = 1.217 \times 10^{10} \times (2.86 \times 10^{-8})^3 = 2.847 \times 10^{-13} \text{ erg} = 0.1777 \text{ eV}. \quad (8.2)$$

This value is quite reasonable to compare with an average cohesive energy per pair of ions of ~ 10 eV [95]. The calculated values of w and w_0 for the perovskite manganites $\text{La}_{0.8}\text{Ca}_{0.2}\text{MnO}_3$, $\text{La}_{0.75}\text{Ca}_{0.25}\text{MnO}_3$, and $\text{La}_{0.70}\text{Sr}_{0.30}\text{MnO}_3$ are also listed in

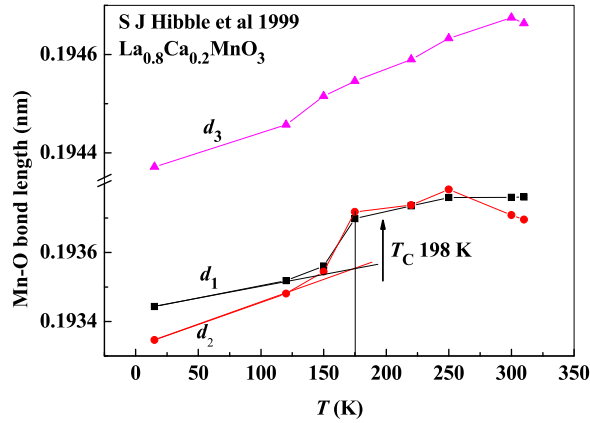


Fig. 43. Dependences of the distances between Mn and O ions, d_1 , d_2 , d_3 , on the test temperature T for an orthorhombic $\text{La}_{0.8}\text{Ca}_{0.2}\text{MnO}_3$ sample (from Qi et al. [136]).

Table 24

Probability of forming WEPs, D , and the relative parameters of $\text{La}_{0.8}\text{Ca}_{0.2}\text{MnO}_3$, $\text{La}_{0.75}\text{Ca}_{0.25}\text{MnO}_3$, and $\text{La}_{0.70}\text{Sr}_{0.30}\text{MnO}_3$ samples. Here, Δd_{obs} is the non-linear variation amplitude of the Mn–O bond length near T_c , and r_{e0} and r_{em} are the equilibrium and maximum distances, respectively, between electrons in a WEP (from Qi et al. [136]).

Sample	T_c (K)	Mn–O bond	Δd_{obs} (Å)	r_{e0} (Å)	r_{em} (Å)	D (%)
$\text{La}_{0.8}\text{Ca}_{0.2}\text{MnO}_3$	198	d_1	0.00147	0.00889	0.01036	0.045
		d_2	0.00167	0.0101	0.01177	0.066
$\text{La}_{0.75}\text{Ca}_{0.25}\text{MnO}_3$	240	d_1	0.00261	0.01586	0.01848	0.308
		d_2	0.00236	0.01436	0.01673	0.228
$\text{La}_{0.70}\text{Sr}_{0.30}\text{MnO}_3$	369	d_1	0.00490	0.02970	0.03460	3.130

Table 23. Notably, the different crystal structures of these materials must be accounted for in these calculations. Since there are four molecules per crystal cell in orthorhombic $\text{La}_{0.8}\text{Ca}_{0.2}\text{MnO}_3$ and $\text{La}_{0.75}\text{Ca}_{0.25}\text{MnO}_3$, $w_0 = wv/2$ in those cases, and since there are six molecules per crystal cell in rhombohedral $\text{La}_{0.70}\text{Sr}_{0.30}\text{MnO}_3$, $w_0 = wv/3$, where v is the cell volume. An interesting result is found in **Table 23**: w_0 is two times the thermal energy $k_B T_c$ at T_c for the four materials with different crystal structures.

The energy, w_0 , reflects the static attractive energy of the WEPs generating the force that acts to compress the crystal cell volume. Accordingly, this energy will decrease rapidly when the sample temperature is near T_c , where corresponding increases in thermal expansivity.

8.3. Thermal expansivity near the Curie temperature

Hibble et al. [36] investigated the dependence of crystal lattice constants on test temperature for the orthorhombic perovskite manganite $\text{La}_{0.8}\text{Ca}_{0.2}\text{MnO}_3$. The obtained temperature dependence of the Mn–O bond lengths, d_1 , d_2 , and d_3 , along the three orthorhombic directions are as shown in **Fig. 43**. It can be seen that both d_1 and d_2 experience rapid increases near the Curie temperature T_c , while d_3 varies more slowly than both d_1 and d_2 . These results suggest that the static magnetic attractive forces of WEPs are along the d_1 and d_2 directions and generate a force that acts to compress the Mn–O bond length.

Near T_c , the static magnetic attractive forces due to WEPs decrease rapidly, resulting in a rapid decrease in the magnetic ordering energy and a simultaneous rapid increase in the Mn–O bond length. One can define two tangent lines along the curves in the low temperature region, as shown in **Fig. 43**, which allows us to consider that only the nonlinear variations in Mn–O bond lengths near T_c are related to the magnetic ordering energy. With this method, the nonlinear variations Δd_{obs} corresponding to the changes in d_1 and d_2 were found to be 0.00147 Å and 0.00167 Å, respectively. Similar studies were conducted by Radaelli et al. [37], who investigated the dependence of crystal lattice constants on test temperature for the orthorhombic perovskite manganite $\text{La}_{0.75}\text{Ca}_{0.25}\text{MnO}_3$, and by Hibble et al. [36], who also investigated the same temperature dependence for the rhombohedral perovskite manganite $\text{La}_{0.7}\text{Sr}_{0.3}\text{MnO}_3$, for which $d_1 = d_2$. The results of these two investigations and the values of Δd_{obs} obtained are presented in **Table 24** and **Figs. 44** and **45**.

8.4. Discussion of the relation between the WEP and Weiss molecular field energies

It is very interesting to consider the relation between the WEP and Weiss molecular field energies. If one assumes that D represents the probability of forming a WEP (cf. **Fig. 42(a)**), r_e represents the distance between the two electrons, and each

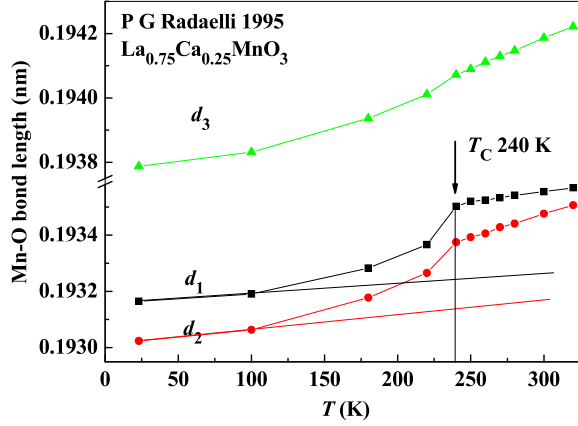


Fig. 44. Dependences of the distances between Mn and O ions, d_1 , d_2 , d_3 , on the test temperature T for an orthorhombic $\text{La}_{0.75}\text{Ca}_{0.25}\text{MnO}_3$ sample (from Qi et al. [136]).

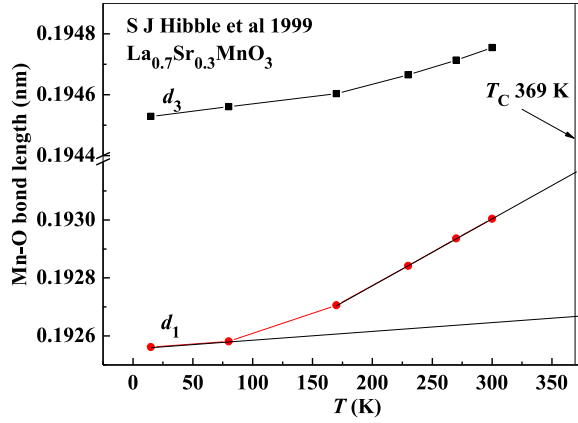


Fig. 45. Dependences of the distances between Mn and O ions, d_1 and d_3 , on the test temperature T for a rhombohedral $\text{La}_{0.7}\text{Sr}_{0.3}\text{MnO}_3$ sample (from Qi et al. [136]).

electron has an electric charge of $-e$ and a spin of $1\mu_B$, then, in addition to the ionic cohesive energy, the system experiences an average increase in energy given by

$$\Delta u = \frac{C}{r_e^9} - D \times \frac{(1\mu_B)^2}{4\pi\mu_0 r_e^3}. \quad (8.3)$$

Here, the first item represents the Pauli repulsive energy and the second item represents the magnetic attractive energy between the two electrons with opposite spin directions. When the two electrons are in the equilibrium state (at which $r_e = r_{e0}$), the derivative with respect to the distance between the electrons, $\left. \frac{d\Delta u}{dr_e} \right|_{r_e=r_{e0}} = 0$, yielding

$$0 = -\frac{9C}{r_{e0}^{10}} + D \times \frac{3(1\mu_B)^2}{4\pi\mu_0 r_{e0}^4}. \quad (8.4)$$

From this condition, we can determine the value of C ,

$$C = \frac{3D(1\mu_B)^2 r_{e0}^6}{36\pi\mu_0}, \quad (8.5)$$

and substituting Eq. (8.5) back into Eq. (8.3) yields

$$\Delta u = \frac{D(1\mu_B)^2}{4\pi\mu_0} \left(\frac{r_{e0}^6}{3r_e^9} - \frac{1}{r_e^3} \right) \quad (8.6)$$

or

$$\Delta u = 53.65 \left(\frac{r_{e0}^6}{3r_e^9} - \frac{1}{r_e^3} \right) D. \quad (8.7)$$

Here, the energy and length are measured in units of electronvolts and picometers.

Moreover, when $r_e = r_{e0}$, we have that

$$\Delta u_0 = -\frac{2}{3} \times \frac{53.65D}{r_{e0}^3} \quad (8.8)$$

and

$$r_{e0}^3 = \frac{35.77D}{|\Delta u_0|}. \quad (8.9)$$

The maximum distance between the two electrons, r_{em} , may also be calculated and was determined to be

$$r_{em} = 1.165r_{e0}. \quad (8.10)$$

When $r_e > r_{em}$, the WEP will be broken, causing the molecular field to disappear. This behavior can be described by considering the bond length deviation,

$$\Delta d_{obs} = r_{em} - r_{e0}. \quad (8.11)$$

Here, Δd_{obs} is the nonlinear thermal expansive length, and its values for $\text{La}_{0.8}\text{Ca}_{0.2}\text{MnO}_3$, $\text{La}_{0.75}\text{Ca}_{0.25}\text{MnO}_3$, and $\text{La}_{0.70}\text{Sr}_{0.30}\text{MnO}_3$ are listed in Table 24. Assuming then that $|\Delta u_0|$ in Eq. (8.9) equals the w_0 values in Table 23, r_{e0} , r_{em} , and D can be determined using Eqs. (8.9)–(8.11) and are as listed in Table 24.

From Table 24, one may see that magnetic ordering arises in the perovskite manganites $\text{La}_{0.8}\text{Ca}_{0.2}\text{MnO}_3$, $\text{La}_{0.75}\text{Ca}_{0.25}\text{MnO}_3$, and $\text{La}_{0.70}\text{Sr}_{0.30}\text{MnO}_3$ when the probability D of WEP formation (cf. Fig. 42(a)) reaches 0.066%, 0.228%, and 3.13%, respectively. In addition, r_{em} for the two electrons constituting a WEP is less than 0.035 Å, which is distinctly smaller than the electron hopping range (0.09 Å, see Table 22) along the ionic radius direction in the outer electron orbit of the ion. These results are quite reasonable and indicate that the WEP model is capable of explaining the magnetic ordering of the materials.

An additional point to note from Table 24 is that the largest value of D is approximately 50 times more than its smallest value, which suggests that there are other factors affecting the magnetic ordering energy. One of these factors is the repulsive energy between spins with the same spin direction, as shown in Fig. 42(b). A second factor is the energy level of the outer orbit electron. As mentioned in Section 4.5, the spinel ferrites $M\text{Fe}_2\text{O}_4$ with $(A)[B]_2\text{O}_4$ structures experience a rapid decrease in T_C when the Fe content is less than 2.0 per formula. Similarly, the perovskite manganites $R_{0.7}T_{0.3}\text{MnO}_3$ ($R = \text{La, Pr, Nd, } \dots$, and $T = \text{Sr, Ba, Ca, } \dots$) also exhibit rapid decreases in T_C when Mn is replaced by any element, as mentioned in Sections 5.3 and 5.4. According to the IEO model, many Fe cations in $M\text{Fe}_2\text{O}_4$ are trivalent and have five 3d electrons, so the itinerant electrons (with spin down) move along the highest 3d energy level of the 3d sub-shell, as shown in Fig. 19. Similarly, for $R_{0.7}T_{0.3}\text{MnO}_3$, the Mn cations are trivalent and have four 3d electrons, so the itinerant electrons (with spin up) also move along the highest 3d energy level of the 3d sub-shell. These facts regarding the T_C variation suggest that if itinerant electrons in an magnetic oxide have to pass through the lower 3d energy level, as is the case if the cations have less than four (or more than five) 3d electrons, the magnetic ordering energy of this oxide will be lower than that of the case when itinerant electrons pass through the highest 3d energy level.

It is clear that further studies of the magnetic ordering energy should be conducted to test this model against the experimental data more thoroughly.

8.5. Why do typical magnetic metals and oxides have different Curie temperatures?

The WEP model can also explain why typical magnetic metals and oxides have different Curie temperatures [137], e.g., $T_C = 1404, 1043, \text{ and } 631 \text{ K}$ for Co, Fe, and Ni, respectively, while $T_C = 860 \text{ K}$ and 369 K for the spinel ferrite Fe_3O_4 and perovskite manganite $\text{La}_{0.7}\text{Sr}_{0.3}\text{MnO}_3$, respectively. Until now, no satisfactory phenomenological explanation for this magnetic ordering puzzle has been found, despite 100 years of research since Weiss originally proposed using a molecular field to explain magnetic ordering in 1907.

As is well known, the magnetic metal Co, which has $T_C = 1404 \text{ K}$, has a hexagonal close-packed crystal structure in which each ion (excluding the free electrons) has 12 nearest adjacent ions. In other words, the average number of bonds surrounding an ion capable of forming WEPs, N_{WEP} , is 12. For the body-centered-cubic magnetic metal Fe, a similar calculation yields $N_{\text{WEP}} = 8$. As a result, the T_C of Fe (1043 K) is lower than that of Co.

The magnetic metal Ni has an FCC crystal structure with each ion having 12 nearest neighbors. According to the IEM model [131], the average number of the 3d electrons, n_d , in Ni is 9.38 (cf. Section 7 and Table 21). In other words, 38% of Ni ions have full 3d sub-shells filled by 10 electrons, and consequently these ions cannot form WEPs with their adjacent ions, as being similar to metal Cu. Therefore, only 62% of Ni ions can form WEPs with 62% of their nearest adjacent ions, yielding $N_{\text{WEP}} = 4.61 (= 12 \times 0.62 \times 0.62)$.

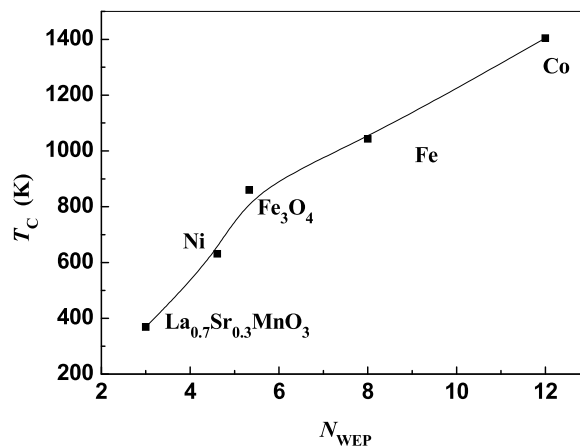


Fig. 46. Dependence of the Curie temperature T_C on the average number of chemical bonds capable of forming WEPs, N_{WEP} , near a cation (cf. Qi et al. [137]).

For the (A)[B]₂O₄ spinel ferrite Fe₃O₄, a cation has four (or six) nearest adjacent O anions in the (A) (or [B]) site, and there are eight (A) sites and 16 [B] sites per crystal cell, yielding $N_{\text{WEP}} = 5.33 [(4 \times 8 + 6 \times 16)/24]$. A similar calculation can be performed for the ABO₃ perovskite manganite La_{0.7}Sr_{0.3}MnO₃, where there are two cations per equivalent cubic crystal cell, while WEPs can only be formed at the six Mn–O bonds, yielding $N_{\text{WEP}} = 3$. These results are shown in Fig. 46, from which one may see that T_C decreases with decreasing N_{WEP} . This relationship indicates that the assumption that the magnetic ordering energy originates from WEPs is reasonable. This view is very important in the search for new magnetic materials with high T_C .

According to this view of the origin of magnetic ordering energy, we can explain why the magnetizations of typical bulk magnetic materials decrease very slowly when T is far lower than T_C and rapidly when T is close to T_C . When $T \ll T_C$, the thermal energy density is far lower than the magnetic ordering energy density, so it can only cause the distance between ions to expand but cannot cause the distance between the electrons in the WEPs to increase significantly. When T is close to T_C , the thermal energy density is close to the magnetic ordering energy density, and the distance between the electrons in the WEPs increases rapidly, resulting in a rapid decrease in the probability of WEP formation and a rapid decrease in the magnetic ordering energy, hence resulting in a rapid decrease in the magnetization.

9. Summary and prospects for future work

A series of magnetic ordering rules for magnetic oxides and metals was proposed by Tang's group, which include the IEO model for magnetic oxides, the new IEM model for magnetic metals, and the WEP model for the origin of magnetic ordering energy. These new phenomenological models are based on atomic physics and are easier to understand than the conventional exchange interactions models. By applying these new models to suitable materials, the magnetic ordering for antiferromagnetic MO ($M = \text{Mn, Fe, Co, or Ni}$) oxides, ferrimagnetic (A)[B]₂O₄ spinel ferrites $M\text{Fe}_2\text{O}_4$ ($M = \text{Ti, Cr, Mn, Fe, Co, Ni, or Cu}$), ABO₃ perovskite manganites $R_{1-x}T_x\text{Mn}_{1-y}M_y\text{O}_3$ ($M = \text{Ti, Cr, Mn, Fe, ...}$), and Fe, Co, and Ni metals have been explained successfully. These results account for experimental phenomena that include not only those that have been explained using conventional models, but also those that have not been explained using conventional models for many years. The greater success of these new models compared to the conventional models indicates that the traditional models should be improved by the newer models reviewed here.

Based on these new models, many magnetic ordering experimental phenomena can and should be investigated further. Some examples are as follows.

(i) For the (A)[B]₂O₄ spinel ferrites $M_x\text{Fe}_{2-x}\text{O}_4$, a magnetic ordering energy explanation for the decreases in the magnetic moments and Curie temperatures when the Fe content is less than 2.0 should be found.

(ii) For the ABO₃ perovskite manganites $R_{1-x}T_x\text{Mn}_{1-y}M_y\text{O}_3$ ($M = \text{Ti, Cr, Mn, Fe, ...}$), an explanation of how the magnetic ordering energy changes with the T or M contents should be identified.

(iii) For ferromagnetic and antiferromagnetic alloys, it is necessary to consider in detail how the atomic magnetic moments are coupled.

(iv) How the magnetic ordering energy changes with the test temperature should be ascertained.

(v) The magnetic properties of hard magnetic materials should be investigated using the IEO, IEM, and WEP models.

(vi) Fe₃O₄ undergoes a Verwey transition at low temperature [138,139], and the magnetic moment of the sample below the transition temperature is distinctly lower than that at the transition temperature. It should be investigated why the Verwey transition of Fe₃O₄ affects the magnetic ordering, using the IEO and WEP models.

(vii) The magnetic properties of some nitrides have been reported [140,141]. These magnetic properties may have physical mechanisms similar to that of magnetic oxides, because the valence electronic structure of $N^{3-}(2s^2 2p^6)$ is close to that of $O^{2-}(2s^2 2p^6)$, which should be investigated using the IEO model.

(viii) The magnetic properties of nanosolids are different from those of bulk solids [142–144] due to the existence of surface effects, which should be investigated using the IEO, IEM, and WEP models.

Acknowledgments

This work was supported by the National Natural Science Foundation of China (NSF-11174069 and NSF-10074013), the Natural Science Foundation of Hebei Province, China (A2015205111), the Key Item Science Foundation of Hebei Province, China (16961106D), and the Young Scholar Science Foundation of the Education Department of Hebei Province, China (QN2016015). The authors wish to thank Profs. Y. W. Du, Wei Zhong, J. F. Hu, J. B. Yang, Wu-Ming Liu, Deng-Lu Hou, Ying Liu, Wei Chen and Norm Davison, for their helpful discussion and Drs. Li-Hu Liu, Xu Zhao, Shao-Peng Liu, Deng-Hui Ji, Jing Xu, Shi-Qiang Li, Xing-Min Liu, Yan-Feng Li, Zhi-Feng Shang, and Li-Li Lang and all of the graduate students in Prof. Tang's group for their hard work in these investigations.

References

- [1] J.M.D. Coey, *Magnetism and Magnetic Materials*, Cambridge University Press, Cambridge, 2010.
- [2] C.W. Chen, *Magnetism and Metallurgy of Soft Magnetic Materials*, North-Holland Publishing Company, Amsterdam, 1977.
- [3] S. Chikazumi, *Physics of Ferromagnetism*, second ed, Oxford University Press, London, 1997.
- [4] B.S. Han, X.F. Nie, G.D. Tang, W. Xi, Formation of hard bubbles by single-pulse bias field (in Chinese with English abstract), *Acta Phys. Sin.* 34 (1985) 1396–1406.
- [5] X.F. Nie, G.D. Tang, X.D. Niu, B.S. Han, Classification of hard domains in garnet bubble films, *J. Magn. Magn. Mater.* 95 (1991) 231–236.
- [6] D.S. Dai, K.M. Qian, *Ferromagnetism* (in Chinese), Science Press, Beijing, 1987.
- [7] J.X. Fang, L. Dong, *Solid State Physics* (in Chinese), Shanghai Scientific and Technical Publishers, Shanghai, 1981.
- [8] R.J. McQueeney, M. Yethiraj, S. Chang, W. Montfrooij, T.G. Perring, J.M. Honig, P. Metcalf, Zener double exchange from local valence fluctuations in magnetite, *Phys. Rev. Lett.* 99 (2007) 246401.
- [9] J.A. Moyer, C.A.F. Vaz, D.A. Arena, D. Kumah, E. Negusse, V.E. Henrich, Magnetic structure of Fe-doped $CoFe_2O_4$ probed by x-ray magnetic spectroscopies, *Phys. Rev. B* 84 (2011) 054447.
- [10] L.J. Zhao, W. Xu, H. Yang, L.X. Yu, Effect of Nd ion on the magnetic properties of Ni–Mn ferrite nanocrystal, *Curr. Appl. Phys.* 8 (2008) 36–41.
- [11] Y.H. Li, T. Kouh, I.B. Shim, C.S. Kim, Investigation of cation distribution in single crystalline $Fe_{3-x}Mn_xO_4$ microspheres based on Mössbauer spectroscopy, *J. Appl. Phys.* 111 (2012) 07B544.
- [12] M.K. Fayek, F.M. Sayed Ahmed, S.S. Ata-Allah, Crystal, magnetic and electric behaviour of $CoMn_xFe_{2-x}O_4$ cubic ferrites, *J. Mater. Sci.* 27 (1992) 4813–4817.
- [13] K. Roumaili, Magnetic properties of Ni–Cu–Mn ferrite system, *J. Mol. Struct.* 1004 (2011) 1–7.
- [14] D.H. Lee, H.S. Kim, C.H. Yo, K. Ahn, K.H. Kim, The magnetic properties and electrical conduction mechanism of $Co_{1-x}Mn_xFe_2O_4$ spinel, *Mater. Chem. Phys.* 57 (1998) 169–172.
- [15] S. Sakurai, S. Sasaki, M. Okube, H. Ohara, T. Toyoda, Cation distribution and valence state in Mn–Zn ferrite examined by synchrotron X-rays, *Phys. B* 403 (2008) 3589–3595.
- [16] F.W. Harrison, W.P. Osmqnd, R.W. Teale, Cation distribution and magnetic moment of manganese ferrite, *Phys. Rev.* 106 (1957) 865–866.
- [17] D.R. Mane, U.N. Devatwal, K.M. Jadhav, Structural and magnetic properties of aluminium and chromium co-substituted cobalt ferrite, *Mater. Lett.* 44 (2000) 91–95.
- [18] F. Magalhaes, M.C. Pereira, S.E.C. Botrel, J.D. Fabris, W.A. Macedo, R. Mendonca, R.M. Lago, L.C.A. Oliveira, Cr-containing magnetites $Fe_{3-x}Cr_xO_4$: The role of Cr^{3+} and Fe^{2+} on the stability and reactivity towards H_2O_2 reactions, *Appl. Catal. A-Gen.* 332 (2007) 115–123.
- [19] M. Hashim, S.Kumar Alimuddin, S.E. Shirsath, R.K. Kotnala, H. Chung, R. Kumar, Structural properties and magnetic interactions in $Ni_{0.5}Mg_{0.5}Fe_{2-x}Cr_xO_4$ ($0 = x = 1$) ferrite nanoparticles, *Powder. Technol.* 229 (2012) 37–44.
- [20] R.H. Kadam, A.P. Birajdar, S.T. Alone, S.E. Shirsath, Fabrication of $Co_{0.5}Ni_{0.5}Cr_xFe_{2-x}O_4$ materials via sol–gel method and their characterizations, *J. Magn. Magn. Mater.* 327 (2013) 167–171.
- [21] A.K. Ghatage, S.A. Patil, S.K. Paranjpe, Neutron diffraction study of chromium substituted nickel ferrite, *Solid. State. Commun.* 98 (1996) 885–888.
- [22] M.B. Salamon, M. Jaime, The physics of manganites: structure and transport, *Rev. Modern Phys.* 73 (2001) 583–628.
- [23] E. Dagotto, T. Hotta, A. Moreo, Colossal magnetoresistant materials: the key role of phase separation, *Phys. Rep.* 344 (2001) 1–153.
- [24] Y. Tokura, Y. Tomioka, Colossal magnetoresistive manganites, *J. Magn. Magn. Mater.* 200 (1999) 1–23.
- [25] P.K. Siwach, H.K. Singh, O.N. Srivastava, Low field magnetotransport in manganites, *J. Phys.:* *Condens. Matter.* 20 (2008) 273201.
- [26] G.D. Tang, Study Of Cohesive Energy and Cation Valence in Several Kind of Lanthanum Manganites with ABO₃ Structure (in Chinese, with English abstract), (Doctor dissertation), Hebei Normal University, Shijiazhuang city, P R China, 2007.
- [27] C. Zener, Interaction between the *d*-shells in the transition metals. II. Ferromagnetic compounds of manganese with perovskite structure, *Phys. Rev.* 82 (1951) 403–405.
- [28] G.H. Jonker, J.H. Van Santen, Ferromagnetic compounds of manganese with perovskite structure, *Physica* 16 (1950) 337–349.
- [29] G., D. Tang, D.L. Hou, Z.Z. Li, X. Zhao, W.H. Qi, S.P. Liu, F.W. Zhao, Influence of cohesive energy on unit cell volume of perovskite manganites $La_{1-x}M_xMnO_3$, *Appl. Phys. Lett.* 89 (2006) 261919.
- [30] G.D. Tang, D.L. Hou, W. Chen, P. Hao, G.H. Liu, S.P. Liu, X.L. Zhang, L.Q. Xu, Estimation of Mn^{4+} ion content ratio in self-doped compound $La_{1-x}MnO_{3-\delta}$, *Appl. Phys. Lett.* 91 (2007) 152503.
- [31] G.D. Tang, S.P. Liu, X. Zhao, Y.G. Zhang, D.H. Ji, Y.F. Li, W.H. Qi, W. Chen, D.L. Hou, Study of the free energy of the $La_{1-x}Ca_xMnO_3$ manganites based on the temperature dependence of the crystal cell volume, *Appl. Phys. Lett.* 95 (2009) 121906.
- [32] A.J. Millis, B.I. Shraiman, R. Mueller, Dynamic Jahn–Teller effect and colossal magnetoresistance in $La_{1-x}Sr_xMnO_3$, *Phys. Rev. Lett.* 77 (1996) 175–178.
- [33] A. Urushibara, Y. Morimoto, T. Arima, A. Asamitsu, G. Kido, Y. Tokura, Insulator–metal transition and giant magnetoresistance in $La_{1-x}Sr_xMnO_3$, *Phys. Rev. B* 51 (1995) 14103–14109.
- [34] S.K. Ida, K. Ono, H. Kozaki, *Data on Physics in Common Use* (in Chinese), Science Press, Beijing, 1979 translated by Z X Zhang.
- [35] J. Stöhr, H.C. Siegmann, *Magnetism: From Fundamentals to Nanoscale Dynamics*, Springer Berlin Heidelberg, New York, 2006.

- [36] S.J. Hibble, S.P. Cooper, A.C. Hannon, I.D. Fawcett, M. Greenblatt, Local distortions in the colossal magnetoresistive manganates $\text{La}_{0.70}\text{Ca}_{0.30}\text{MnO}_3$, $\text{La}_{0.80}\text{Ca}_{0.20}\text{MnO}_3$ and $\text{La}_{0.70}\text{Sr}_{0.30}\text{MnO}_3$ revealed by total neutron diffraction, *J. Phys.: Condens. Matter* 11 (1999) 9921–9238.
- [37] P.G. Radaelli, D., E. Cox, M. Marezio, S.W. Cheong, P.E. Shiffer, A.P. Ramirez, Simultaneous structural, magnetic, and electronic transition in $\text{La}_{1-x}\text{Ca}_x\text{MnO}_3$ with $x = 0.25$ and 0.50 , *Phys. Rev. Lett.* 75 (1995) 4488–1191.
- [38] L.B. Liao, *Crystal Chemical and Crystal Physics* (in Chinese), Geological Publishing House, Beijing, 2000.
- [39] J.C. Phillips, Ionicity of the chemical bond in crystals, *Rev. Modern Phys.* 42 (1970) 317–356.
- [40] J. Thomas, I. Pollini, Ionic bonding of transition-metal halides: A spectroscopic approach, *Phys. Rev. B* 32 (1985) 2522–2532.
- [41] J.R. Chelikowsky, J.K. Burdett, Ionicity and the structural stability of solids, *Phys. Rev. Lett.* 56 (1986) 961–964.
- [42] A. Garcí a, M.L. Cohen, First-principles ionicity scales. I. Charge asymmetry in the solid state, *Phys. Rev. B* 47 (1993) 4215–4220.
- [43] L.M. Peng, S.L. Dudarev, M.J. Whelan, Ionicity of nickel oxide: Direct determination by reflection diffraction of high-energy electrons from the (100) surface, *Phys. Rev. B* 56 (1997) 15314–15319.
- [44] S.A. Chambers, T. Droubay, Role of oxide ion screening at oxide/metal interfaces, *Phys. Rev. B* 64 (2001) 075410.
- [45] B. Balamurugan, B.R. Mehta, S.M. Shivaprasad, Surface-modified CuO layer in size-stabilized single-phase Cu₂O nanoparticles, *Appl. Phys. Lett.* 79 (2001) 3176–3178.
- [46] M.J. Guittet, J.P. Crocombette, M. Gautier-Soyer, Bonding and XPS chemical shifts in ZrSiO₄ versus SiO₂ and ZrO₂: Charge transfer and electrostatic effects, *Phys. Rev. B* 63 (2001) 125117.
- [47] Y. Ito, Y. Idemoto, Y. Tsunoda, N. Koura, Relation between crystal structures, electronic structures, and electrode performances of $\text{LiMn}_{2-x}\text{M}_x\text{O}_4$ (M = Ni, Zn) as a cathode active material for 4V secondary Li batteries, *J. Power Sources* 119 (2003) 733–737.
- [48] H. Abu-Farsakh, A. Qteish, Ionicity scale based on the centers of maximally localized Wannier functions, *Phys. Rev. B* 75 (2007) 085201.
- [49] Y.P. Yu, X.J. Xing, L.M. Xu, S.X. Wu, S.W. Li, N-derived signals in the x-ray photoelectron spectra of N-doped anatase TiO₂, *J. Appl. Phys.* 105 (2009) 123535.
- [50] R. Lizárraga, E. Holmström, S.C. Parker, C. Arrouvel, Structural characterization of amorphous alumina and its polymorphs from first-principles XPS and NMR calculations, *Phys. Rev. B* 83 (2011) 094201.
- [51] N.E. Christensen, S. Satpathy, Z. Pawlowska, Bonding and ionicity in semiconductors, *Phys. Rev. B* 36 (1987) 1032–1050.
- [52] G.E. Arif, Y.A. Douiri, F.A. Abdullah, R. Khenata, Differential equations to calculate the ionicity factor of hexagonal structure semiconductors, *Superlattices Microstruct.* 53 (2013) 24–30.
- [53] Y.Y. Guo, C.K. Kuo, P.S. Nicholson, The ionicity of binary oxides and silicates, *Solid State Ion.* 123 (1999) 225–231.
- [54] R.R. Reddy, K.R. Gopal, Y. Nazeer Ahammed, K. Narasimhulu, L. Siva Sankar Reddy, C.V. Krishna Reddy, Correlation between optical electronegativity, molar refraction, ionicity and density of binary oxides, silicates and minerals, *Solid State Ion.* 176 (2005) 401–407.
- [55] R.E. Cohen, H. Krakayer, Lattice dynamics and origin of ferroelectricity in BaTiO₃ Linearized-augmented-plane-wave total-energy calculations, *Phys. Rev. B* 42 (1990) 6416–6423.
- [56] R.E. Cohen, Origin of ferroelectricity in perovskite oxides, *Nature* 358 (1992) 136–138.
- [57] J.C. Dupin, D. Gonbeau, P. Vinatier, A. Lévassieur, Systematic XPS studies of metal oxides hydroxides and peroxides, *Phys. Chem. Chem. Phys.* 2 (2000) 1319–1324.
- [58] L.Q. Wu, Y.C. Li, S.Q. Li, Z.Z. Li, G.D. Tang, W.H. Qi, L.C. Xue, X.S. Ge, L.L. Ding, Method for estimating ionicities of oxides using O1s photoelectron spectra, *AIP Adv.* 5 (2015) 097210.
- [59] L.Q. Wu, S.Q. Li, Y.C. Li, Z.Z. Li, G.D. Tang, W.H. Qi, L.C. Xue, L.L. Ding, X.S. Ge, Presence of monovalent oxygen anions in oxides demonstrated using X-ray photoelectron spectra, *Appl. Phys. Lett.* 108 (2016) 021905.
- [60] G.D. Tang, D.L. Hou, W. Chen, X. Zhao, W.H. Qi, Quantum-mechanical model for estimating the number ratio between different valence cations in multiaatom compounds, *Appl. Phys. Lett.* 90 (2007) 144101.
- [61] G.D. Tang, D.H. Ji, Y.X. Yao, S.P. Liu, Z.Z. Li, W.H. Qi, Q.J. Han, X. Hou, D.L. Hou, Quantum-mechanical method for estimating ion distributions in spinel ferrites, *Appl. Phys. Lett.* 98 (2011) 072511.
- [62] E. Merzbacher, *Quantum Mechanics*, second ed., John Wiley & Sons, Inc, New York, 1970.
- [63] D.H. Ji, G.D. Tang, Z.Z. Li, X. Hou, Q.J. Han, W.H. Qi, R.R. Bian, S.R. Liu, Quantum mechanical method for estimating ionicity of spinel ferrites, *J. Magn. Magn. Mater.* 326 (2013) 197–200.
- [64] G.D. Tang, Q.J. Han, J. Xu, D.H. Ji, W.H. Qi, Z.Z. Li, Z.F. Shang, X.Y. Zhang, Investigation of magnetic ordering and cation distribution in the spinel ferrites $\text{Cr}_x\text{Fe}_{3-x}\text{O}_4$ ($0.0 \leq x \leq 1.0$), *Physica B* 438 (2014) 91–96.
- [65] H.T. Jeng, G.Y. Guo, D.J. Huang, Charge-orbital ordering and verwey transition in magnetite, *Phys. Rev. Lett.* 93 (2004) 156403.
- [66] N. Nücker, J. Fink, J.C. Fuggle, P.J. Durham, W.M. Temmerman, Evidence for holes on oxygen sites in the high-Tc superconductors $\text{La}_{2-x}\text{Sr}_x\text{CuO}_4$ and $\text{YBa}_2\text{Cu}_3\text{O}_{7-y}$, *Phys. Rev. B* 37 (1988) 5158–5163.
- [67] K. Ibrahim, H.J. Qian, X. Wu, M.I. Abbas, J.O. Wang, C.H. Hong, R. Su, J. Zhong, Y.H. Dong, Z.Y. Wu, L. Wei, D.C. Xian, Y.X. Li, G.J. Lapeyre, N. Mannella, C.S. Fadley, Y. Baba, O 2p hole-assisted electronic processes in the $\text{Pr}_{1-x}\text{Sr}_x\text{MnO}_3$ ($x = 0.0, 0.3$) system, *Phys. Rev. B* 70 (2004) 224433.
- [68] G. Papavassiliou, M. Pissas, M. Belesi, M. Fardis, M. Karayanni, J.P. Ansermet, D. Carlier, C. Dimitropoulos, J. Dolinsek, Spin-polarized oxygen hole states in cation-deficient $\text{La}_{1-x}\text{Ca}_x\text{MnO}_{3+\delta}$, *Europhys. Lett.* 68 (2004) 453–459.
- [69] H.L. Ju, H.-C. Sohn, Kannan M. Krishnan, Evidence for O2p hole-driven conductivity in $\text{La}_{1-x}\text{Sr}_x\text{MnO}_3$ ($0 \leq x \leq 0.7$) and $\text{La}_{0.7}\text{Sr}_{0.3}\text{MnO}_2$ thin films, *Phys. Rev. Lett.* 79 (1997) 3230–3233.
- [70] A.S. Alexandrov, A.M. Bratkovsky, V.V. Kabanov, Phase coexistence and resistivity near the ferromagnetic transition of manganites, *Phys. Rev. Lett.* 96 (2006) 117003.
- [71] J. Xu, L. Ma, Z.Z. Li, L.L. Lang, W.H. Qi, G.D. Tang, L.Q. Wu, L.C. Xue, G.H. Wu, Antiferromagnetic coupling between Mn^{3+} and Mn^{2+} cations in Mn-doped spinel ferrites, *Phys. Status Solidi B* 252 (2015) 2820–2829.
- [72] L.Q. Wu, W.H. Qi, Y.C. Li, S.Q. Li, Z.Z. Li, G.D. Tang, L.C. Xue, X.S. Ge, L.L. Ding, Influence of thermal treatment on the ionic valence and the magnetic structure of perovskite manganites $\text{La}_{0.95}\text{Sr}_{0.05}\text{MnO}_3$ (in Chinese with English Abstract), *Acta Phys. Sin.* 65 (2016) 027501.
- [73] E. Kisker, K. Schroder, M. Campagna, W. Gudat, Temperature dependence of the exchange splitting of Fe by spin-resolved photoemission spectroscopy with synchrotron radiation, *Phys. Rev. Lett.* 52 (1984) 2285–2288.
- [74] P.D. Johnson, Spin-polarized photoemission, *Rep. Progr. Phys.* 60 (1997) 1217–1304.
- [75] L.C. Xue, L.L. Lang, J. Xu, Z.Z. Li, W.H. Qi, G.D. Tang, L.Q. Wu, Magnetic moment directions and distributions of cations in Cr (Co) substituted spinel ferrites $\text{Ni}_{0.7}\text{Fe}_{2.3}\text{O}_4$, *AIP Adv.* 5 (2015) 097167.
- [76] R.D. Shannon, Revised effective ionic radii and systematic studies of interatomic distances in halides and chalcogenides, *Acta Crystallogr. A* 32 (1976) 751–767.
- [77] Z.F. Shang, W.H. Qi, D.H. Ji, J. Xu, G.D. Tang, X.Y. Zhang, Z.Z. Li, L.L. Lang, Cation distributions estimated using the magnetic moments of the spinel ferrites at $\text{Co}_{1-x}\text{Cr}_x\text{Fe}_2\text{O}_4$ 10 K, *Chin. Phys. B* 23 (2014) 107503.
- [78] L.L. Lang, J. Xu, W.H. Qi, Z.Z. Li, G.D. Tang, Z.F. Shang, X.Y. Zhang, L.Q. Wu, L.C. Xue, Study of cation magnetic moment directions in Cr (Co) doped nickel ferrites, *J. Appl. Phys.* 116 (2014) 123901.

- [79] X.Y. Zhang, J. Xu, Z.Z. Li, W.H. Qi, G.D. Tang, Z.F. Shang, D.H. Ji, L.L. Lang, Experimental evidence for the magnetic moment directions of Cr^{2+} and Cr^{3+} cations in the spinel ferrites $\text{Cu}_{x_1}\text{Cr}_{x_2}\text{Fe}_{3-x_1-x_2}\text{O}_4$, *Physica B* 446 (2014) 92–99.
- [80] L.L. Lang, J. Xu, Z.Z. Li, W.H. Qi, G.D. Tang, Z.F. Shang, X.Y. Zhang, L.Q. Wu, L.C. Xue, Study of the magnetic structure and the cation distributions in MnCo spinel ferrites, *Phys. B* 462 (2015) 47–53.
- [81] C.M. Kale, P.P. Bardapurkar, S.J. Shukla, K.M. Jadhav, Mössbauer spectral studies of Ti^{4+} substituted nickel ferrite, *J. Magn. Magn. Mater.* 331 (2013) 220–224.
- [82] R.C. Srivastava, D.C. Khan, A.R. Das, Mössbauer and magnetic studies of Ti^{4+} -substituted Ni-Zn ferrites, *Phys. Rev. B* 41 (1990) 12514–12521.
- [83] M. Kobayashi, Y. Ooki, M. Takizawa, G.S. Song, A. Fujimori, Photoemission and x-ray absorption studies of valence states in $(\text{Ni}, \text{Zn}, \text{Fe}, \text{Ti})_3\text{O}_4$ thin films exhibiting photoinduced magnetization, *Appl. Phys. Lett.* 92 (2008) 082502.
- [84] G.D. Dwivedi, Amish G. Joshi, H. Kevin, P. Shahi, A. Kumar, A.K. Ghosh, H.D. Yang, S. Chatterjee, Existence of the multiferroic property at room temperature in Ti doped CoFe_2O_4 , *Solid State Commun.* 152 (2012) 360–363.
- [85] K. Srinivasa Rao, A. Mahesh Kumara, M. Chaitanya Varma, G.S.V.R.K. Choudary, K.H. Rao, Cation distribution of titanium substituted cobalt ferrites, *J. Alloys Compd.* 488 (2009) L6–L9.
- [86] C. Jin, W.B. Mi, P. Li, H.L. Bai, Experimental and first-principles study on the magnetic and transport properties of Ti-doped Fe_3O_4 epitaxial films, *J. Appl. Phys.* 110 (2011) 083905.
- [87] J. Xu, D.H. Ji, Z.Z. Li, W.H. Qi, G.D. Tang, Z.F. Shang, X.Y. Zhang, Magnetic moments of Ti cations in Ti-doped $\text{Ni}_{0.68}\text{Fe}_{2.32}\text{O}_4$ spinel ferrites, *J. Alloys Compd.* 619 (2015) 228–234.
- [88] J. Xu, D.H. Ji, Z.Z. Li, W.H. Qi, G.D. Tang, X.Y. Zhang, Z.F. Shang, L.L. Lang, Estimate of the cation distribution for Ti-doped $\text{Ni}_{0.68}\text{Fe}_{2.32}\text{O}_4$ spinel ferrites by fitting magnetic moments at 10 K, *Physica Status Solidi B* 252 (2015) 411–420.
- [89] J. Xu, W.H. Qi, D.H. Ji, Z.Z. Li, G.D. Tang, X.Y. Zhang, Z.F. Shang, L.L. Lang, Study on cation distribution and magnetic moment of Ti ions in spinel ferrites $\text{Ni}_{1-x}\text{Ti}_x\text{Fe}_2\text{O}_4$ (in Chinese with English Abstract), *Acta Phys. Sin.* 64 (2015) 017501.
- [90] G.D. Tang, Z.F. Shang, X.Y. Zhang, J. Xu, Z.Z. Li, C.M. Zhen, W.H. Qi, L.L. Lang, Evidence from infrared spectra for the magnetic moment directions of CR cations in the spinel ferrites, *Physica B* 463 (2015) 26–29.
- [91] A.A. Ati, Z. Othaman, A. Samavati, Influence of cobalt on structural and magnetic properties of nickel ferrite nanoparticles, *J. Mol. Struct.* 1052 (2013) 177–182.
- [92] M.A. Gabal, Y.M.A. Angari, M.W. Kadi, Structural and magnetic properties of nanocrystalline $\text{Ni}_{1-x}\text{Cu}_x\text{Fe}_2\text{O}_4$ prepared through oxalates precursors, *Polyhedron* 30 (2011) 1185–1190.
- [93] A.M. Wahba, M.B. Mohamed, Structural, magnetic, and dielectric properties of nanocrystalline Cr-substituted $\text{Co}_{0.8}\text{Ni}_{0.2}\text{Fe}_2\text{O}_4$ ferrite, *Ceram. Int.* 40 (2014) 6127–6135.
- [94] E. Pervaiz, I.H. Gul, Enhancement of electrical properties due to Cr^{3+} substitution in Co-ferrite nanoparticles synthesized by two chemical techniques, *J. Magn. Magn. Mater.* 324 (2012) 3695–3703.
- [95] N.W. Ashcroft, N.D. Mermin, *Solid State Physics*, Holt, Rinehart and Winston Inc., New York, 1976.
- [96] S.R. Liu, D.H. Ji, J. Xu, Z.Z. Li, G.D. Tang, R.R. Bian, W.H. Qi, Z.F. Shang, X.Y. Zhang, Estimation of cation distribution in spinel ferrites $\text{Co}_{1+x}\text{Fe}_{2-x}\text{O}_4$ ($0.0 \leq x \leq 2.0$) using the magnetic moments measured at 10 K, *J. Alloys Compd.* 581 (2013) 616–624.
- [97] R.R. Bian, Study on cation distributions and magnetic properties of ferrites $\text{NiCr}_x\text{Fe}_{2-x}\text{O}_4$ and $\text{Ni}_{1-x}\text{Co}_x\text{Fe}_2\text{O}_4$ (in chinese, with English abstract), (Master dissertation), Hebei Normal University, Shijiazhuang city, P R China, 2013.
- [98] Z.F. Shang, Study on magnetic properties and cation distributions in Co-Cr ferrites (in chinese, with English abstract), (Master dissertation), Hebei Normal University, Shijiazhuang city, P R China, 2014.
- [99] M. Takahashi, M.E. Fine, Magnetic behavior of quenched and aged CoFe_2O_4 - Co_3O_4 alloys, *J. Appl. Phys.* 43 (1972) 4205–4216.
- [100] J.V. Angadi, B. Rudraswamy, S. Matteppanavar, P. Bharathi, K. Praveena, Magnetic properties of nanocrystalline $\text{Mn}_{1-x}\text{Zn}_x\text{Fe}_2\text{O}_4$, *Conf. Proc.* 1665 (2015) 050014.
- [101] P. Mathur, A. Thakur, M. Singh, A study of nano-structured Zn-Mn soft spinel ferrites by the citrate precursor method, *Phys. Scr.* 77 (2008) 045701.
- [102] M. Singh, A comparative study of the electrical and the magnetic properties and Mössbauer studies of normal and hot pressed $\text{Mg}_x\text{Mn}_{1-x}\text{Fe}_2\text{O}_4$ ferrites, *J. Magn. Magn. Mater.* 299 (2006) 397–403.
- [103] B. Antic, N. Jovic, M.B. Pavlovic, A. Kremenovic, D. Manojlović, M. Vucinic-Vasic, A.S. Nikolić, Magnetization enhancement in nanostructured random type MgFe spinel prepared by soft mechanochemical route, *J. Appl. Phys.* 107 (2010) 043525.
- [104] V.M. Khot, A.B. Salunkhe, M.R. Phadatare, N.D. Thorat, S.H. Pawar, Low-temperature synthesis of $\text{Mn}_x\text{Mg}_{1-x}\text{Fe}_2\text{O}_4$ ($x = 0 - 1$) nanoparticles: cation distribution, structural and magnetic properties, *J. Phys. D: Appl. Phys.* 46 (2013) 055303.
- [105] R. Pandit, K.K. Sharma, P. Kaur, R.K. Kotnala, J. Shah, R. Kumar, Effect of Al substitution on structural, cation distribution, electrical and magnetic properties of CoFe_2O_4 , *J. Phys. Chem. Solids* 75 (2014) 558–569.
- [106] Q.J. Han, D.H. Ji, G.D. Tang, Z.Z. Li, X. Hou, W.H. Qi, R.R. Bian, S.R. Liu, Dependence of magnetization on cation distributions in the spinel ferrites $\text{Cu}_{1-x}\text{Zn}_x\text{Fe}_2\text{O}_4$ ($0.0 \leq x \leq 1.0$), *Phys. Status Solidi A* 209 (2012) 766–772.
- [107] Q.J. Han, D.H. Ji, G.D. Tang, Z.Z. Li, X. Hou, W.H. Qi, S.R. Liu, R.R. Bian, Estimating the cation distributions in the spinel ferrites $\text{Cu}_{0.5-x}\text{Ni}_{0.5}\text{Zn}_x\text{Fe}_2\text{O}_4$ ($0.0 \leq x \leq 0.5$), *J. Magn. Magn. Mater.* 324 (2012) 1975–1981.
- [108] L.L. Ding, L.C. Xue, Z.Z. Li, S.Q. Li, G.D. Tang, W.H. Qi, L.Q. Wu, X.S. Ge, Study of cation distributions in spinel ferrites $\text{M}_x\text{Mn}_{1-x}\text{Fe}_2\text{O}_4$ ($M = \text{Zn}, \text{Mg}, \text{Al}$), *AIP Adv.* 6 (2016) 105012.
- [109] L.Q. Wu, W.H. Qi, X.S. Ge, D.H. Ji, Z.Z. Li, G.D. Tang, W. Zhong, Study of dependence of magnetic moment of $\text{La}_{1-x}\text{Sr}_x\text{MnO}_3$ on Sr doping level x, *Europhys. Lett.* 120 (2017) 27001.
- [110] L.Q. Wu, Study of Oxygen Ionic Valence and Its Influence on the Magnetic Property of the Perovskite Manganites $\text{La}_{1-x}\text{Sr}_x\text{MnO}_3$ (in chinese, with English abstract), (Master dissertations), Hebei Normal University, Shijiazhuang city, P R China, 2016.
- [111] S.P. Liu, G.D. Tang, P. Hao, L.Q. Xu, Y.G. Zhang, W.H. Qi, X. Zhao, D.L. Hou, W. Chen, Rietveld fitting of x-ray diffraction spectra for the double phase composites $\text{La}_{0.7-x}\text{Sr}_{0.3}\text{Mn}_{1-y}\text{O}_{3-1.5(x+y)}/(\text{Mn}_3\text{O}_4)_y/3$, *J. Appl. Phys.* 105 (2009) 013905.
- [112] S.P. Liu, Y. Xie, J. Xie, Gui-De Tang, Structural and magnetic properties of self-doped perovskite manganites $\text{La}_{0.8-x}\text{Sr}_{0.2}\text{MnO}_{3-\delta}$, *J. Appl. Phys.* 110 (2011) 123714.
- [113] D.H. Ji, G.D. Tang, Z.Z. Li, Q.J. Han, X. Hou, R.R. Bian, S.R. Liu, Investigation on the maximum content of vacancy at the B sites in $\text{La}_{0.75}\text{Sr}_{0.25}\text{Mn}_{1-x}\text{O}_3$ perovskite manganites, *J. Appl. Phys.* 111 (2012) 113902.
- [114] D.H. Ji, X. Hou, G.D. Tang, Z.Z. Li, D.L. Hou, M.G. Zhu, Oxygen content and magnetic properties of composites $\text{La}_{0.75}\text{Sr}_{0.25}\text{MnO}_{3\pm\delta}$ calcined at different temperatures, *Rare metals* 33 (2014) 452–458.
- [115] X. Hou, D.H. Ji, W.H. Qi, G.D. Tang, Z.Z. Li, Structural and magnetic properties of $\text{La}_{0.7}\text{Sr}_{0.1}\text{Ag}_x\text{MnO}_{3-\delta}$ perovskite manganites, *Chin. Phys. B* 24 (2015) 057501.
- [116] J. Töpfer, J.B. Goodenough, $\text{LaMnO}_{3+\delta}$ revisited, *J. Solid State Chem.* 130 (1997) 117–128.
- [117] F. Prado, R.D. Sanchez, A. Caneiro, M.T. Causa, M. Tovar, Discontinuous evolution of the highly distorted orthorhombic structure and the magnetic order $\text{LaMnO}_{3\pm\delta}$ in perovskite, *J. Solid State Chem.* 146 (1999) 418–427.
- [118] K. Jiang, S.K. Gong, Effect of cobalt on the magnetoresistance characteristics of rare-earth doped manganites, *Chin. Phys. B* 18 (2009) 3035–3039.

- [119] Y. Sun, W. Tong, X.J. Xu, Y.H. Zhang, Tuning colossal magnetoresistance response by Cr substitution in $\text{La}_{0.67}\text{Sr}_{0.33}\text{MnO}_3$, *Appl. Phys. Lett.* 78 (2001) 643–645.
- [120] J.J. Blanco, M. Insausti, I. Gil de Muro, L. Lezama, T. Rojo, Neutron diffraction and magnetic study of the $\text{Nd}_{0.7}\text{Pb}_{0.3}\text{Mn}_{1-x}\text{Fe}_x\text{O}_3$ ($0 \leq x \leq 0.1$) perovskites, *J. Solid State. Chem.* 179 (2006) 623–631.
- [121] H. Yang, W.H. Qi, D.H. Ji, Z.F. Shang, X.Y. Zhang, J. Xu, L.L. Lang, Structure and magnetic properties of perovskite manganites $\text{La}_{2/3}\text{Sr}_{1/3}\text{Fe}_x\text{Mn}_{1-x}\text{O}_3$ (in Chinese with English abstract), *Acta Phys. Sin.* 63 (2014) 087503.
- [122] S.Q. Li, L.Q. Wu, W.H. Qi, X.S. Ge, Z.Z. Li, G.D. Tang, W. Zhong, Unique magnetic properties of perovskite manganites $\text{La}_{0.95}\text{T}_{0.05}\text{Cr}_x\text{Mn}_{1-x}\text{O}_3$ ($T = \text{Ca}, \text{Sr}$), *J. Magn. Magn. Mater.* 460 (2018) 501–508.
- [123] X.S. Ge, L.Q. Wu, S.Q. Li, Z.Z. Li, G.D. Tang, W.H. Qi, H.J. Zhou, L.C. Xue, L.L. Ding, Study of magnetic ordering in the perovskite manganites $\text{Pr}_{0.6}\text{Sr}_{0.4}\text{Cr}_x\text{Mn}_{1-x}\text{O}_3$, *AIP Adv.* 7 (2017) 045302.
- [124] X.S. Ge, Z.Z. Li, W.H. Qi, D.H. Ji, G.D. Tang, L.L. Ding, J.J. Qian, Y.N. Du, Magnetic and electrical transport properties of perovskite manganites $\text{Pr}_{0.6}\text{Sr}_{0.4}\text{M}_x\text{Mn}_{1-x}\text{O}_3$ ($M = \text{Fe}, \text{Co}, \text{Ni}$), *AIP Adv.* 7 (2017) 125002.
- [125] X.S. Ge, Study of magnetic ordering in the perovskite manganites $\text{Pr}_{0.6}\text{Sr}_{0.4}\text{Mn}_{1-x}\text{M}_x\text{O}_3$ ($M = \text{Cr}, \text{Fe}, \text{Co}, \text{Ni}$), (Master dissertation), Hebei Normal University, Shijiazhuang city, P R China, 2017.
- [126] D.V. Maheswar Repaka, T.S. Tripathi, M. Aparnadevi, R. Mahendiran, Magnetocaloric effect and magnetothermopower in the room temperature ferromagnet $\text{Pr}_{0.6}\text{Sr}_{0.4}\text{MnO}_3$, *J. Appl. Phys.* 112 (2012) 123915.
- [127] S. Rößler, H.S. Nair, U.K. Rößler, C.M.N. Kumar, S. Elizabeth, S. Wirth, Ferromagnetic transition and specific heat of $\text{Pr}_{0.6}\text{Sr}_{0.4}\text{MnO}_3$, *Phys. Rev. B* 84 (2011) 184422.
- [128] W. Boujelben, M. Ellouze, A. Cheikh-Rouhou, J. Pierreb, Q. Cai, W.B. Yelon, K. Shimizu, C. Dubourdieu, Neutron diffraction, NMR and magneto-transport properties in the $\text{Pr}_{0.6}\text{Sr}_{0.4}\text{MnO}_3$ perovskite manganite, *J. Alloys Compd.* 334 (2002) 1–8.
- [129] R. Mahendiran, S.K. Tiwary, A.K. Raychaudhuri, T.V. Ramakrishnan, R. Mahesh, N. Rangavittal, C.N.R. Rao, Structure electron-transport properties and giant magnetoresistance of hole-doped LaMnO_3 systems, *Phys. Rev. B* 53 (1996) 3348.
- [130] J. Sánchez-Barriga, J. Minár, J. Braun, A. Varykhalov, V. Boni, I. Di Marco, O. Rader, V. Bellini, F. Manghi, H. Ebert, M.I. Katsnelson, A.I. Lichtenstein, O. Eriksson, W. Eberhardt, H.A. Dürr, J. Fink, Quantitative determination of spin-dependent quasiparticle lifetimes and electronic correlations in hcp cobalt, *Phys. Rev. B* 82 (2010) 104414.
- [131] W.H. Qi, L. Ma, Z.Z. Li, G.D. Tang, G.H. Wu, Dependences of valence electronic structure on magnetic moment and electrical resistivity of metals (in Chinese with English Abstract), *Acta Phys. Sin.* 66 (2017) 027101.
- [132] G.E. Pacchioni, L. Gragnaniello, F. Donati, M. Pivetta, G. Autès, O.V. Yazyev, S. Rusponi, H. Brune, Multiplet features and magnetic properties of Fe on Cu(111): From single atoms to small clusters, *Phys. Rev. B* 91 (2015) 235426.
- [133] W. Jauch, M. Reehuis, Electron density distribution in α iron: A γ ray diffraction study, *Phys. Rev. B* 76 (2007) 235121.
- [134] M.B. Stearns, On the origin of ferromagnetism and the hyperfine fields in Fe, Co, and Ni, *Phys. Rev. B* 8 (1973) 4383–4398.
- [135] M.B. Stearns, Why is iron magnetic? *Phys. Today* 31 (4) (1978) 34–39.
- [136] W.H. Qi, Z.Z. Li, L. Ma, G.D. Tang, G.H. Wu, F.X. Hu, Molecular field origin for magnetic ordering of magnetic materials (in Chinese with English Abstract), *Acta Phys. Sin.* 66 (2017) 067501.
- [137] W.H. Qi, Z.Z. Li, L. Ma, G.D. Tang, Why typical magnetic metals and oxides have different Curie temperatures? *AIP Adv.* 8 (2018) 065105.
- [138] X. Liu, W.B. Mi, Q. Zhang, X.X. Zhang, Anisotropic magnetoresistance across Verwey transition in charge ordered Fe_3O_4 epitaxial films, *Phys. Rev. B.* 96 (2017) 214434.
- [139] X. Liu, L. Yin, W.B. Mi, Biaxial strain effect induced electronic structure alternation and trimeron recombination in Fe_3O_4 , *Sci. Rep.* 7 (2017) 43403.
- [140] W.H. Zhong, B.K. Tay, S.P. Lau, X.W. Sun, S. Li, C.Q. Sun, Structural and magnetic properties of iron-nitride thin films deposited using a filtered cathodic vacuum arc, *Thin Solid Films* 478 (2005) 61–66.
- [141] W.T. Zheng, C.Q. Sun, Electronic process of nitriding: mechanism and applications, *Prog. Solid State Chem.* 34 (2006) 1–20.
- [142] W.H. Zhong, C.Q. Sun, S. Li, H.L. Bai, E.Y. Jiang, Impact of bond-order loss on surface and nanosolid magnetism, *Acta Mater.* 53 (2005) 3207–3214.
- [143] S.N. Khanna, S. Linderoth, Magnetic behavior of clusters of ferromagnetic transition metals, *Phys. Rev. Lett.* 67 (1991) 742–745.
- [144] J.J. Zhao, X.S. Chen, Q. Sun, F.Q. Liu, G.H. Wang, A simple d-band model for the magnetic property of ferromagnetic transition-metal clusters, *Phys. Lett. A* 205 (1995) 308–312.